BILINGUAL PUBLISHING CO.
Pioneer of Global Academics Since 1984

Journal of Building Material Science

Volume 3 • Issue 2 • December 2021 ISSN 2630-5216(Online)

Volume 3 Issue 2 • December 2021 • ISSN 2630-5216 (Online)

JOURNAL OF BUILDING MATERIAL SCIENCE

BILINGUAL PUBLISHING CO.
Pioneer of Global Academics Since 1984

BILINGUAL PUBLISHING CO.
Pioneer of Global Academics Since 1984

Volume 3 | Issue 2 | December 2021 | Page1-66
Journal of Building Material Science

Contents

Articles

Reviews

BILINGUAL PUBLISHING CO.
Pioneer of Global Academics Since 1984

Journal of Building Material Science
https://ojs.bilpublishing.com/index.php/jbms

REVIEW

Hemp Concrete: A Sustainable Green Material for Conventional Concrete

Sudarshan D. Kore* **J. S. Sudarsan**

School of Construction Management, National Institute of Construction Management and Research (NICMAR) Pune, India

ARTICLE INFO

Article history
Received: 1 May 2021
Accepted: 18 July 2021
Published Online: 13 September 2021

Keywords:
Hemp
Hempshiv
Concrete
Sustainability

ABSTRACT

Concrete is one of the most important building material and day by day the utilization of concrete is increasing to meet the infrastructure development requirement. On one hand it is unavoidable but some alternative to be explored to reduce the global environmental impact caused by the concrete. To overcome this from the last decade the world is looking towards the fact of sustainability due to rapid industrialization. The growth in the construction industry increased the demand of concrete as construction material. This concrete produces significant amount of greenhouse emission in the environment. There is a need to find an alternative solution to minimize the greenhouse emission emitted from the concrete manufacturing plant.

Hempcrete is a building material prepared from hemp yarns, lime and water. This composite material has several beneficial properties like low in cost, easily available, thermal and acoustic insulation, low density and sustainable cause of no adverse impact of carbon footprint on production. In this study the properties and several benefits of the hempcrete were discussed in detail.

1. Introduction

Rapid growth in the urbanization, industrialization and infrastructure activities in the world increased the demand of the amenities in the developed and undeveloped countries. The increased demand in the infrastructure amenities by people of the society is much more in later 1990'S. To meet this demand the construction industry uses concrete as construction material which is one of the popular material in the world. The concrete is prepared by cement, fine aggregate, coarse aggregate and water. In today's scenario approximately 25 billion tons per year of concrete is being produced globally [18]. For production of concrete the main ingredient is cement. For production one ton of cement approximately 0.98 tons of carbon dioxide is emitted in the environment [2]. The emission of this gas lead to be the one of the major causes for global warming. The issue of global warming attracts the researchers to find a suitable alternative material as binder for construction industry which makes it economical and sustainable [3]. There are various other materials found by the researchers like waste from thermal power plant (Ash) metakaoline, Ground Granulated Blast furnace Slag (GGBS), silica fume etc. [17,15,10]. For sustainable development need to find some materials which does not have any impact on the greenhouse gas emissions.

The recent advancement in the construction industry

**Corresponding Author:*
Sudarshan D. Kore,
School of Construction Management, National Institute of Construction Management and Research (NICMAR) Pune, India;
Email: skore@nicmar.ac.in; sudarshankore123@gmail.com

 DOI: https://doi.org/10.30564/jbms.v3i2.3189

developed some new innovative materials which may be called as ecofriendly, sustainable or green construction materials. The various studies conducted by the past researchers explored the use of plant fibers and byproducts in concrete as construction material for sustainable developments for example wood, hemp, sunflower, flax, sisal [1].

2. Emerging Trends on a New Challenge

Hemp is grown in the tropical regions of the world as one of the popular crop in those regions. The biological name of this plant is *Cannabis Sativa* as shown in Figure 1. The fibers generated from the hemp stack is used as a building product along with lime and cement [12].

Figure 1. Hemp Plant

Hemp is a quickly developing yearly yield (1.5 - 4 m tallness) which is mostly developed for its high rigidity common fiber which develops in the shoot nearby the timbered center of the plant [27]. This timbered center of the plant is slashed up into little sizes (5-25 mm) (hurd/shive) and blended in with lime, water and a little amount of concrete (to speed up setting time) to shape of composite blend called hempcrete [7]. The use of hemp fibers was first trialed by France in 1990. The hemp fibers were used for production of less weight concrete, making of protection boards, mass-spraying of hempcrete respectively for the production of lightweight composites [15]. Hempcrete is obtained by adding the hemp shives or fibers along with cement or lime in presence of water. It is having several benefits such as low density, and acoustic protection properties, and can passively regulate humidity in a built environment [29]. Due to low strength and modulus elasticity it cannot be used as structural concrete. It can be used as filling material for construction of ecofriendly and sustainable structures [3]. Pores in hempcrete can create a respiratory structure that absorbs and desorbs moisture from its environment and controls sudden tempering and humidity changes in its environment. This ability of the hempcrete allows the users to use to maintain healthy environment in arid regions [8]. Hemp is an agriculture product cause of this it is a carbon negative martial which doesn't emit any carbon emission during the production process [21]. The researchers claimed that per kilogram of hemp shiv sequesters about 1.6 to 1.8 kg of CO_2 [14,25].

From the past fifteen years the hemp is termed as green building material which was seen from the previous studies. Hemp had significant papers as a fibre plant in the past, and already processed into cord and fabric in Egypt's in the past dynasty 3500 years ago [24]. Hemp's potential for green growth in Europe has been rediscovered around 25 years ago [13]. Several European countries have changed their laws to enable the production and processing of manufacturing hemp ranges with a content of less than 0.2% in the higher part of the plant. Recent policy reforms in favor of cannabis farming and manufacturing on a global scale are only viable if they are combined with the use of hemp.

Building is known to consume approximately 40% of the total energy production, 25% of the world's water, and 40% of the world's resources (UN Environment Program, 2016). By substituting plant aggregates for mineral aggregates, this consumption can be greatly reduced [6]. This calculation not only locks CO_2 within the building envelope, but it also lowers operating energy such as air conditioning, makes insulating hemp concrete a very promising choice for fighting global warming [5]. Currently, about 5,000 tonnes of hemp material are used for construction purposes in France, the country that pioneered the use of hemp-based insulating construction materials in the early 1990s, followed by other European countries, and has increased in popularity in the last 15 years as a result of growing research in this area [4].

Figure 2. Brick made from Hempcrete [16]

DOI: https://doi.org/10.30564/jbms.v3i2.3189

3. Hempcrete's Characteristics

Capabilities for dealing with moisture

Hempcrete's vapor permeable walls enable dampness to naturally move starved of the risk of condensation and water harm [28].

It has a large potential for retaining moisture. With permeable skins on both sides of the wall, moisture-related problems are significantly reduced in any area.

It hurd contains a lot of silica, because when it's combined with lime, the hurd begins to mineralize.

Compressive Strength (CS)

According to Elfordy et al., [11] compressive strength of hempcrete blocks varies from 14.5 psi (1.02 kg/cm^2) to 420 psi (29.5 kg/cm^2).

It helps to stabilize or harden lightweight partition framing members. Hempcrete's density ranges from 93.6 to 136.4 kg/m^3. As a result, it is bright.

Thermal Efficiency

Hempcrete has exceptional thermal properties.

Hemp concrete has a R value of 1.5 to 2.0 per inch in its steady state [26].

The density obtained in the combination, as well as the binder/Hemp ratio, will affect the values.

It also passed the European burn exam, which is a 75-minute test [9].

4. Sustainable Building Material

It can raise up to four meters tall in three months without pesticides or herbicides, and hemp cultivation is quickly growing around the world [7].

The recent growth in this sector is due to several reasons, not the least of which is our collective sense that what we are doing with our world isn't quite working out.

This sensation is growing in intensity, but it is at odds with our normal way of life. Hemp is a green building material with a wide range of applications, and it is expected to become a valuable crop in the future [28].

One of the most interesting the components of this hemp renaissance is the slow growth in the use of hemp as a building fabric [7].

Hempcrete consists of hemp 'shiv', the woody middle of the hemp plant broken up into something as nice wooden chips, that's then mixed with a lime-based complete binder and water.

This arrangement sets hard to become an exceptional padding for walls, floors, or roofs. It has numerous benefits over supplementary building materials, including being fireproof, non-toxic, sustainable, breathable, and highly isolative.

Figure 3. Walls with hemp clay bricks

Figure 4. Hemp lime concrete sprayed application

5. Environmentally Friendly Construction Material

It's probably safe to say that climate change poses the biggest threat to our future survival, and buildings account for roughly half of all greenhouse gas emissions, both during construction and in heating, cooling, and maintenance demands after they've been occupied.

At any of these points, it has the ability to minimize emissions, making it a genuinely green building material.

Plants engross carbon from the air as they grow, and hemp is able to lock up more carbon per hectare than almost every other plant, including trees, due to its rapid growth rate [19].

Once this biomass is processed, mixed with lime, and incorporated into a structure, the carbon is locked up for the life of the structure. Lime also balances the energy used in its production by removing CO_2 from the air as it sets.

DOI: https://doi.org/10.30564/jbms.v3i2.3189

Most traditional construction materials have a high embodied carbon content, which means they release large amounts of CO_2 into the environment during their manufacture.

It typically absorbs more carbon than it emits during production, rendering it a carbon-neutral material. To set that into perception, m^3 of hempcrete will restore around 110 kg of CO_2 [17]. For the walls, an average sized house will use about 50 cubic meters of hempcrete, resulting in 5.5 tons of carbon being locked up over the course of the building's lifespan [10,19].

In contrast, a typical new house of comparable size will likely release 48 tons of carbon into the atmosphere through its walls. This equates to a carbon reduction of 53.5 tons per house constructed [5]. It's clear that the carbon balance isn't even near, and that, despite minor differences in measurement methods**,** building with hempcrete will save you money.

Figure 5. Structural vault of hemp concrete

6. Insulation

The potential of this green material is to save carbon and to act as an insulating enclosing material with two main properties that help it minimize carbon emissions and save money on energy bills: moisture management and thermal mass. These features, which are often ignored by building codes, mean that hempcrete buildings use less energy to have inhabitants warm and happy.

Its ability to absorb and desorb moisture helps it to control humidity in the house, allowing for greater comfort at lower temperatures and lower energy bills.

Hempcrete's thermally massive properties cause the building's fabric to warm up and remain warm even when the weather is modified [9]. This is in contrast to most modern houses, where the lining layer in the partition is placed so close to the inner surface that the only thing that keeps the space warm.

The biggest downside is that when there is some kind of aeration or draught, the room heat drops rapidly, forcing the regulator to cut in and reheat the room on a consistent basis. This, too, has strong negative effects for energy bills. Anyone who lives in a modern home and has observed how easily the room temperature drops when the heating is switched off is frustrated [20].

Figure 6. Hemp Concrete as insulating material

7. Expertise and Experience

There is a shortage of knowledge and experience within the hempcrete industry, if there is one at all. There are a few businesses that are successfully constructing and renovating, but the majority of the structures are one-off projects. The experience and skills needed for these one-off projects are similar to, but not equal to, those required for large-scale construction.

Hempcrete buildings, like any other building, may benefit from economies of scale, but scale necessitates investment, and investment necessitates confidence.

At the moment, the numerous yet effective hempcrete builders are not banding together to provide this evidence

DOI: https://doi.org/10.30564/jbms.v3i2.3189

in a crime manner.

8. Potential Future

The raw material for hempcrete will become more readily available as hemp cultivation spreads around the world and processing plants made easy [20]. If textile manufacturers can shift away from cotton and toward hemp, the hemp market can grow quickly, allowing the price of hemp shiv to remain steady.

The emerging infrastructure material manufacturing industry has attracted a lot of investment, but due to outdated laws that make hemp farming difficult.

Figure 7. Construction with Hempcrete

Any hempcrete building offers evidence for how we need to design, and if we look hard enough, we will find proof that existing standard building strategies are failing us. More concrete structures are quietly underperforming, dumping even more carbon into the atmosphere.

Hempcrete isn't a commodity through a lot of unanswered questions. It's a sustainable material of future age, and it has the potential to help us develop in a more ecological way, resulting in better building results.

9. Applications of Hempcrete

9.1 Plastering

- Painted on the building's interior or exterior surfaces.
- Ideal for places that are prone to cracking and knocks.
- Better for filling in and repairing holes in existing plaster.
- Spray applications save time and money by eliminating the need for formwork.
- The most popular approach is to add lime plaster directly to hempcrete [22].

9.2 Form Packing

To maximize the insulating potential, it is tightly filled near the surfaces and loosely in the middle.

The frame may be balanced or bent to one side. The exterior is also finished with cladding.

Figure 8. Form packing of hempcrete

9.3 Precast Insulation Panels

Hemp concrete construction utilizes precast panels for large structures.

Individually built residences that are assembled on site may also benefit from precast panels.

The British Science Museum cast-off hempcrete boards in an artefact storage room.

10. Hempcrete vs Concrete

In terms of design, concrete has a distinct benefit over hempcrete in that it can be used to create load-bearing structures.

Hempcrete, on the other hand, has obvious benefits in its ability to withstand mould, bacteria, and damp, which are common problems for homeowners in older buildings and can cause severe respiratory problems.

Concrete [23] and hempcrete are both fire-resistant, maintain heat well, and are effective sound-proofing materials. The initial cost of the materials, as well as their suitability for a variety of large-scale construction projects, would likely determine any change in industry between widespread acceptances of concrete as a building material versus hempcrete.

 DOI: https://doi.org/10.30564/jbms.v3i2.3189

Hempcrete **Concrete**

Figure 9. Comparison of Hemcrete with Concrete [23]

11. Conclusions

Hempcrete has not only a help in protecting the environment, global warming and climate change; it also provides comfort in the structures.

Its hygrometric behavior leads to indoor air quality and a relaxed indoor microclimate condition.

It displays low thermal conductivity, low density, low strength, high absorptivity and high moisture buffer capacity.

It is ensuring a building envelope, which can be used in the wall, roof and floor. The mixture proportions should be calculated properly according to the application area, so as to evade unforeseen effects.

It is an appropriate plant for growing in environments other than extreme desert climates and high mountain regions.

Guidelines must be formed to endorse hempcrete usage in the building's assembly.

The researches related to hemp must be encouraged it will rise in the coming years and it will indirectly help in producing green building products and technologies.

References

[1] S. Amziane (2016), Overview on biobased building material made with plant aggregate, Sustain. Constr. Mater. Technol. 2016-August 31-38.

[2] E. Awwad, D. Choueiter, H. Khatib (2020), Concrete Masonry Blocks Reinforced with Local Industrial Hemp Fibers and Hurds Third International Conference on Sustainable Construction Materials and, Sustain. Constr. Mater. Technol. -August 1-11.

[3] G. Balčiunas, S. Vejelis, S. Vaitkus, A. Kairyte 2013), Physical properties and structure of composite made by using hemp hurds and different binding materials, Procedia Eng. 57 (159-166.

[4] H. Bedlivá, N. Isaacs, (2014), Hempcrete - An environmentally friendly material?, Adv. Mater. Res. 1041 83-86.

[5] T. Bejat, Hygrothermal Behaviour of a Hemp Concrete Wall :, in: 13th Conf. Int. Build. Perform. Simul. Assoc., Chambery France, 2013.

[6] T. Bejat, A. Piot, A. Jay, L. Bessette (2015), Study of two hemp concrete walls in real weather conditions, Energy Procedia. 78 1605-1610.

[7] R. Brencis, S. Pleiksnis, J. Skujans, A. Adamovics, U. Gross (2017), Lightweight composite building materials with hemp (Cannabis sativa L.) additives, Chem. Eng. Trans. 57 1375-1380.

[8] P. de Bruijn (2008), Hemp Concretes Hemp Concretes, Swedish University of Agricultural Sciences.

[9] F. Delhomme, A. Hajimohammadi, A. Almeida, C. Jiang, D. Moreau, Y. Gan, X. Wang, A. Castel (2020), Physical properties of Australian hurd used as aggregate for hemp concrete, Mater. Today Commun. 24, 100986.

[10] T.M. Dinh, C. Magniont, M. Coutand (2012), Hemp concrete using innovative pozzolanic binder, First Int. Conf. Bio-Based Build. Mater. 33, 265-270.

[11] S. Elfordy, F. Lucas, F. Tancret, Y. Scudeller, L. Goudet (2008), Mechanical and thermal properties of lime and hemp concrete ("hempcrete") manufactured by a projection process, Constr. Build. Mater. 22 , 2116-2123.

[12] J.C. van Empelen (2018), A study into more sustainable, alternative building materials as a substitute for concrete in tropical climates, 1-26.

[13] R. Hornby (2020), A Review of Alternative Building Materials in comparison to CMU : Hempcrete , Woodcrete , Papercrete, Univ. Arizona. 1-16.

[14] T. Jami, S.R. Karade, L.P. Singh (2018), Hemp Concrete - A Traditional and Novel Green Building Ma-

DOI: https://doi.org/10.30564/jbms.v3i2.3189

terial, Proc. Int. Conf. Adv. Constr. Mater. Struct.
[15] M. Jothilingam, P. Paul (2019), Study on strength and microstructure of hempcrete, AIP Conf. Proc. 2117.
[16] N.M.T. K, H.G. Sunil, D. Rani, A. Kumar (2016), Manufacturing of building blocks using Hempcrete, 02 62-73.
[17] J.K. Kana (2020), Experimental investigation on the physical properties of hemp concrete on addition of low carbon material, Int. Res. J. Eng. Technol. 7 2360-2364.
[18] H. Klee, Briefing (2004): The cement sustainability initiative, Proc. Inst. Civ. Eng. Eng. Sustain. 157 9-11.
[19] C. Magniont, G. Escadeillas, M. Coutand, C. Oms-Multon (2012), Use of plant aggregates in building ecomaterials, Eur. J. Environ. Civ. Eng. 16.
[20] A. Mukherjee, C. MacDougall (2013), Structural benefits of hempcrete infill in timber stud walls, Int. J. Sustain. Build. Technol. Urban Dev. 4 295-305.
[21] P. Novakova, J. Sal (2019), Use of technical hemp for concrete-Hempcrete, IOP Conf. Ser. Mater. Sci. Eng. 603.
[22] E. Ob (2021), Hempcrete , or concrete made of hemp in architectural engineering, Ecoreactor. 1-11.
[23] K. Rajput 2021), Hempcrete Vs Concrete | What Is Hempcrete | What Is Concrete, (1-11).
[24] R. Rhydwen (2010), Building with Hemp and Binder.
[25] A.N.G. Shi, Y. Isebelle, K.O.H.S. Hwee, T.A.Y.W.E.N. Lin, N.G. Shi, H.U.I. Jolyn, O.N.G.T. Dee, C.A.I. Yufeng, I. Nabilah, L.O.W. Kerling, K. Teck, Y. Melvin, L.I.N.J.U.N. Liang, G.O.H.J. Garvin (2015), Hemp concrete, National University of Singapore.
[26] M. Sinka, L. Radina, G. Sahmenko, A. Korjakins, D. Bajare (2015), Enhancement of lime-hemp concrete properties using different manufacturing technologies, First Int. Conf. Bio-Based Build. Mater.
[27] A. Sutton, D. Black, P. Walker (2011), BRE, IME An introduction to low-impact building materials, BRE. 1-6.
[28] J. and T.F. Updike (2016), Hempcrete as a Sustainable Building Material Joseph Updike South Dakota School of Mines and Technology ASCE Student Member 7296671 501 E . Saint Joseph St . Rapid City , SD 57701 Joseph.Updike@mines.sdsmt.edu, ASCE, Rapid.
[29] T. Woods (2021), Hemp MythBusters — Can hempcrete replace concrete?, Medium. 1-10.

 DOI: https://doi.org/10.30564/jbms.v3i2.3189

BILINGUAL PUBLISHING CO.
Pioneer of Global Academics Since 1984

Journal of Building Material Science
https://ojs.bilpublishing.com/index.php/jbms

REVIEW

Partial Replacement of Cement by Solid Wastes as New Materials for Green Sustainable Construction Applications

Hosam M. Saleh[1*] Abeer A. Faheim[2] Aida A. Salman[2] Abeer M. El-Sayed[2]

1. Radioisotope Department, Nuclear Research Center, Atomic Energy Egyptian Atomic Energy Authority, Cairo, Egypt
2. Chemistry Department, Faculty of Science, Al Azhar University, Egypt

ARTICLE INFO

Article history
Received: 12 April 2021
Accepted: 30 May 2021
Published Online: 18 September 2021

Keywords:
Construction materials
Sustainable composites
Green concrete
Solid wastes

ABSTRACT

The manufacturing of ordinary Portland cement is an energy-intensive process that results in pollution and CO_2 emissions, among other issues. There is a need for an environmentally friendly green concrete substitute. Waste products from a variety of sectors can be recycled and used as a green concrete substitute. This decreases the environmental effects of concrete manufacturing as well as energy consumption. The use of solid waste materials for green building is extremely important now and in the future. Green concrete is also in its infancy in terms of manufacturing and application. Academics must intervene by encouraging business implementation. The aim of this review paper is to raise awareness about the importance of repurposing recycled materials and to highlight new technologies for producing green, sustainable concrete.

1. Introduction

Nine separate mixtures with a water-to-binder ratio (W/B) of 0.8 with differing Stabilized polystyrene (SPS) content ratios of 0, 60 and 100 % were prepared and tested as a partial substitution of the natural fine aggregate with an approximate amount of 0, 20 and 40 % fly ash substitution with Portland cement. The properties of the concrete tested were compressive strength and ultrasonic pulse velocity (UPV) at 28-day age. The findings suggest a drop in compressive strength and UPV with increasing concentrations of SPS and fly ash in concrete [1].

Polymer mortar and polymeric composites have been prepared using recycled polystyrene waste and cement dust waste as a filler due to cost and environmental concerns. For comparison, virgin polystyrene and Portland cement are used. To strengthen the adhesion between the filler and the polymer matrix, cement dust was treated with a stearic acid reaction. Composites are made by mixing different quantities of refined and raw cement dust (30, 50, 70, and 90 wt%) with virgin or recycled polystyrene. Mechanical properties, water absorption, and chemical resistance were used to demonstrate the suitability of formulated cement materials as building materials.

Chemical resistance and mechanical properties have improved after a week of immersion in water, 10% sodium chloride (NaCl), and 10% sodium sulphate (Na_2So_4) solutions, and water absorption has been delayed. The

**Corresponding Author:*
Hosam M. Saleh,
Radioisotope Department, Nuclear Research Center, Atomic Energy Egyptian Atomic Energy Authority, Cairo, Egypt;
Email: hosam.saleh@eaea.org.eg; hosamsaleh70@yahoo.com

DOI: https://doi.org/10.30564/jbms.v3i2.3082

recycled polystyrene composites filled with treated cement dust had the strongest abrasion resistance, weight loss, compressive and bending strength. Chemical resistance and mechanical properties have been improved, and water absorption has been delayed, after regular immersion in water, 10% sodium chloride (NaCl), and 10% sodium sulphate (Na_2SO_4) solutions. The highest abrasion resistance and lowest weight loss, as well as the greatest compressive and bending strength, were achieved with recycled polystyrene waste packed with treated cement dust. [2].

It is traditional practice to make concrete masonry units, such as concrete blocks or tiles, using portal cement in conjunction with aggregates. The previous technique has combined one section of cement with ten aggregate pieces, conventionally fine and rough aggregates, typically in the shape of sand and gravel or crushed stone. Limited quantities of other materials can be applied to facilitate or postpone reactions or to provide the desired properties to the cement. Portland cement is a mixture of calcium-aluminum-magnesia-silicate. The addition of water to a dry mixture of Portland cement results in a series of crystallization reactions that give concrete the strength required for use in construction industry. Due to the complexities of different chemical reactions, a great deal of study has been carried out to assess their effect on cured products, both in reaction conditions and in reactants. Such an investigation has an impact on the development of standardized quality standards for cement, as laid out by the American Association for Measuring Materials (ASTM). Materials such as sulfates, retardants, chlorides as accelerators, and pozzolans are among the various chemicals used in the processing of concrete and concrete block items. Although these pozzolans are not of cement quality or binding, they do interact with lime in the presence of water to form cementitious substances. Additives include products such as fly ash, silica dust, and silica-containing materials such as ground concrete, burnt shale, and some slag. Suitable fly ash formulations for the preparation of cement blocks include all of those fly ash compositions set out in ASTM C 618, 'Standard Specification for Fly Ash and Pure or Calcined Natural Pozzolan for use as a natural additive in Portland Cement Concrete [3].

In a global environment where the demand for quality housing is growing with an increased quality of life and a rising population, over-exploitation of natural resources as construction materials is becoming a significant issue. In this case, the incorporation of non-biodegradable waste materials into better construction materials would be highly useful. This report experimentally tested the use of expanded polystyrene mechanically recycled as 50 percent of total EPS for the composite foam concrete panel. The findings of the experimental program have been investigated concerning different useful structural behaviors in compression and flexicurity. The use of this foam concrete in combination with cement fiber boards results in a lightweight wall panel that can be used for both load-bearing and non-load-bearing walls in multi-story buildings. These light-weight panels allow for fast construction while also reducing the total weight of the building [4].

Construction has far-reaching social, economic, and environmental consequences. Given the materials used, such effects are dependent on the development of concrete, since it is the most widely used commodity, and its products are linked to the use of Portland cement, which accounts for a large portion of the industry's CO_2 emissions. The aim of this study was to investigate the use of recycled rubber in lightweight concrete with metakaolin, with the dual goal of reducing cement consumption while maintaining adequate strength. Metakaolin was created in the lab, and the minimum temperature for kaolin production was determined. Compressive strength, calorimetry, and mortar thermal conductivity measurements were used to evaluate lightweight concrete (in which sand was replaced by rubber). The researchers discovered that metakaolin produced at 800°C is more effective at replacing silica smoke. The 40% rubber mortar has a compressive strength of 20 MPa. This strength in light concrete allows for the production of materials with low cement consumption, such as mortar (22.9 kg of cement/m^3/MPa) and concrete (13 kg of cement/m^3/MPa). The concrete-rubber results revealed the best thermal conductivity indices, allowing building projects to be constructed more energy-efficiently, lowering their operating costs [5].

The mechanical properties of a wide variety of structural fine aggregates concrete mixtures are measured by a non-destructive ultrasonic testing process. This research includes about 84 different formulations checked between 3 and 180 days with compressive strengths ranging from 30-80 MPa. The effect of multiple influences on the relationship between ultrasonic pulse velocity and compressive intensity is investigated. These considerations include the form and quantity of cement, the quantity of water, the form of mixture, the initial wetting conditions, the type and volume of aggregate, and the partial substitution of the normal gross weight and fine aggregates with lightweight aggregates. Changing design parameters has a different effect on lightweight and standard weight concretes. The non-destructive ultrasonic pulse velocity test is also used to test the calculation of

 DOI: https://doi.org/10.30564/jbms.v3i2.3082

the mortar's strength properties. A generalized definition is proposed to estimate the compressive force based on the dependence of the ultrasonic pulse velocity on the stiffness and flexibility of concrete, regardless of the shape of concrete and its structure. More than 200 results were analyzed for different types of aggregates and concrete compositions, yielding a high correlation analysis [6].

Aggregates have low-cost volumes, containing between 66% and 78% of concrete. With growing concern about the unsustainable processing of natural and quality aggregates, the aggregate generated from industrial waste and agricultural waste is a viable new source of building materials. This review was undertaken to assess the feasibility of the use of coconut shells as aggregates in concrete. It is not only solves the issue of disposing of this solid waste but also helps preserve natural resources.

The crushed coconut shell aggregate's mechanical strength has been demonstrated. Rough aggregate is often used to represent fresh concrete properties such as density, slump, and 28-day compressive strength of lightweight concrete made from coconut shells. The results showed that the coconut shell aggregate had a high water absorption rate of about 24%, but the crushing value and impact value were comparable to other lightweight aggregates. The coconut shell concrete aggregates had an average fresh concrete density of 1975 kg/m^3 and a 28-day cubic compressive strength of 19.1 N/mm^2, respectively. It is concluded that crushed coconut shells are ideal for use as a replacement for traditional aggregates in the manufacture of light concrete [7].

In the presence and absence of enhanced additives, two difficult waste materials, cement kiln dust (CKD) and poly(styrene) (PS), were unutilized for the production of lightweight cementitious bricks suitable for subsequent building applications. To maximize the mechanical properties of the substance, various doses of Portland cement, iron slag, and crushed waste glass were mixed with the two main components (CKD and PS). The compressive strength, density, porosity, and water absorption of the various samples were evaluated under various conditions to determine their mechanical stability and physical properties. The microstructure of different sample compositions dependent on different variables has been studied using scanning electron microscopy (SEM), energy-dispersive X-ray (EDX), and spectroscopic analysis (FTIR and XRF). The mechanical strength results show that PS is unable to increase CKD reliability in the absence of other improved additives. In addition to CKD, 5% iron slag, 10% Portland cement, 10% ground waste glass, and 3% PS shredded waste were the required ratios for achieving an appropriate composite of feasible integrity. The nominated product has met the recommended value for building construction on outer shielding and internal non-loading walls, ensuring maximum mechanical and physical specifications in compliance with international standards. One of the benefits of this study is that it served two important roles for the environment: it consumed a by-product of environmental waste recycling, it was not financially costly, and it did not waste energy during its processing, and it primarily assisted us in getting rid of this waste [8].

2. Green Cement and Sustainability

Much research has been done to make adjustments to the cement manufacturing process to reduce greenhouse gas emissions from its manufacture. Approximately 50% of industrial pozzolana (cold ash or iron slag) has been suggested in the cement, thereby decreasing the emissions of carbon dioxide resulting from the burning of fuels into concrete clinker and also reducing pozzolan concrete mixing water [9]. The research competed in providing alternatives to traditional cement, and it used a type of industrial pozzolana, which is fly ash that is collected by special filters from combustion gases in electric power plants by burning coal. Where this ash is fine and the US produces about 70 million tonnes per year. Also, to the value of minimizing CO_2 emissions in natural or industrial pozzolana use [10].

Experiments also show that several significant qualities are the characteristics of this form of cement, such as its strength in soil and groundwater and resistance to natural factors, its low porosity, permeability, and thermal cracks, which influence conventional cement [11]. A team of Australian researchers sought to produce a new mixture of cement, using magnesium oxide with "Portland cement" to replace part of the limestone [12]. Consequently, the heating furnace temperature drops to about seven hundred degrees Celsius, which can be obtained by burning biofuels and some other fuels with lower carbon emissions. Despite the importance of this proposal, it soon turned out to be ineffective in reducing emissions, as the process of producing magnesium oxide is done by heating magnesium carbonate, and this process causes the emission of large quantities of carbonate gas [13].

Cement manufacturing is considered one of the developmental and strategic industries because it is directly related to the construction and reconstruction works, where cement is used as a hydraulic binder from building materials [14]. The cement industry may result in severe diseases as it contains compounds such as carbon, hydrogen, suspended particles, phosphorous, dust, smoke, fog, fumes, and others [15]. When cement

DOI: https://doi.org/10.30564/jbms.v3i2.3082

kilns are used to destroy components of hazardous waste, careful assessment of alternative disposal pathways is required, adherence to strict environmental, health, and safety standards, and no harm to the final product [15]. All these reasons have prompted most countries of the world to adopt the idea of sustainability and green buildings. Green buildings are buildings that provide a better life for people and take into account environmental standards at every stage of construction, design, implementation, operation, and maintenance, thus reducing the harmful environmental impact of the building on societies [16]. Sustainability is based on three main concepts, and the matter can only be correct by taking into account its variables; the economy, society, and the environment [16]. Green buildings are an integrated system that contributes through its ability to provide the consumption of types of cement that contribute to increasing the life span of the building, improving human health, and preserving the ecosystem in a way that reflects positively on the economy and productivity [17]. Various studies have been proposed to replace harmful types of cement with a by-product of rice husk as a partial substitute for ordinary Portland cement. Several studies have suggested optimal values for replacing rice husk ash, from 10% to 20%, which showed a significant improvement in the strength of the resulting mixed concrete [18]. However, these optimum values depend heavily on the burning preparation of rice husk ash that adversely affects the amorphous silica components and, consequently, the pozzolanic activities of the rice husk ash in the concrete [18]. A potential approach has been conducted to convert rice husk to be improved, highly reactive rice husk ash is provided by controlled combustion and milling. The results showed that mortar or concrete containing rice husk ash showed a notable reduction in mass loss when exposed to the hydrochloric acid solution and a significant decrease in the expansion of alkali, silica, and sulfate [19]. It is worth noting that around the world, 100 million tons of by-products are obtained from rice fields. Rice husk ash also has a good reaction when used as a partial substitute for cement. In another study, the results revealed that ash of coconut husk and rice husk used as alternatives to concrete, and it is one of the best sustainable and environmentally friendly products [20]. The mixed formulation had 20% coconut husk ash and 20% rice husk ash had 15.3% greater compressive strength than the reference formulation after aging 180 days. The mixtures of coconut husk ash and rice husk ash showed the highest compressive and pulling efficiency for all aging periods tested. Rice husk ash has a similar chemical composition to many organic fibersand composed of cellulose($C_5H_{10}O_5$), lignin ($C_7H_{10}O_3$), hemicellulose, silicon dioxide (SiO_2), and holocellulose [21]. Rice husk ash can differ according to the source and the processing type. The heating technique can also alter the overall chemical composition of the ash [22].

Silicate is one of rice husk ash's most essential components. During the firing process, the ingredients evaporate, and the only constituent left is silicates. Silicates are the component that gives the ability to react pozzolanic to rice husk ash [23].

3. Conclusions

Replacing cement with large quantities of fly ash and silica dust to develop new green cement and cohesive materials is a promising trend. It improves the use of renewable raw materials and alternative fuels by producing or improving cement with less energy consumption during manufacturing. The use of appropriate alternatives to Portland cement, particularly in construction industry such as fly ash, iron slag, and silica dust is very vital to minimize pollution. Also, attempts to use efficient recycling materials as an alternative to concrete aggregates, such as recycled aggregates, are becoming very significant.

References

[1] B. A. Herki, J. M. Khatib, and E. M. Negim, "Lightweight concrete made from waste polystyrene and fly ash," *World Appl. Sci. J.*, vol. 21, no. 9, pp. 1356-1360, 2013.

[2] J. N. Asaad and S. Y. Tawfik, "Polymeric composites based on polystyrene and cement dust wastes," *Mater. Des.*, vol. 32, no. 10, pp. 5113-5119, 2011.

[3] M. H. Wills Jr, "Concrete masonry units incorporating cement kiln dust." Google Patents, Oct. 04, 1983.

[4] P. L. N. Fernando, M. T. R. Jayasinghe, and C. Jayasinghe, "Structural feasibility of Expanded Polystyrene (EPS) based lightweight concrete sandwich wall panels," *Constr. Build. Mater.*, vol. 139, pp. 45-51, 2017.

[5] F. Pelisser, A. Barcelos, D. Santos, M. Peterson, and A. M. Bernardin, "Lightweight concrete production with low Portland cement consumption," *J. Clean. Prod.*, vol. 23, no. 1, pp. 68-74, 2012.

[6] J. A. Bogas, M. G. Gomes, and A. Gomes, "Compressive strength evaluation of structural lightweight concrete by non-destructive ultrasonic pulse velocity method," *Ultrasonics*, vol. 53, no. 5, pp. 962-972, 2013.

[7] K. Gunasekaran and P. S. Kumar, "Lightweight concrete using coconut shell as aggregate," in *Proceedings of the ICACC-2008. International conference on*

 DOI: https://doi.org/10.30564/jbms.v3i2.3082

advances in concrete and construction, Hyderabad, India, 2008, pp. 7-9.

[8] H. M. Saleh, A. A. Salman, A. A. Faheim, and A. M. El-Sayed, "Sustainable composite of improved lightweight concrete from cement kiln dust with grated poly (styrene)," *J. Clean. Prod.*, p. 123491, 2020.

[9] X. Shi, N. Xie, K. Fortune, and J. Gong, "Durability of steel reinforced concrete in chloride environments: An overview," *Constr. Build. Mater.*, vol. 30, pp. 125-138, 2012.

[10] Z. Giergiczny, "Fly ash and slag," *Cem. Concr. Res.*, vol. 124, p. 105826, 2019.

[11] S. Demirdag, "Effects of freezing-thawing and thermal shock cycles on physical and mechanical properties of filled and unfilled travertines," *Constr. Build. Mater.*, vol. 47, pp. 1395-1401, 2013.

[12] M. Schneider, M. Romer, M. Tschudin, and H. Bolio, "Sustainable cement production—present and future," *Cem. Concr. Res.*, vol. 41, no. 7, pp. 642-650, 2011.

[13] M. S. Imbabi, C. Carrigan, and S. McKenna, "Trends and developments in green cement and concrete technology," *Int. J. Sustain. Built Environ.*, vol. 1, no. 2, pp. 194-216, 2012.

[14] U. N. Environment, K. L. Scrivener, V. M. John, and E. M. Gartner, "Eco-efficient cements: Potential economically viable solutions for a low-CO_2 cement-based materials industry," *Cem. Concr. Res.*, vol. 114, pp. 2-26, 2018.

[15] P. K. Gupta, "Toxicologic Hazards of Solvents, Gases, Vapors, and Other Chemicals," in *Concepts and Applications in Veterinary Toxicology*, Springer, 2019, pp. 121-142.

[16] L. Zhang, J. Wu, and H. Liu, "Turning green into gold: A review on the economics of green buildings," *J. Clean. Prod.*, vol. 172, pp. 2234-2245, 2018.

[17] A. Alwisy, S. BuHamdan, and M. Gül, "Criteria-based ranking of green building design factors according to leading rating systems," *Energy Build.*, vol. 178, pp. 347-359, 2018.

[18] M. M. Hossain, M. R. Karim, M. Hasan, M. K. Hossain, and M. F. M. Zain, "Durability of mortar and concrete made up of pozzolans as a partial replacement of cement: A review," *Constr. Build. Mater.*, vol. 116, pp. 128-140, 2016.

[19] S. Donatello, A. Palomo, and A. Fernández-Jiménez, "Durability of very high volume fly ash cement pastes and mortars in aggressive solutions," *Cem. Concr. Compos.*, vol. 38, pp. 12-20, 2013.

[20] Z. A. Zeidabadi, S. Bakhtiari, H. Abbaslou, and A. R. Ghanizadeh, "Synthesis, characterization and evaluation of biochar from agricultural waste biomass for use in building materials," *Constr. Build. Mater.*, vol. 181, pp. 301-308, 2018.

[21] H. Moayedi, B. Aghel, H. Nguyen, and A. S. A. Rashid, "Applications of rice husk ash as green and sustainable biomass," *J. Clean. Prod.*, vol. 237, p. 117851, 2019.

[22] B. S. Thomas, "Green concrete partially comprised of rice husk ash as a supplementary cementitious material-A comprehensive review," *Renew. Sustain. Energy Rev.*, vol. 82, pp. 3913-3923, 2018.

[23] C. Sonat and C. Unluer, "Development of magnesium-silicate-hydrate (MSH) cement with rice husk ash," *J. Clean. Prod.*, vol. 211, pp. 787-803, 2019.

DOI: https://doi.org/10.30564/jbms.v3i2.3082

BILINGUAL PUBLISHING CO.
Pioneer of Global Academics Since 1984

Journal of Building Material Science
https://ojs.bilpublishing.com/index.php/jbms

ARTICLE

A Carbonation and Chloride Induced Corrosion Model for Hot-dip Galvanised Reinforcement Bar Material in Concrete

Xiaoshu Lü[1,2,3*] Tao Lu[1] Tong Yang[3]

1. Department of Electrical Engineering and Energy Technology, University of Vaasa, Vaasa, FIN-65101, Finland
2. Department of Civil Engineering, Aalto University, Espoo, FIN-02130, Finland
3. Faculty of Science and Technology, Middlesex University, London, UK

ARTICLE INFO

Article history
Received: 26 April 2021
Accepted: 15 June 2021
Published Online: 18 September 2021

Keywords:
Concrete corrosion
Carbonation and chloride
Hot-dip galvanised concrete reinforcement
Crack
Corrosion model

ABSTRACT

This paper focuses on methodological issues relevant to corrosion risk prediction models. A model was developed for the prediction of corrosion rates associated with hot-dip galvanised reinforcement bar material in concrete exposed to carbonation and chlorides in outdoor environment. One-year follow-up experiments, over five years, were conducted at various carbonation depths and chloride contents. The observed dependence of corrosion rate on the depth of carbonation and chloride content is complex indicating that the interaction between the carbonation and chloride influencing the corrosion. A non-linear corrosion model was proposed with statistical analysis to model the relationship between the corrosion rate and the test parameters. The main methodological contributions are (i) the proposed modeling approach able to take into account the uncertain measurement errors including unobserved systematic and random heterogeneity over different measured specimens and correlation for the same specimen across different measuring times, which best suits the measurement data; (ii) the developed model in which an interaction parameter is introduced especially to account for the contribution and the degree of the unobserved carbonation-chloride interaction. The proposed model offers greater flexibility for the modelling of measurement data than traditional models.

1. Introduction

The practice of hot-dip galvanised steel reinforcement bar (HDG) in concrete has been shown to be one of the most durable and technically suitable coating methods for corrosion protection [1-3]. In this method, zinc, in the form of hot dip galvanizing, is applied to the surface of steel forming zinc-iron alloy barrier around the steel which delays the onset of corrosion of the steel and enhances the durability of the concrete. HDG offers multifold advantages including substantially higher chloride threshold and lower corrosion rate for zinc corrosion in concrete than conventional steel. Furthermore, zinc's sacrificial action protects the steel even if the coating barrier is damaged.

However, HDG did not get wide acceptance in the past because inconsistent and contradictory results were observed under some conditions and environments [4-6].

**Corresponding Author:*
Xiaoshu Lü,
Department of Electrical Engineering and Energy Technology, University of Vaasa, Vaasa, FIN-65101, Finland; Department of Civil Engineering, Aalto University, Espoo, FIN-02130, Finland; Faculty of Science and Technology, Middlesex University, London, UK;
Email: xiaoshu.lu@univaasa.fi

 DOI: https://doi.org/10.30564/jbms.v3i2.3150

Uncertainties exist in the literature related to the effectiveness of HDG as a long-term inhibition for chlorides and carbonation induced corrosion. The controversy arises due to several reasons. One obvious reason is the exposure to oxygen, carbon dioxide, chlorides, water and other chemical exposures in an actual environment that the relation between environmental exposures and corrosion status can be quite complex. For example, at high PH-value conditions, corrosion may start at very low chloride content due to the zinc's instability at high PH-values. The corrosion attack is determined by the relevant environmental exposures, their interactions and time. Therefore, it has stated that laboratory results must be viewed with caution due to the fact that the simulated environment might not fully match the actual environments [5]. However, although complex, it has been well recognized that chlorides and carbonation are the two main causes for corrosion of steel in concrete. Aggressive substances of chlorides and carbon dioxide under certain environments, such as temperature and moisture, are the key risk factors. The presence of chlorides and carbon dioxide can lead to the breakdown of the steel's passivity which affects the inhibitive properties of the coating zinc and causes spalling of the concrete over corroded steel and, consequently, structural breakage.

Chloride and/or carbonation induced corrosion models, have been used extensively to predict the corrosion rate (see reviews [7-8]). Models can be classified as physical-based (or process-based) and data-driven methods generally. Physical-based methods use explicit mathematical equations to model evolution of the corrosion rate. Data-driven methods use measurement data to build up statistical models for predicting the corrosion process based on empirical relationships between corrosion rate and input parameters. Both models have their merits and demerits and challenges still exist in the current state-of-the-art corrosion modeling. A major limitation is the large gap between the general corrosion models, dominated by physically-based approaches, and the understanding of complexes encountered in real world situations. For example, time-dependent characteristic of the chloride concentration, or carbonation levels, at a concrete surface has been rarely considered in predicting the chloride or the carbonation ingress [9]. Data-driven modelling approaches are becoming more popular due to the increasing availability of measurement tools and data; however, methodological problems exist with such approaches because interpreting experimental findings strongly depend on the features of the data and the statistical methods for analyzing the data. For example, many measurement data involve multiple measures on each specimen. The correlated measures within specimens are not always considered in many studies. Moreover, correlation derived risk models for the in-service conditions are rare [10]. Not surprisingly, few reports have taken into account the complexity added by the interaction between chloride and carbonation in corrosion models. For risk assessment, the interaction between chloride and carbonation has a great influence on corrosion process and understanding the behavior of chloride, carbonation and their interaction is important for understanding how they induce the corrosion process [11]. The corrosion risk significantly increases when the concrete is exposed to both substances [11].

The purpose of this paper is to develop a correlation derived risk model for the prediction of the corrosion rate to address thesemethodological issues. The model predicts corrosion rates for hot-dip galvanised reinforcement bar material in concrete exposed to carbonation and chlorides in real world situations with regard to atmospheric attack in an outdoor environment. Long-term follow-up measurement data, one-year follow-up experiments for over five years, were conducted at various carbonation depths and chloride contents. A non-linear corrosion model was proposed with statistical analysis to model the relationship between the corrosion rate and the test parameters. From the methodological point of view, the main contribution of the present work consists in the approach developed to deal with the measurement errors including unobserved systematic and random heterogeneity over different measured specimens and correlation for the same specimen across different measuring times. Such issues are often neglected in the literature. Secondly, an interaction parameter was introduced especially to account for the contribution and the degree of the unobserved carbonation-chloride interaction. The proposed model offers greater flexibility for the modelling of measurement data than traditional models.

2. Methods and Materials

2.1 Measurement Data

The measurement data used in this study were collected from seven-year long-term follow up measurement. The data include 336 specimens of hot-dip galvanized reinforcement bar material in concrete exposed to carbonation and chlorides in real world situations with regard to atmospheric attack in outdoor environment. Corrosion rates on the depth of carbonation and chloride content were measured using PH indicator sprayed onto the freshly broken surface, which was possible to measure

DOI: https://doi.org/10.30564/jbms.v3i2.3150

the carbonation depth after a few minutes. The detailed experimental procedure can be referred from the paper [12].

2.2 Model

The proposed model predicts the corrosion rate given environmental exposures under real outdoor condition (i.e. different chloride concentration, carbonation level, etc). Since corrosion processes are complex which involves multiple environmental parameters, their interactions with each other and many uncertainties, the development of the model involved two stages. In the first stage, a suitable model structure and key risk parameters were selected using the Akaike information criterion [13]. In the second stage, the model equation was formulated. The proposed model has several new features that extend the current corrosion models in the literature:

(1) The model predicts time dependent corrosion rate base on full historical corrosion data;

(2) The model identifies the important environmental parameters as key risk conditions;

(3) The model takes into account the random and uncertain nature of different specimens and parameters over time.

(4) The model accounts for correlation among measured outcomes over time in the same specimen.

The model equation is based on a multivariate nonlinear regression as

$$y^{corr}_{it} = a_0 + a_1 \sqrt{t} + \beta_1 x^{CH}_{it} + \beta_2 x^{CO2}_{it} + \beta_3 x^{CH}_{it} . x^{CO2} + \gamma_1 x^{R}_{it} + u_i + \varepsilon_{it} \quad (1)$$

where

- y^{corr}_{it} presents the corrosion rate for the i-th specimen at time t
- x^{CH}_{it} is the chloride content for the i-th specimen at time t
- $x^{CO2}it$ is the carbonation level for the i-th specimen at time t
- x^{R}_{it} is the corrosion resistance for the i-th specimen at time t
- u_i is the random effect by specimens
- ε_{it} presents the measurement errors, random noise and other source of uncertainties
- a, β and γ are the model coefficients
- t represents the time

The model emphasizes the following aspects:

- accounts the random and uncertain nature of different specimens presented using random variable u_i
- accounts for correlation among measured outcomes over time in the same specimen: correlation (y^{corr}_{it}, $y^{cor}_{rit'}$) $\neq 0$
- accounts for all the measurement and modeling uncertainties using a stochastic variable ε_{it}.

The model relaxes the restriction that the measurements taken at different times for the same specimen are not correlated. Such uncorrelated restriction is one of the most common assumptions made in many corrosion models which can lead to misleading inferences because there is a good reason to believe that the correlations exist among the measurements for the same specimen at different time. For example, an average correlation coefficient for the corrosion rate measures of the same specimen is 0.5, which shows strong correlations. We shall demonstrate below in the discussion section that it is inaccurate and misleading to draw conclusions if such correlations are ignored. The correlation structure for the same specimen i was modeled as sphericity characteristic meaning that correlations of the measures for the same specimen are the same.

It can be seen that the model is a dynamic model in specimen and time. The novelty and generalization of the proposed model lie in the application of these new features. The model coefficients, a, β and γ, determine the effects on corrosion rates of their correspondent model parameters or environmental factors which were calculated by Maximum likelihood method (MLE) [14]. MLE provides better and more accurate results than least square method in general. Furthermore, time series analysis technique was used to test for the statistical significance of the effect of the estimate. Statistical significance is a statistical assessment of the probability that the relationship exists which presents the accuracy of the model. The significance is measured using p-value. Confidence interval ($p < 0.05$) was chosen as probability threshold for the statistical significance for the confidence level. After determining the significant parameters, the final models were developed incorporating only these parameters for different corrosion measurement outputs. The results are presented in the third section.

3. Results

Table 1 shows the results. Effect estimates are presented as 95% confidence intervals. p-values are provided which show the statistical significance of the effect estimates. For example, p<0.01 means 99% probability the true effect lies in that estimated interval. The sign of the estimate depends on the sign of the estimated slope of the model parameter. A positive sign means a positive correlation between the parameter and the model output.

Table 1 shows that chloride concentration, carbonation level, chloride-carbonation interaction, crack width and pH concentration were strongly predictive of corrosion

 DOI: https://doi.org/10.30564/jbms.v3i2.3150

Table 1. Significance Analysis of the Independent Variable

Parameter	Estimate	Standard Error	df	t	Sig.	95% Confidence Interval	
						Lower Bound	Upper Bound
a_0	-512,332810	96,613337	1224,352	-5,303	0,000	-701,878848	-322,786772
t	-172,593211	113,573595	1247,640	-1,520	0,129	-395,409522	50,223100
x^{CH}	-14,575465	5,515497	372,582	-2,643	0,009	-25,420871	-3,730058
x^{CO2}	27,867155	11,444345	344,743	2,435	0,015	5,357627	50,376684
x^{CH} x^{CO2}	-4,378792	3,431653	532,164	-1,276	0,203	-11,120040	2,362456
x^{R}	75,400366	37,197950	1088,903	2,027	0,043	2,412597	148,388135

Table 2. Parameter Estimates (Dependent Variable: y^{corr})

Parameter	Value	Standard Error	t	Sig.	95% Confidence Interval	
					Lower Bound	Upper Bound
a_0	-126,373	87,521	-1,444	0,149	-298,056	45,310
t	-638,260	103,055	-6,193	0,000	-840,415	-436,104
x^{CH}	-28,219	3,553	-7,942	0,000	-35,188	-21,249
x^{CO2}	-19,066	6,026	-3,164	0,002	-30,887	-7,246
$x^{CH}x^{CO2}$	-4,968	2,107	-2,358	0,019	-9,102	-0,835
x^{R}	-23,967	35,353	-0,678	0,498	-93,316	45,382

rate. Chloride concentration, carbonation depth and crack width had the same, or nearly the same, significant positive effect per unit on corrosion rate. Increased chloride concentration, carbonation depth and crack width had progressively increasing effect on y^{corr}. The results indicate the PH concentration could induce the increase of the corrosion rate too. An interesting result was obtained here regarding the chloride-carbonation interaction. The interaction was found to have a significant impact on corrosion rate. Association between y^{corr} and the interaction depended on the levels of both factors. Roughly speaking, y^{corr} can be expected to change by 1.8+0.35x when chloride concentration increases by 1 given x depth of carbonation. The increase of y^{corr} is about 1.4+0.35CH when carbonation depth increases by 1 given CH concentration of chloride.

For higher concentration of CH, significant higher y^{corr} was present at higher levels of carbonation (13 mm depth) than at lower level of carbonation (11 mm). The study also shows that y^{corr} is in inverse proportion with the square-root of exposure time. The increase of y^{corr} slows down in time.

Corrosion rate has shown to be strongly dependent on chloride concentration, carbonation level, PH concentration but has a weak dependence on crack growth (significance at the 8% level). Increases of carbonation, pH values and crack width have been found to potentially increase the corrosion rate. At pH 7-8 (the average pH used in this study) the corrosion potential decreases significantly with the increase of chloride concentrations. From the experiments it is not apparent that the exposure times are correlated with y^{corr}.

4. Discussion

4.1 Methodological Issues

One of the most striking features of the proposed methodology is that it allows for taking into account the uncertain measurement errors including unobserved systematic and random heterogeneity over different measured specimens and correlation for the same specimen across different measuring times, which best suits the measurement data. Misleading inferences could be obtained if we neglect such measuring correlations within specimens. Figure 1 illustrates the specimen-based corrosion rate changes in our experimental data which are subject to random fluctuations. A linear regression trend line fitted to all the specimens' lines is displayed in the figure which roughly shows a positive relationship between carbonation depth variation and corrosion rate. Therefore, simple regression models fail to capture randomness between-specimen fluctuations and the correlations within specimen. The model's standard errors are biased and the model results are inaccurate. Because of space limitations, we only show the comparison results for y^{corr}. Such inaccurate predictions existed in the calculation of other corrosion outputs as well.

The presence of the correlations among y^{corr} measures for the same specimen introduces methodological problems in significance testing. The correlations

DOI: https://doi.org/10.30564/jbms.v3i2.3150

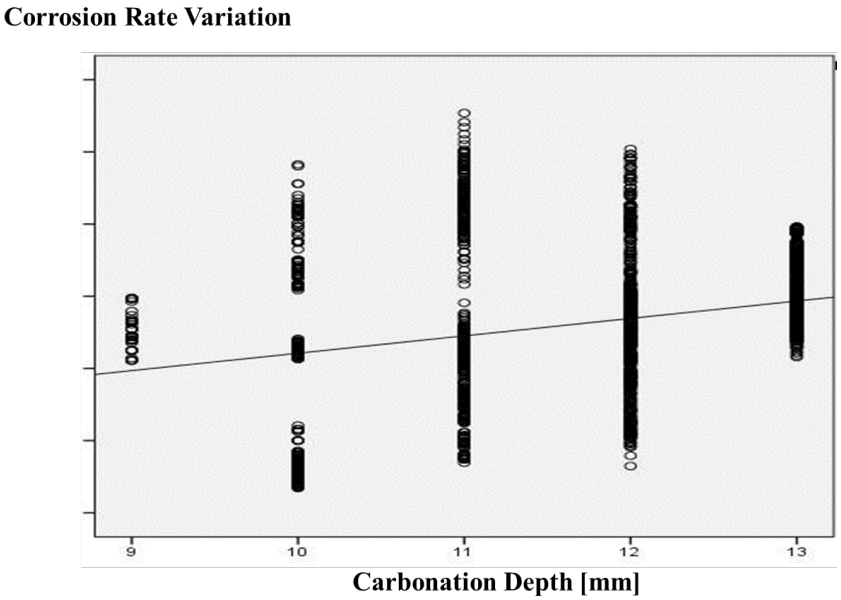

Figure 1. The specimen-based corrosion rate variation vs carbonation depth. Circles represent the specimens. Large variation in specimen can be observed. A linear relationship indicates a correlation between them.

indicate nested sources of variation. If we ignore it, we underestimate the error variance of the estimated coefficients and inflate the significance levels. This can increase the likelihood of a Type I error. The existence of such correlations has been rarely been taken into account in the corrosion models.

4.2 Chloride and Carbonation Interaction

The interaction effect between chloride and carbonation on corrosion rate was identified in this study. Although research on this topic is lacking because most studies have focused on the chloride and carbonation penetrations independently, relatively few studies have demonstrated that their combination could lead to rapid deterioration [15]. Therefore, these results are consistent with the large body of scientific evidence although there are disputes on some levels in the literature.

The change of structure due to carbonation can reduce the binding capacity of the solid phase in concrete leading to a higher amount of free chlorides in the pore solution. The coexistence of chloride and carbonation is related to the effect of carbonation on the liberation of bound chlorides leading to a higher penetration rate and higher corrosion rate. However, for chloride, penetration only occurs in pores that contain water which is completely different from that of carbonation [16]. One report suggested that once the carbonation front reaches the rebar location. The chloride concentration threshold needed to initiate corrosion could be significantly reduced [17].

5. Conclusions

Corrosion risk prediction models of concrete structures have been widely studied in the literature. This paper developed a model for the prediction of corrosion rates associated with hot-dip galvanised reinforcement bar material in concrete exposed to carbonation and chlorides in outdoor environment. Our proposed modelling approach adds some new methodological aspects to these important studies, namely, (i) able to take into account the uncertain measurement errors including unobserved systematic and random heterogeneity over different measured specimens and correlation for the same specimen across different measuring times, which best suits the measurement data; (ii) detailed study of the contribution and the degree of the unobserved carbonation-chloride interaction.

Among the study factors, chloride, carbonation, chloride-carbonation interaction, crack width, pH concentration and exposure time were found to be associated with the corrosion risk. This is the first study accounting for randomness between-specimen fluctuations and the correlations within specimen and experimental finding indicating that the chloride-carbonation interaction has noticeable effect on corrosion. Our study results suggest that there is potential for reducing corrosion risk by controlling the risk factors.

Finally, the developed model offers greater flexibility for the modelling of corrosion data and the proposed modeling approach is easily implemented in common statistical software packages with small computational load.

 DOI: https://doi.org/10.30564/jbms.v3i2.3150

Acknowlegments

This study is financed by the Academy of Finland (Grant number 324023) Dr. Esko Sistonen provided the experimental data.

References

[1] Tonini, DE., Gaidis, JM (1980) "*Corrosion of reinforcing steel in concrete*" A symposium, ASTM (Philadelphia), Conference Proceedings, 204p.

[2] Yeomans, SR (1994) Proceedings of International Conference held at the University of Shieffield. (Ed. R.N.Swamy), 24-28 July 1994, Sheffield Academic Press.

[3] Yeomans, SR (Ed.), Galvanized steel reinforcement in concrete, Elsevier (2004).

[4] Fratesi, G., Moriconi, IC. (1996) "*The influence of steel galvanization on rebars behaviour in concrete*", Page, CL., Bamforth, PB., Figg JW (Eds.), Corrosion of Reinforcement in Concrete Construction, Royal Society of Chemistry (1996), pp. 630-641.

[5] Swamy, RN (1990) "Resistance to chlorides of galvanized rebars", Page, CL., Treadaway, KWJ., Bamforth PB (Eds.), Corrosion of Reinforcement in Concrete, Elsevier Appl. Sci, London, New York, pp. 586-600.

[6] Sergi, G., Short, NR, Page, CL (1985) Corrosion, 41, Allen Press.

[7] Reale, T., O'Connor, A (2012) A review and comparative analysis of corrosion-induced time to first crack models, Construction and Building Materials, 36, 475-483.

[8] Otieno, M., Beushausen, H., Alexander, M (2012) Prediction of corrosion rate in reinforced concrete structures - a critical review and preliminary results, Mater. Corros., 63, 777-790.

[9] Ann, KY., Ahn, JH., Ryou. JS (2009) The importance of chloride content at the concrete surface in assessing the time to corrosion of steel in concrete structures, Construction and Building Materials, 23, 239-245.

[10] Otaduy, P., Karagiozis, A (2010) "*Corrosion Prediction in Buildings Based on Simulation of Temporal Distribution of Humidity and Temperatures and the International Standard ISO-9223*", Proceedings of Thermal Performance of Exterior Envelopes of Whole Buildings XI, ASHRAE, 2010.

[11] Pular, P (1987) Corrosion Damaged Concrete, First Edition, Butterworths, p99, London, UK.

[12] Sistonen, E., Puttonen, J (2010) "*Durability study of hot-dip galvanized reinforcement bars in carbonated and chloride-contaminated concrete*". 3rd fib International Congress, May 29 - June 3, Washington D.C., USA.

[13] Akaike, H (1974) A new look at the statistical model identification". IEEE Transactions on Automatic Control, 1974, 19 (6), 716-723.

[14] Ross, SM (2014) Introduction to probability and statistics for engineers and scientists, Academic Press.

[15] Lacasse, MA., Vanier, DJ (1999) "*Durability of Building Materials and Components 8: Durability of building assemblies and methods of service life prediction*", NRC Research Press National Research Council of Canada, 1999.

[16] Costa, A., J. Appleton, J (2001) Concrete carbonation and chloride penetration in a marine environment, Concrete Science and Engineering, 3, 242-249.

[17] Boulfiza, M., Sakai, K., Banthia, N., Yoshida, H (2003) Prediction of Chloride Ions Ingress in Uncracked and Cracked Concrete. ACI Materials Journal. 100, 38-48.

DOI: https://doi.org/10.30564/jbms.v3i2.3150

BILINGUAL PUBLISHING CO.
Pioneer of Global Academics Since 1984

Journal of Building Material Science
https://ojs.bilpublishing.com/index.php/jbms

ARTICLE

New Approach and Alternate Criterion for Heat-transfer Analysis of Building Walls and Its Applications

Yu Zhang[1,2*] Xu Zhang[1]

1. Building Design Institute, China Academy of Building Research, Beijing, 100013, China
2. Department of Building Science, Tsinghua University, Beijing, 100084, China

ARTICLE INFO

Article history
Received: 16 April 2021
Accepted: 28 June 2021
Published Online: 18 September 2021

Keywords:
Heat transfer
Thermal resistance
Capacitance
Entransy
Impedance

ABSTRACT

Energy consumed by buildings accounts for approximately one-third of the total energy consumption of the society. Moreover, energy systems employed in buildings emit hazardous pollutants, such as, NOx, PM2.5 and CO_2, into the environment. Consequently, increasing the energy efficiency of buildings constitutes an important problem concerning the field of building-energy and environment conservation. Thermal resistance and capacitance are two important thermophysical properties of building walls significantly impacting their heat-transfer performance. Traditional theories concerning these properties, however, face certain limitations: (1) the concept of thermal resistance is only valid for one-dimensional, steady heat conduction without existence of an internal heat source; (2) thermal resistance and capacitance are relevant, and can, therefore, not be used to analyze heat-transfer and storage performance, respectively, of building walls. Based on the entransy-dissipation-based impedance theory, a new approach towards realization of heat-transfer analysis and optimization has been proposed in this study. The weightiness of thermal resistance and capacitance with regard to heat-transfer performance has been described along with deduction of the corresponding substitutional relation via illustrative examples. The proposed approach has been demonstrated to effectively overcome aforementioned limitations of building energy conservation problems.

1. Introduction

Modern building structures consume too much energy and emit a number of hazardous pollutants, such as NOx, PM2.5, and CO_2 into the atmosphere. Consequently, increasing the energy efficiency of buildings constitutes an important problem concerning building energy conservation.

Envelopes of modern buildings result in creation of major heating and cooling loads. Therefore, construction of an appropriate building envelope is an effective means of adjusting the heat-transfer rate and reducing the energy consumption of buildings. Thermal resistance and capacitance greatly impact the heat-transfer performance of building walls, and using these two parameters, one can analyze and optimize the heat-transfer performance of buildings, which in turn, would lead to construction of energy-saving building walls. Extant studies have

**Corresponding Author:*
Yu Zhang,
Building Design Institute, China Academy of Building Research, Beijing, 100013, China; Department of Building Science, Tsinghua University, Beijing, 100084, China;
Email: sdjyzhq@163.com

 DOI: https://doi.org/10.30564/jbms.v3i2.3103

traditionally used only the thermal resistance and retaining-heat parameters to optimize the construction of building walls. Asan et al. [1,2] numerically explored the effect of different arrangements of wall materials on the time lag and decrement factor concerning the outdoor-air temperature as well as the relationship between these. Corresponding influencing factors were subsequently determined. Studies by del Coz Dıaz et al. [3,4], Bouchair [5], and Li et al. [6] investigated optimization of the hollow-brick design based on the concept of equivalent thermal conductivity to realize high heat-insulation performance. However, thermal resistance and the retaining-heat parameter are not entirely independent in unsteady heat-transfer processes. Consequently, these cannot be used to analyze heat transfer and storage performances of building walls.

Recently, Guo et al. [7] proposed the concept of entransy—defined as half the product of internal energy and temperature ($G = ½\ U \times T$) (U and T denote the internal energy and temperature of a system). It has been observed that entransy dissipation occurs during heat-transfer processes owing to the existence of thermal resistance. Based on this result, thermal resistance can be defined as the ratio of the entransy-dissipation rate to square of the heat flow, and this definition of thermal resistance can be uniquely determined under a known temperature distribution. The said entransy-dissipation-based thermal resistance has been widely employed in the optimization of heat-transfer processes [8-18].

Based on the entransy method, the proposed study aims at decoupling the thermal resistance and capacitance with regard to unsteady heat-transfer processes, thereby subsequently illustrating weightiness of these two properties in heat-transfer processes and thence deducing the substitutional relationship between them.

2. Definition of Entransy-dissipation-based Thermal Resistance and Capacitance in Unsteady Heat-transfer Processes

For a general heat-conduction process occurring across a wall, the thermal energy conservation equation can be expressed as

$$\rho c_p \frac{\partial T}{\partial t} = -\nabla \cdot \boldsymbol{q}, \tag{1}$$

where ρ and cp denote the density and constant-pressure volumetric specific heat of the wall, respectively; T denotes wall temperature; t represents time; and $\boldsymbol{q}$ denotes the heat-flow density. Multiplying both sides of Equation (1) by temperature T yields the balance equation of entransy during heat-transfer processes [19] expressed as

$$\rho c_p T \frac{\partial T}{\partial t} = -\nabla \cdot (\boldsymbol{q} T) + \boldsymbol{q} \cdot \nabla T, \tag{2}$$

Terms on the left of the equality in Equation (2) denote the time variation of entransy stored per unit wall volume. Correspondingly, two terms exist on the right of the equality sign. The first denotes entransy transferred from one part of the wall to another while the second refers to the local entransy-dissipation rate during heat conduction. It can be seen from Equation (2) that entransy is dissipated as heat-transfer proceeds from a high-temperature zone of the wall to a low-temperature one.

Introducing the temperature of surrounding air into Equation (2), one gets

$$\rho c_p T \frac{\partial T}{\partial t} = -\nabla \cdot [\boldsymbol{q}(T - T_e)] - \nabla \cdot (\boldsymbol{q} T_e) + \boldsymbol{q} \cdot \nabla T, \tag{3}$$

where T_e denotes the temperature of surrounding air.

Integrating the entransy balance equation Equation (3) over the entire heat-conduction domain and transforming volume integrals to surface integrals over the domain boundary using the Gauss Law, Equation (4) can be obtained.

$$\iint_{\partial} -(\boldsymbol{q} T_e) \cdot \boldsymbol{n} \mathrm{d}S - \iiint \rho c_p T \frac{\partial T}{\partial t} \mathrm{d}V = \iiint k \nabla T \cdot \nabla T \mathrm{d}V + \iint -\boldsymbol{q}(T_e - T) \cdot \boldsymbol{n} \mathrm{d}S, \tag{4}$$

where $\boldsymbol{n}$ denotes the unit outward normal vector on the wall surface; Σ denotes surface integral area; Ω represents volume integral area, and S and V denote the area and volume of the wall, respectively.

Based on Equation (4), heat-transfer impedance can be defined in accordance with the thermoelectricity analogy and described as follows by Equation (5).

$$\begin{aligned} Z_h = \frac{T_1 - T_2}{\dot{Q}_h} &= \frac{\dfrac{\iint_{\partial_1} -(\boldsymbol{q} T_e) \cdot \boldsymbol{n} \mathrm{d}S}{\iint_{\partial_1} -\boldsymbol{q} \cdot \boldsymbol{n} \mathrm{d}S} - \dfrac{\iint_{\partial_2} (\boldsymbol{q} T_e) \cdot \boldsymbol{n} \mathrm{d}S}{\iint_{\partial_2} \boldsymbol{q} \cdot \boldsymbol{n} \mathrm{d}S}}{\iint_{\partial_2} \boldsymbol{q} \cdot \boldsymbol{n} \mathrm{d}S} \\ &= \frac{\dot{\Phi}_h + \iiint_U \rho c_p T \frac{\partial T}{\partial t} \mathrm{d}V - \dfrac{\iint_{\partial_1} -(\boldsymbol{q} T_e) \cdot \boldsymbol{n} \mathrm{d}S \times \iiint \rho c_p \frac{\partial T}{\partial t} \mathrm{d}V}{\iint_{\partial_1} -\boldsymbol{q} \cdot \boldsymbol{n} \mathrm{d}S}}{(\iint_{\partial_2} \boldsymbol{q} \cdot \boldsymbol{n} \mathrm{d}S)^2} \\ &= \frac{\dot{\Phi}_{h,R} + \Delta \dot{G}_C}{\dot{Q}_h^2} = \frac{(T_1 - T_2)^2}{\dot{\Phi}_{h,R} + \Delta \dot{G}_C}, \end{aligned} \tag{5}$$

$$\dot{\Phi}_{h,R} = \dot{\Phi}_h, \tag{6}$$

$$\Delta \dot{G}_C = \iiint_U \rho c_p T \frac{\partial T}{\partial t} \mathrm{d}V - \frac{\iint_{\partial_1} -(\boldsymbol{q} T_e) \cdot \boldsymbol{n} \mathrm{d}S \times \iiint \rho c_p \frac{\partial T}{\partial t} \mathrm{d}V}{\iint_{\partial_1} -\boldsymbol{q} \cdot \boldsymbol{n} \mathrm{d}S}, \tag{7}$$

DOI: https://doi.org/10.30564/jbms.v3i2.3103

Here, subscripts 1 and 2 represent the two wall boundaries; Q_h represents the total heat flow rate; $\Phi_{h,}R$ denotes the entransy dissipation rate due to thermal resistance of the wall; and ΔG_C represents the entransy variation rate owing to thermal capacitance.

Based on the above discussion, the thermal resistance R_h and capacitance X_h can be decoupled from the heat-transfer process and expressed as follows.

$$R_h = \frac{(T_1 - T_2)^2}{\dot{\Phi}_{h,R}} \tag{8}$$

$$X_h = \frac{(T_1 - T_2)^2}{\Delta \dot{G}_C} \tag{9}$$

The entransy-dissipation-based thermal resistance R_h and capacitance X_h are different from traditional thermal resistance R and retaining-heat parameter S in that the heat-transfer and heat-storage processes can be completely characterized by the thermal resistance R_h and capacitance X_h, respectively.

3. Illustrative Example 1: Weightiness of Thermal Resistance and Capacitance in with regard to Building-wall Heat-transfer Processes

In accordance with the definition of thermal resistance R_h and capacitance X_h, values of R_h and X_h can be easily calculated for a wall of a given room using Equations (8) and (9). Subsequently, the weightiness of thermal resistance and capacitance during the heat-transfer process can be determined.

3.1 Calculation model

A simplified two-plate room model [20] was considered in this study. In the said model, the internal wall, floor, and ceiling were modeled as a single plate. An external wall, to where a south-facing window was fixed [21] was modeled using another plate. The transient heat-conduction equation for the said plate modeled could be expressed as follows [21].

$$\rho_p c_{p,p} \frac{\partial t_p}{\partial \tau} = \frac{\partial}{\partial x}\left(k_p \frac{\partial t_p}{\partial x}\right), \tag{10}$$

Boundary conditions for Equation (10) can be expressed as [21]

$$h_{out}(t_{out,a} - t_{p,out}) + q_{r,p,out} = -k_p \left.\frac{\partial t_p}{\partial x}\right|_{x=0}, \tag{11}$$

$$h_{in}(t_{in,a} - t_{p,in}) + q_{r,p,in} = k_p \left.\frac{\partial t_p}{\partial x}\right|_{x=L_p}, \tag{12}$$

The initial condition for Equation (10) can be expressed as [21]

$$t_p(x,\tau)\big|_{\tau=0} = t_{p,init}, \tag{13}$$

where ρ_p, $cp_{,p}$, and k_p denote the density, constant-pressure volumetric specific heat, and thermal conductivity of the plate, respectively; t_p refers to the plate temperature; τ and x indicate time and space coordinates, respectively; h_{out} and h_{in} denote convective heat-transfer coefficients corresponding to the outer and inner plate surfaces, respectively, which could be calculated with reference to the ASHRAE Handbook [22]; $t_{out,a}$ and $t_{in,a}$ denote outdoor and indoor air temperatures, respectively, while $t_{p,out}$ and $t_{p,in}$ denote temperatures of the outer and inner plate surfaces, respectively; $q_{r,p,out}$ and $q_{r,p,in}$ represent thermal radiation heat fluxes corresponding to the outer and inner plate surfaces, respectively; L_p denotes plate thickness; and lastly, $t_{p,init}$ denotes the initial plate temperature [21].

Heat-transfer equations for the double-glazed window could be expressed as [21]

$$\rho_{win,1} c_{p,win,1} L_{win,1} \frac{\partial t_{win,1}}{\partial \tau} = h_{out}(t_{out,a} - t_{win,1}) + h_{1,2}(t_{win,2} - t_{win,1}) + q_{r,win,1}, \tag{14}$$

$$\rho_{win,2} c_{p,win,2} L_{win,2} \frac{\partial t_{win,2}}{\partial \tau} = h_{in}(t_{in,a} - t_{win,2}) + h_{1,2}(t_{win,1} - t_{win,2}) + q_{r,win,2}, \tag{15}$$

where ρ_{win} and $cp_{,win}$ denote the density and constant-pressure volumetric specific heat of the window; subscripts 1 and 2 refer to the outer and inner glass layers, respectively; L_{win} and t_{win} denote the thickness of glass and it temperature, respectively; $q_{r,win}$ denotes the thermal radiation heat flow density of the window; and lastly, $h_{1,2}$ denotes the overall heat-transfer coefficient between the two glasses expressed as

$$h_{1,2} = \frac{1}{\frac{1}{U_{win}} - \frac{1}{h^*_{out}} - \frac{1}{h^*_{in}}}, \tag{16}$$

where U_{win} denotes the overall heat-transfer coefficient of the window while h^*_{out} and h^*_{in} refer to convective heat-transfer coefficients of the outer and inner window surfaces, respectively.

The energy-conservation equation is [21]

$$V_R \rho_a c_{p,a} \frac{\partial t_{in,a}}{\partial \tau} = \sum_{j=1}^{2} Q_{p,j} + Q_{win} + Q_{d,c} + Q_{ven}, \tag{17}$$

where V_R denotes the room volume; ρ_a and $cp_{,a}$ denote the density and constant-pressure volumetric specific heat of air; $Q_{p,j}$, Q_{win}, $Q_{d,c}$, and Q_{ven} refer to convective

 DOI: https://doi.org/10.30564/jbms.v3i2.3103

heat-transfer rates between the two plates and indoor air, window and indoor air, heat-transfer rate due to presence of internal heat sources, and that due to natural ventilation. Values of $Q_{p,j}$, Q_{win} and Q_{ven} could be obtained using following equations.

$$Q_{p,j} = h_{in} \times (t_{p,in,j} - t_{in,a}) \times A_{p,j}, \quad (18)$$

$$Q_{win} = h_{in} \times (t_{win,2} - t_{in,a}) \times A_{win}, \quad (19)$$

$$Q_{ven} = V_R \rho_a c_{p,a} \times ACH \times (t_{out,a} - t_{in,a}) / 3600, \quad (20)$$

wherein A_p and A_{win} denote areas of the plate and window while ACH represents air change per hour.

3.2 Calculation Conditions

Table 1 summarizes building parameters. In the following calculations, typical rooms in seven representative Chinese cities located in regions with different climatic conditions were considered (refer Table 2). Climate data for the seven cities were generated using the Chinese Architecture-specific Meteorological Data Sets for Thermal Environment Analysis.

3.3 Results Analysis

Calculation results for values of thermal resistance R_h and capacitance X_h of the external wall plate of the building in different cities are depicted in Figures 1–4.

Table 1. Building parameters [20,21]

Category	Parameters
Dimension	5.7 m (depth) × 3.6 m (width) × 3.2 m (height)
Wall and window	External reinforced concrete: 0.17 m; ρcp = 2.3 MJ/m^3 K; k = 2 W/m K External polystyrene board: 0.08 m; ρcp = 0.048 MJ/m^3 K; k = 0.047 W/m K External wall plate:0.25 m; ρcp = 1.58 MJ/m^3 K; k = 0.14 W/m K Solar radiation absorptance of external wall plate: 0.6 Ceiling and floor: 0.2 m; ρcp = 2.3 MJ/m^3 K; k = 2 W/m K Internal wall: 0.2 m; ρcp = 0.84MJ/m^3 K; k = 0.41 W/m K Internal wall plate: 0.2 m; ρcp = 1.5 MJ/m^3 K; k = 1 W/m K Double-glazing: 2.0 m (length) × 1.7 m (width) Overall heat-transfer coefficient: 3.1 W/m^2 K SC = 0.67 (winter), SC = 0.44 (summer)
ACH	5.0 h^{-1} (outdoor temperature measured between 293 K and 299 K) 0.75 h^{-1} (others)
Internal heat sources	10.6 W/m^2
Convective heat-transfer coefficient	h_{out} = 23.3 W/m^2 K h_{in} = 1.31($\triangle$ t)$^{1/3}$ [22]

Table 2. Climatic characteristics of different cities [20] considered in this study

Regions	Latitude	January		July		Climate Type
	(o)	Average temperature (◦C)	Average solar radiation (Wm^{-2})	Average temperature (◦C)	Average solar radiation (Wm^{-2})	
Harbin	45.75	-21.8	67.4	22.9	209.1	Severe cold
Urumchi	43.78	-18.2	56.8	25.0	261.6	Severe cold
Beijing	39.93	-3.6	97.8	25.3	205.0	Cold
Shanghai	31.17	3.7	86.7	29.2	188.9	Hot summer and cold winter
Lhasa	29.67	-0.2	189.8	15.4	270.3	Cold
Kunming	25.02	7.5	168.1	19.5	180.0	Moderate
Guangzhou	23.13	9.4	103.1	27.8	166.5	Hot summer and warm winter

DOI: https://doi.org/10.30564/jbms.v3i2.3103

From the figures, it can be concluded that the weightiness of capacitance X_h exceeds that of thermal resistance R_h as regards the building external wall in summer. That is, heat storage plays a significant role in thermal processes that occur in buildings, and that optimization of the heat-storage process is more efficient compared to that of heat-transfer. Meanwhile, it was observed that the value of capacitance X_h was minimum in Harbin, whereas it was maximum in Lhasa.

Using the same method, values of the thermal resistance R_h and capacitance X_h during winter were calculated for the seven different cities. In this case, the weightiness of thermal resistance R_h was observed to exceed that of capacitance X_h for the building external wall, thereby implying that heat transfer plays a major role in the thermal process of buildings during winter, and that optimization of the heat-transfer process during winters is more efficient compared to that of the heat-storage process. As observed, the thermal resistance R_h was minimum in Kunming while that in Harbin was maximum.

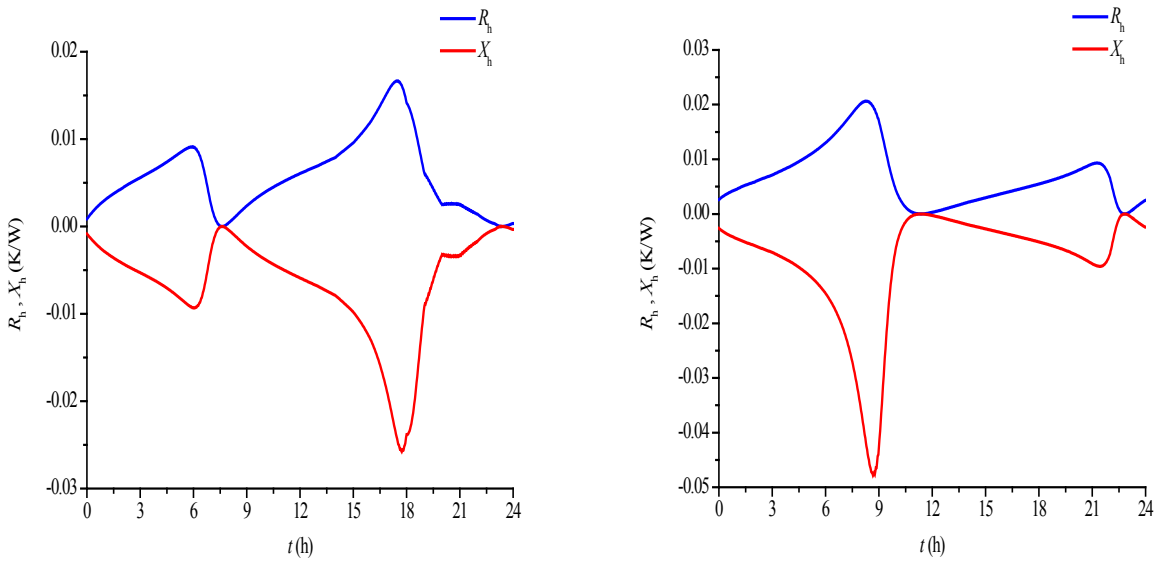

Figure 1. Thermal resistance R_h and capacitance X_h in Harbin and Urumchi during summer

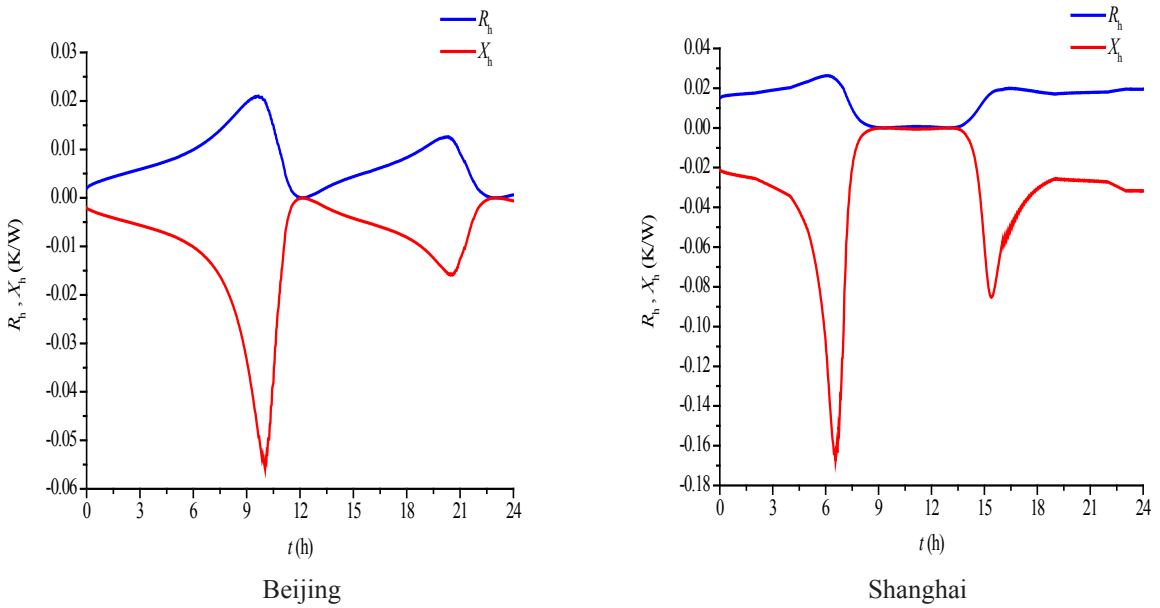

Figure 2. Thermal resistance R_h and capacitance X_h in Beijing and Shanghai during summer

 DOI: https://doi.org/10.30564/jbms.v3i2.3103

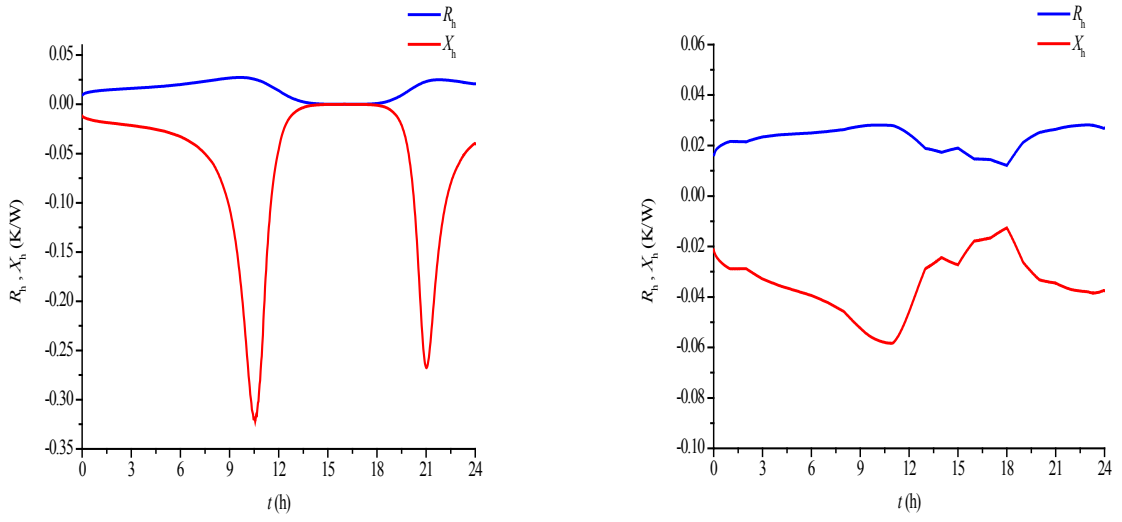

Lhasa Kunming

Figure 3. Thermal resistance R_h and capacitance X_h in Lhasa and Kunming during summer

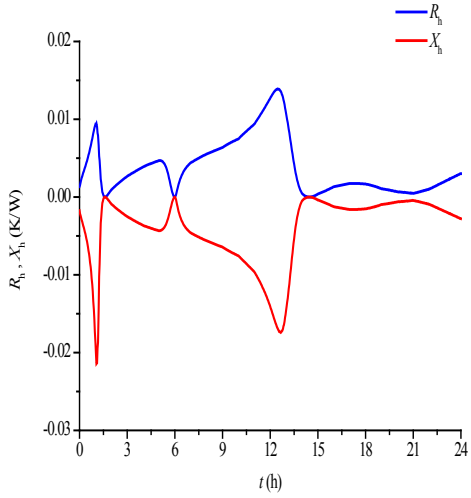

Figure 4. Thermal resistance R_h and capacitance X_h in Guangzhou during summer

4. Illustrative Example 2: Substitutional Relationship between Thermal Resistance and Capacitance

Combining Equations (5)–(9), the following relationship between thermal resistance R_h and capacitance X_h can be deduced.

$$\frac{1}{Z_h} = \frac{1}{R_h} + \frac{1}{X_h} \tag{21}$$

It can, therefore, be demonstrated that thermal resistance R_h and capacitance X_h maintains an alternative relationship.

Multiplying both sides of Equation (21) by $(T_2 - T_1)$ and integrating the equation over the time domain yields

$$Q = \int_t \frac{T_1 - T_2}{R_h} + \int_t \frac{T_1 - T_2}{X_h}, \tag{22}$$

where Q denotes the total heat transferred from outdoors to indoors in accordance with the building external wall plate.

For given values of k and ρcp of the building external wall plate, the value of Q can be calculated using Equation (22). Likewise, for another value of k, one could calculate the value of ρcp in accordance with Equation (22) under the condition that values k and Q are known.

The same room described in Table 1 was used to illustrate the said alternate relation. Figure 5 depicts the analysis result. As can be observed, the thermal conductivity k and constant-pressure volumetric specific heat ρcp of the building external wall plate in Beijing over an entire year demonstrates an approximate quadratic-function distribution.

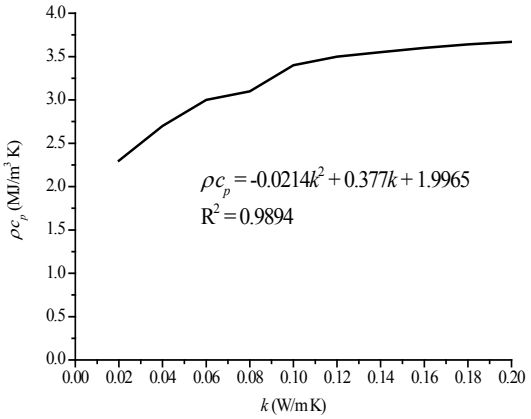

Figure 5. Substitutional relationship between k and ρc*p* in Beijing over a one-year duration.

DOI: https://doi.org/10.30564/jbms.v3i2.3103

5. Conclusions

Entransy-dissipation-based thermal resistance and capacitance of a building wall during unsteady heat transfer have been defined and decoupled in the proposed research. Accordingly, solutions to the following problems can be obtained.

(1) The weightiness of thermal resistance and capacitance during unsteady heat-transfer processes can be determined to guide the optimization of building wall structures. The heat-transfer and heat-storage processes can, accordingly, be pertinently optimized for transient heat-transfer problems.

(2) An alternate relationship between thermal resistance and capacitance can be established, and the same can be used to construct economical wall structures under the premise of ensuring optimum thermal performance of buildings.

(3) The proposed study provides a novel and in-depth view towards understanding unsteady heat-transfer processes, thereby addressing several problems related to building energy conservation.

Acknowledgements

The author(s) disclosed receipt of the following financial support for the research, authorship, and/or publication of this article: the Youth Science Research Foundation of China Academy of Building Research (20160118331030053).

References

[1] Asan H. Investigation of wall's optimum insulation position from maximum time lag and minimum decrement factor point of view. Energy and Buildings 2000; 32: 197-203.

[2] Asan H. Numerical computation of time lags and decrement factors for different building materials. Energy and Buildings 2006; 41: 615-620.

[3] del Coz Dı´az JJ, Garcı´a Nieto PJ, Betego´n Biempica C, Prendes Gero MB. Analysis and optimization of the heat-insulating light concrete hollow brick walls design by the finite element method. Applied Thermal Engineering 2007; 27: 1445-1456.

[4] del Coz Dı′az JJ, Garcı′a Nieto PJ, Sua′rez Sierra JL, Pen˜uelas Sa′nchez I. Non-linear thermal optimization and design improvement of a new internal light concrete multi-holed brick walls by FEM. Applied Thermal Engineering 2008; 28: 1090-1100.

[5] Bouchair A. Steady state theoretical model of fired clay hollow bricks for enhanced external wall thermal insulation. Building and Environment 2008; 43: 1603-1618.

[6] Li LP, Wu ZG, Li ZY, He YL, Tao WQ. Numerical thermal optimization of the configuration of multi-holed clay bricks used for constructing building walls by the finite volume method. International Journal of Heat and Mass Transfer 2008; 51: 3669-3682.

[7] Guo ZY, Zhu HY, Liang XG. Entransy-a physical quantity describing heat transfer ability. International Journal of Heat and Mass Transfer 2007; 50: 2545-2556.

[8] Chen Q, Zhu HY, Pan N, Guo ZY. An alternative criterion in heat transfer optimization. Proceedings of the Royal Society A-Mathematical Physical □Engineering Sciences 2011; 467: 1012-1028.

[9] Chen Q, Wang MR, Pan N, Guo ZY. Optimization principles for convective heat transfer. Energy 2009; 34: 1199-1206.

[10] Chen L, Chen Q, Li Z, Guo ZY. Optimization for a heat exchanger couple based on the minimum thermal resistance principle. International Journal of Heat and Mass Transfer 2009; 52: 4778-4784.

[11] Guo ZY, Liu XB, Tao WQ, Shah RK. Effectiveness–thermal resistance method for heat exchanger design and analysis. International Journal of Heat and Mass Transfer 2010; 53: 2877-2884.

[12] Shah RK, Skiepko T. Entropy generation extrema and their relationship with heat exchanger effectiveness–number of transfer unit behavior for complex flow arrangements. Journal of Heat Transfer; Transactions of the ASME 2004; 126: 994-1002.

[13] Wu J, Cheng XT. Generalized thermal resistance and its application to thermal radiation based on entransy theory. International Journal of Heat and Mass Transfer 2013; 58: 374-381.

[14] Chen Q, Yang KD, Wang MR, Pan N, Guo ZY. A new approach to analysis and optimization of evaporative cooling system I: Theory. Energy 2010; 35: 2448-2454.

[15] Chen Q, Pan N, Guo ZY. A new approach to analysis and optimization of evaporative cooling system II: Applications. Energy 2011; 36: 2890-2898.

[16] Zhang T, Liu XH, Zhang L, Jiang Y. Match properties of heat transfer and coupled heat and mass transfer processes in air-conditioning system. Energy Conversion and Management 2012; 59: 103-113.

[17] Chen L, Chen Q, Li Z, Guo ZY. Moisture transfer resistance method for liquid desiccant dehumidification analysis and optimization, Chinese Science Bulletin 2010; 55: 1445-1453.

[18] Xu YC, Chen Q. An entransy dissipation-based method for global optimization of district heating

 DOI: https://doi.org/10.30564/jbms.v3i2.3103

networks. Energy and Buildings 2012; 48: 50-60.

[19] Zhang Y, Chen Q, Zhang YP, Wang X. Exploring buildings' secrets: The ideal thermophysical properties of a building's wall for energy conservation. International Journal of Heat and Mass Transfer 2013; 65: 265-273.

[20] Zeng RL, Wang X, Di HF, Jiang F, Zhang YP. New concepts and approach for developing energy efficient buildings: ideal specific heat for building internal thermal mass. Energy and Buildings 2011; 43: 1081-1090.

[21] Zhang Y, Zhang YP, Wang X, Chen Q. Ideal thermal conductivity of a passive building wall: Determination method and understanding. Applied Energy 2013; 112: 967-974.

[22] ASHRAE. Handbook Fundamentals. SI Edition, Atlanta: American Society of Heating, Refrigerating and Air-Conditioning Engineers, 2009.

DOI: https://doi.org/10.30564/jbms.v3i2.3103

BILINGUAL PUBLISHING CO.
Pioneer of Global Academics Since 1984

Journal of Building Material Science
https://ojs.bilpublishing.com/index.php/jbms

ARTICLE

Effects of the Addition of Sawdust Ash and Iron Ore Tailings on the Characteristics of Clay Soil

Elinwa, Augustine Uchechukwu[1*] Mohammed, Abdulrahaman Shehu[2] Mohammed, Ahmed Bafeto[3]

1. Civil Engineering Department, Abubakar Tafawa Balewa University, Bauchi, Bauchi State, Nigeria
2. C/O Engineering and Construction Ltd, AY1 Faskari Road, sabo Gari, Tudun Wada, Kaduna, Kaduna State, Nigeria
3. Department of Civil Engineering, Federal Polytechnic Damaturu, Yobe State, Nigeria

ARTICLE INFO

Article history
Received: 18 September 2021
Accepted: 10 November 2021
Published Online: 20 December 2021

Keywords:
Additives
Firing temperature
Clay bricks
Bricks characteristics
Statistics
Regression models

ABSTRACT

An evaluation of the effects of additives and firing temperatures on clay bricks characteristics was studied. The two (2) additives used were sawdust ash (SDA) and iron ore tailing wastes (IOTW), and the five (5) firing temperatures of 400°C to 1200°C at intervals of 200°C were applied. The fired bricks were tested for linear shrinkage, water absorption, density, and compressive strength. The results of the investigations showed that firing temperature improved the clay brick characteristics across all replacement levels. However, the SDA additions increased the linear shrinkage and the water absorption but decreased the density and compressive strength. On the other hand, the addition of IOTW to the clay-SDA mixture, reduced both the linear shrinkage and water absorption of the clay bricks, and increased the density and compressive strength. The statistical values and the regression models derived on the experimental data using Minitab 18 Software were significant.

1. Introduction

The yardstick for the measurement of national progress is tied to the degree of contributions of the construction industry, and the building materials sector have been identified as the major contributor to the construction industry. Another area of concern in the construction industry is the rapid growth in construction works due to urbanization and the rate at which conventional materials for constructions are being depleted. These concerns are worsened by the pollution and degradation of the environments leading to depletion of the ozone layer and climate change.

The use of earth blocks and bricks dates back to thousands of years, and are man-made materials, made from the natural clay, and sundried. These were used for building houses by the low income groups. Burnt clay bricks are created from clay that are either molded, dry-pressed, or extruded and then dried and fired in a kiln. Researches on the improvement of clay bricks by addition and replacement materials have come of age because of the pressures on the conventional construction materials, and the advantages attached to the use of fired clay bricks. Fired bricks are inert materials which hardly react with

**Corresponding Author:*
Elinwa, Augustine Uchechukwu,
Civil Engineering Department, Abubakar Tafawa Balewa University, Bauchi, Bauchi State, Nigeria;
Email: auelinwa@gmail.com

 DOI: https://doi.org/10.30564/jbms.v3i2.3732

other materials, and do not release toxic substance.

Sutau et al [1] studied the "characteristics of fired clay bricks with waste marble powder addition as building materials." Using semi pressing process, they produced fired clay bricks lightened by the addition of up to 35% wt. % waste marble powder and analyzed by XRF, XRD, TGA, and SEM, respectively. The brick mixtures containing waste marble powder at different proportions were formed, dried and then fired at 950 and 1050°C for 2h. Some of their findings were that the use of waste marble powder addition reduced the bulk density of the samples, and the porosity ratios up to about 40% improved with increasing of waste marble powder additions up to 30 wt. % for all samples. However, they concluded that the compressive strengths decreased until 8.2 MPa but enough according to the values required by the standard.

Bagasse was added in proportions of 5 to 20 wt. % and fired to different temperatures of 700 to 1000°C to produce lightweight clay brick ceramic [2]. They concluded that higher bagasse additions resulted in higher values of porosity and water absorption. Also, reported were reductions in thermal conductivity and bulk density, but the increased firing temperature resulted in a decrease in porosity and water absorption, higher thermal conductivity and bulk density.

Aouba et al [3] in their work examined the significance of adding organic matter coming from agricultural solid waste (olive stone flour), OSF, and wheat straw, WS, residue to improve thermal performance while maintaining load bearing capacity. Some of their findings were that the bulk density decreased for mixtures containing OSF, ranging from 6% to 19% compared to clay alone, and for WS mixtures, where the bulk density reduced from 4% to 20%.

A study on the use of palm oil waste to produce fired clay bricks was undertaken by Kadir et al [4]. They incorporated palm waste in the proportions of 1%, 5%, and 10% by wt. % of clay, and fired to temperature of 1050°C with heating rate of 1°C/min. The results of their findings showed that the replacements with 1%, to 5% of POW improved several properties of the fired clay bricks with a decrease of performance at higher replacement levels (20% and 30%).

Srisuwan et al [5] used wood ash at replacement levels of 0, 4, 8, 12, and 16 % by wt. % of clay soil to prepare samples of clay bricks that were fired to temperatures of 900°C to 1100°C, at 100°C increment. The aim of their study was to evaluate the effect of the addition of wood ash and the firing temperature on the physical characteristics of the fired clay bricks. They concluded that the physical properties and strength of the fired clay bricks depend on the wood ash content and firing temperature.

The effect of adding sawdust ash (SDA) to clay for the purpose of making bricks was undertaken by Elinwa [6]. The bricks were fired to temperatures of 200°C, 600°C, and 1200°C and cured for 1, 4 and 8 days, respectively. They made measurements on linear shrinkage, water absorption, and compressive strength of fired bricks. His work concluded that the compressive strength decreased as the SDA was increased, and the maximum compressive strength was achieved at a firing temperature of 600°C, curing for 1 day, and at 10 % wt. %SDA. Equally of note in his conclusion was that the water absorption increased as the SDA was increased but the values were within the code specification.

The present work is on using two additives, SDA and IOTW, with clay soil and firing the brick samples at five different firing temperatures of 400°C, 600°C, 800°C, 1000°C, and 1200°C, respectively. The aim of the research work was to address the research needs raised by Elinwa [6] on the low compressive strength of fired clay bricks with SDA, by using a ternary material that can improve the low compressive strength. This problem was addressed by adding IOTW to the clay-SDA bricks using experimental methods.

Highlights

- Characterization of the materials- clay, sawdust ash and iron ore waste tailings.
- Experiments to determine the effects of sawdust ash and iron ore waste tailings on linear shrinkage, water absorption, density and compressive strength.
- Effects of firing temperatures and additives on these characteristics.
- Statistical and regression models on the experimental data.

2. Material

The materials used for this work are clay soil, sawdust ash (SDA), iron ore tailing wastes (IOTW), and potable water. The clay was sourced along Bauchi- Kano road in Bauchi State, Nigeria, and was oven dried for 24 hours, crushed using pestle and mortar, and sieved through 2.0 mm sieve. Table 1 shows the clay soil characteristics and the particle size distribution. Table 2 shows the improvements results on the clay soil using SDA matched with also the improvement that was carried out on the clay soil-SDA mixture, using IOTW. The replacements for the clay soil were 0%, 5%, 10%, 20%, 30%, and 40% by wt. % of clay soil. The MDD of 1.49 mg-m^3 and maximum dry density (OMC) of 25.6% for this composite were achieved. Using these values of MDD and OMC for the

DOI: https://doi.org/10.30564/jbms.v3i2.3732

clay-SDA mixture, three levels of improvement 10%, 20%, and 30% were chosen by replacing the clay soil-SDA mixture by IOTW by wt. %. The achieved lowest MDD was 1.44 mg-m^3 and OMC of 23.9 %.

Table 1. Characteristics of Clay Soil

Property	Average value (%)
Moisture Content (%)	
Liquid Limit (LL) (%)	12.2
Plastic Limit (PL) (%)	44.0
Plastic Index (PI) (%)	21.0
Linear Shrinkage (LS) (%)	23.0
Specific Gravity (SG)	12.2
Maximum Dry Density (MDD)	2.75
(mg-m^3)	1.65
Optimum Moisture Content	18.3
(OMC) (%)	
Particle Size Distribution	
Sand (%)	37.0
Silt (%)	38.4
Clay (%)	21.6
Gravel (%)	1.0

Table 2. Characteristics of Clay-SDA and Clay-SDA-IOT

Improvement Material	Mix No	MDD (mg-m^3)	OMC (%)
Sawdust ash (SDA)	MC-00	1.65	18.3
	MCS-05	1.65	19.8
	MCS-10	1.62	20.9
	MCS-20	1.59	24.0
	MCS-30	1.55	24.8
	MCS-40	1.49	25.6
Iron Ore Tailings (IOW)	MCS-10-I	1.44	23.9
	MCS-20-I	1.60	20.9
	MCS-30-I	1.64	19.7

The sawdust that was used for the production of the sawdust ash was from the Timber Market in Bauchi. This was processed using the Industrial Design Department kiln, Abubakar Tafawa Balewa University, Bauchi, Nigeria. The temperature range used for the calcination was between 400^{o}C and 600^{o}C and grinded using pestle and mortar and sieved through sieve 150 µm.

The iron ore tailing waste was obtained from Nigerian Iron Ore Mining Company (NIOMCO), Itakpe, Kogi State, Nigeria. The samples were crushed in a crushing machine and subsequently sieved through 212 µm sieve. The physical and chemical properties of both the clay soil, SDA and IOTW are shown in Table 3.

Table 3. Physical and Chemical Properties of SDA and IOT

Property	Value		
	Clay	SDA	IOTW
Specific Gravity	2.75	2.39	3.51
Moisture Content (%)	12.2	0.53	0.22
Bulk Density (kg/m^3)	-	1.21	1650
Fineness (m^2/g)	-	330	-
pH	-	10.0	13.11
Loss on Ignition (%)	-	0.45	-
Value (%)			
SiO_2	48.5	67.7	77.2
Al_2O_3	16.4	2.8	2.62
Fe_2O_3	4.1	1.53	15.0
CaO	0.5	0.1	1.20
Total ($Na_2O + K_2O$)	-	-	1.20
MgO	0.7	2.0	0.30
K_2O	1.4	0.53	-
Na_2O	-	0.60	-
SO_3	0.01	1.53	0.08
TiO_2	0.80	< 0.001	0.20
P	-	-	0.08
Other compounds and elements	0.23	-	8.37

3. Experiment

The productions of the bricks were in three phases. The first was the control samples, made with 100% clay soil. They are fifteen (15) in number. The second phase was done using clay soil to which proportions of SDA of 5%, 10%, 20%, 30% and 40% by wt. % of clay soil were mixed with the clay soil. These are labelled as MCS-00. MCS-05, MCS-10, MCS-20, MCS-30, and MCS-40 and a total of 75 samples were made. The third phase was an improvement on the clay soil-SDA using IOTW of 10%, 20%, 30% by weight of the clay soil-SDA composite. This was applied at the 40% SDA replacement where the minimum MDD and maximum OMC were achieved. A total of 45 brick samples were produced in this case. A total of 135 clay bricks samples were prepared and cured for seven days. In each of the phase, the amount of water required to give optimum compaction was determined from the compaction tests at various replacement levels. The machine used for the production of the bricks was the mechanically hand-operated block press Model CINVA-RAM, at the laboratory of Building Department, Abubakar Tafawa Balewa University, Bauchi, Nigeria. The machine was designed with dimensions 295 mm x 140 mm x 90 mm. The inner compartment of the CINVA-RAM contained fifteen (15) hollow chamfered metallic cube molds of dimensions 40 mm and driven into the soil to about half their depth and the cover placed over them.

 DOI: https://doi.org/10.30564/jbms.v3i2.3732

The whole assembly was pressed further until the whole depth of the mold penetrated the soil. The brick samples were compacted and extruded in this chamber. The extrusion of the samples were carried out using specially improvised extruder. The freshly extruded brick samples were placed on polythene leather giving enough spaces in-between for proper air circulation, and covered to prevent rapid or uneven curing. The curing was done for 7 days and oven dried at 50°C for 24 hrs to remove any moisture remaining in the sample. The purpose of curing is to allow the limestone ($CaCO_3$) convert to quicklime during firing to hydrate without expansion in the volume of the bricks [6]. The process of producing the brick samples is shown in Plate 1 (a-c).

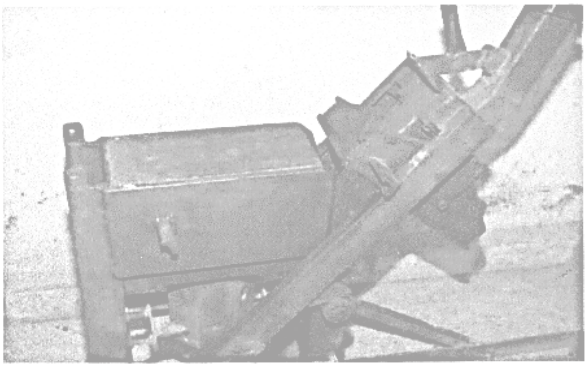

Compaction of the samples (a)

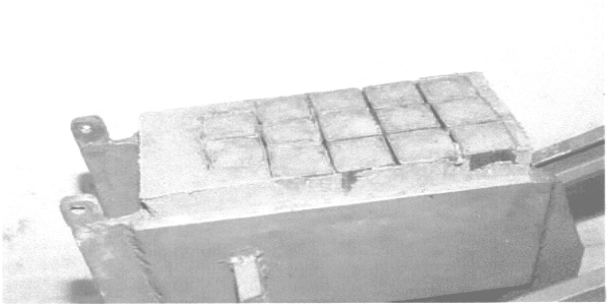

Extrusion of the samples (b)

Curing of the samples (c)

Plate 1. Compaction, Extrusion and Curing of the Samples

Firing of the Samples

The brick samples were subjected to five different temperatures of firing at 400°C, 600°C, 800°C, 1000°C, and 1200°C, in an electric oven, Model Alpha1, in the Faculty of Agriculture of the University. The heating velocity was kept approximately at 8°C and was capable of achieving 1200°C. To achieve uniformity in the heat flow in the furnace, the arrangement of the brick samples was such as to allow good spacing for proper circulation of heat. Heating of the brick samples was carried out at the stipulated temperatures, and at the attainment of each specified temperature, the brick samples were left in the chamber for approximately 2 hrs to attain a uniform temperature. They are then removed and cooled in air for 24 hrs. Three fired clay brick samples were tested for linear shrinkage, density, water absorption, and compressive strength. The average values are recorded as shown in Table 4.

Testing of the Fired Bricks

The linear shrinkage was tested at two stages; one after drying the bricks at 50°C for 2 hours. The parameter measured was the drying shrinkage. The second process was firing the brick samples at the temperatures of 400, 600, 800, 1000, and 1200°C, respectively. This was defined as the firing shrinkage. The linear shrinkage (total shrinkage) therefore, is the effect of both the drying and firing shrinkages, expressed as the percentage of the original length of the bricks This was done in accordance with ASTM C 210-95 [7]. The shrinkage was measured with the aid of digital vernier caliper readable to 01 mm. The linear shrinkage is the average of two sides of each brick and the average of three bricks were tested.

The density of the brick samples was first of all measured by weighing the bricks dry and dividing by the volume of each brick. After firing at each specified temperature, the volume of each brick was calculated by approximately taking the reduced lengths of the sides.

The water absorption of the fired brick is a measure of its porosity and carried out in accordance with ASTM C373-88 [8]. This was measured by immersion of the bricks in cold water for 24 hours and the water absorbed expressed as a percentage of its dry weight. Three (3) specimens were tested for each replacement level and temperature. The average of these values is recorded as the water absorption.

The compressive strength was carried out after testing for the water absorption, and allows to dry at 50°C for 24 hours. Three specimens were tested for each firing temperature using the Universal Testing Machine, Model TQ SM 100 of 100 kN capacity. The average results are recorded. The results of the linear shrinkage, water absorption, density and compressive strength are shown in Table 4.

DOI: https://doi.org/10.30564/jbms.v3i2.3732

Table 4. Results of SDA-IOT Brick

Property	Mix No	Temperature (°C)				
		400	600	800	1000	1200
Linear Shrinkage (%)	MC-00	6.2	6.5	7.1	7.7	8.3
	MCS-05	4.0	4.0	4.4	4.5	5.3
	MCS-10	3.0	3.7	4.2	4.5	5.0
	MCS-20	2.0	2.2	2.8	2.8	3.0
	MCS-30	1.3	1.9	2.3	2.8	2.9
	MCS-40	1.2	1.5	1.9	2.3	2.6
	MCS-10-I	3.3	3.9	4.0	4.1	4.1
	MCS-20-I	2.0	2.2	2.4	2.7	3.1
	MCS-30-I	1.6	1.9	2.1	2.6	2.7
Density (kg-m^3)	MC-00	2.17	2.12	2.05	2.02	2.00
	MCS-05	1.91	1.91	1.88	1.87	1.84
	MCS-10	1.83	1.79	1.77	1.76	1.71
	MCS-20	1.63	1.64	1.61	1.59	1.58
	MCS-30	1.63	1.60	1.58	1.57	1.54
	MCS-40	1.51	1.50	1.50	1.46	1.45
	MCS-10-I	1.98	1.97	1.95	1.95	1.89
	MCS-20-I	2.16	2.12	2.11	2.11	2.04
	MCS-30-I	2.32	2.32	2.29	2.29	2.27
Water Absorption (%)	MC-00	18.9	17.6	16.0	14.7	12.4
	MCS-05	19.2	18.6	18.5	17.9	14.8
	MCS-10	21.2	21.1	20.7	19.6	19.4
	MCS-20	27.4	26.7	26.6	26.5	23.3
	MCS-30	29.9	29.5	28.1	27.2	27.0
	MCS-40	35.8	33.7	33.5	30.6	27.3
	MCS-10-I	18.6	18.1	17.9	17.2	16.5
	MCS-20-I	16.3	15.9	15.4	14.9	13.1
	MCS-30-I	13.8	13.7	13.2	12.8	12.5
Compressive Strength (kN-m^2)	MC-00	4.5	5.9	7.5	8.2	5.8
	MCS-05	2.5	4.0	6.1	7.1	6.2
	MCS-10	1.8	3.5	3.7	3.8	3.9
	MCS-20	0.8	1.2	2.0	2.1	2.4
	MCS-30	0.6	0.6	1.0	1.0	0.6
	MCS-40	0.3	0.5	0.7	0.8	0.4
	MCS-10-I	2.8	5.0	6.1	6.7	7.4
	MCS-20-I	3.3	6.0	6.2	6.8	7.6
	MCS-30-I	3.4	6.1	6.3	7.5	8.5

4. Discussion

Characteristics of the clay soil

Figure 1a is on the Atterberg limit test. The values obtained showed that the clay belongs to the kaolinite group of clay minerals formed from the weathering of alkaline feldspar and alternate layers of silicon and aluminum. The plasticity index met the requirement of the standard (PI, 15 and 20). The specific gravity of the clay is 2.75. The grain size distribution from the composition of the clay indicated a gap graded soil with the composition shown in Figure 1b. This met the specification of the Standard for brick production [9].

The clay soil had a maximum dry density (MDD) of approximately 1.7 mg-m^{-3} with an optimum moisture content (OMC) of approximately 18%, obtained using the standard proctor compaction in accordance to BS 1377 Part 4 [10]. The lowest MDD and highest OMC for replacement levels of 5, 10, 20, 30, and 40 %, were achieved at 40 % wt. %SDA. These are 1.5 mg-m^3 and 25.6% for OMC. The lowest MDD and highest for the three levels of addition of IOTW (10, 20, and 30%), are 1.4 mg-m^3 and 23.9%. These are shown in Figure 2 (a and b). The various amounts of SiO_2 + Fe_2O_3 + Al_2O_3 for the clay soil, SDA and IOTW are approximately 69%, 72% and 90%, respectively, with a pH of 7, 10 and 13. The pH showed that the clay is little acidic while the SDA and IOTW are base in nature.

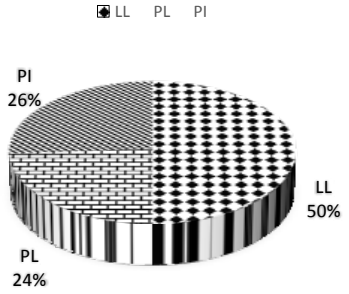

(a)- Atterberg Limit Test

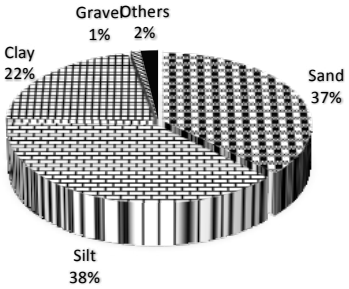

(b): Grain Size Distribution

Figure 1. Clay Soil Characteristics

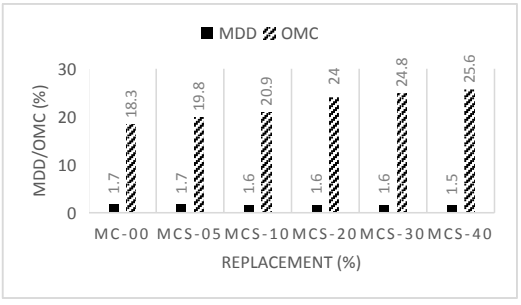

(a)- Clay-SDA

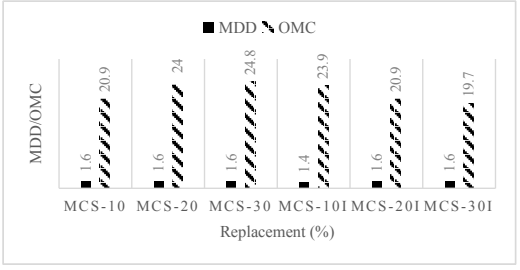

(b) – Clay-SDA-IOTW:

Figure 2. Maximum Dry Density and Optimum Moisture Content

 DOI: https://doi.org/10.30564/jbms.v3i2.3732

Properties of Fired SDA-IOTW Bricks

Linear Shrinkage

Firing temperatures affected the linear shrinkage of the clay bricks. Figure 3 showed that firing the clay bricks from 400°C to 1200°C achieved a shrinkage of approximately 6 to 8%. This could also be said for SDA replacements of 5, 10, 20, 30 and 40% by wt. % of clay, where reductions of 4-5%, 3-5%, 2-3%, 1.3-2.9%, 1.2-2.6%, respectively, were recorded. This strongly showed that firing temperatures affected to a great extent the linear shrinkage, and the best firing temperature was at 1200°C [3]. It has been reported in the literature that shrinkage occurred when the chemically and mechanically bound water evaporated [5]. This assertion can be said to be observed on the results obtained. It seemed that the addition of SDA which is pozzolanic in nature, achieved internal transformations necessary for structural changes and solidifications [5]. The addition of IOTW to the clay-SDA bricks was at three levels of 10%, 20% and 30%. The aim was to observe its effect on the clay-SDA bricks. The IOTW contained 90% the total sum of SiO_2 + Al_2O_3 + Fe_2O_3 with Fe_2O_3 approximately 15%. IOTW. Therefore it is a ferric oxide silicate material. This, as observed equally had some transformational effects on the stability of the clay-SDA-IOTW bricks. Therefore, the additions of SDA and IOTW to fired clay bricks affected the linear shrinkage (LS) [3,5].

Water Absorption

From Figure 4, the effect of firing temperatures for all classes of clay brick mixture showed reductions in water absorption as the firing temperatures increased (400-1200°C). Water absorption is a durability indicator and gives information about open porosity [3]. Therefore, firing temperatures of bricks have tremendous effects on the bricks. The higher the firing temperatures the lesser is the water absorption. For 100% clay samples (control) fired for the range of temperatures of 400-1200°C, the water absorption decreased from 18.9-12.4%. However, with the addition of SDA by wt. % of clay, the water absorptions are 19.2-14.8%, 21.2-19.4%, 27.4-23.3%, 29.9-27.0%, and 35.8-27.3%, for the same range of temperatures, 400-1200°C, respectively. This showed reduction with the firing temperature increased. It was equally observed that as the replacement with SDA increased the water absorption increased. This was clearly the case when a comparison of the clay bricks containing SDA are made with the control clay bricks (without SDA).The differences in the water absorption increased respectively from 1.6-19.4%, 12.2-54.5%, 35.0-87.9%, 58.2-117.7%, and 89.4-120.2%, with the firing temperatures of 400°C to 1200°C.Therefore, the effect of adding SDA to clay soil and firing can be said to increase the water absorption as the quantity of SDA was increased. This was also confirmed by the study of Srisuwan et al [5] and Elinwa [6], which stated that higher wood ash and SDA content affected an increase in porosity and water absorption. The addition of IOTW at three levels of 10%, 20% and 30% clay-SDA by wt. %, and compared with the same levels of addition in clay-SDA, showed immense improvement on the water absorption. The percentage water absorption reductions were therefore calculated as shown in Equation (1):

$$WA_R = \frac{(WA_{T_{CS}} - WA_{T_{CSI}})}{WA_{T_{CS}}} \; x \; 100\ \% \qquad (1)$$

Where

WA_R = % water absorption reduction

$WA_{T\,CS}$ = Water absorption of clay-SDA at the indicated firing temperature (%)

$WA_{T\,CSI}$ = Water absorption of clay-SDA-IOTW at the indicated temperature (%)

Example:

At 10 % replacement @ 400°C

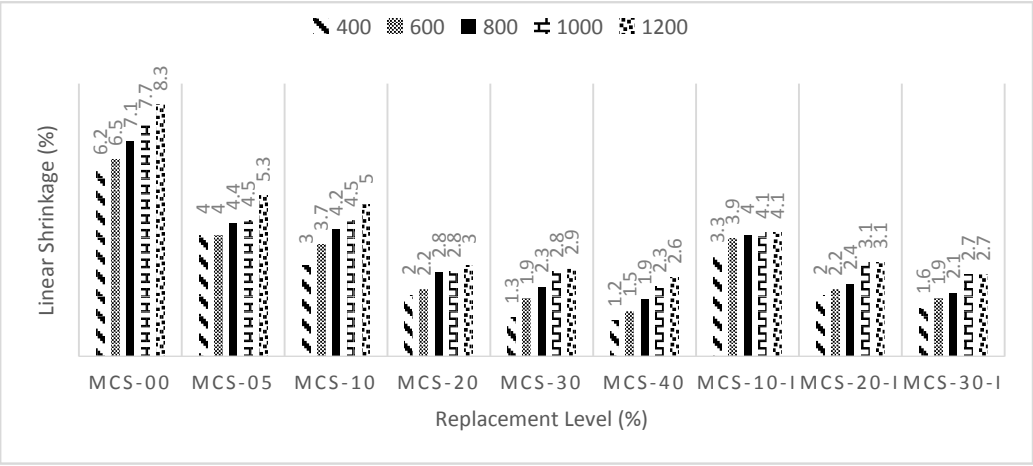

Figure 3. Linear Shrinkage (%)

DOI: https://doi.org/10.30564/jbms.v3i2.3732

$WA_{T\,CS}$ = *21.2 %*

$WA_{T\,CSI}$ = *18.6 %*

$WA_R = \frac{18.6 - 21.2}{21.2}$ *x 100 % = -12 %: The same is done for other firing temperatures.*

The reductions were approximately -12-15%, -42-44%, and -54-54%. The interpretation of which signified porosities of 25%, 7%, and 0%, respectively. The 0% porosity is a closed porosity. Therefore, addition of IOTW to clay bricks would improve the durability of the bricks.

The Density of the Bricks

Figure 5 showed the fired densities of the clay-SDA bricks and the three levels of clay-SDA-IOTW bricks. The bulk densities at the various firing temperatures were 2.17-2.0%, 1.91-1.84%, 1.83-1.71%, 1.63-1.54%, and 1.51-1.45%, for clay-SDA bricks at 0% to 40% of SDA by wt. % of clay. The clay-SDA brick densities decreased as the firing temperatures increased. The percentage decrease in the densities at firing temperatures of 600-1200°C compared to the firing temperature of 400°C were 12 %, 16 %, 25%, and 30%, respectively. The same observation was made by Srisuwan [5]. Some factors have been attributed to this behavior. These are due to increased consolidation or vitrification between the particles in the body as the firing temperature increased. The lower bulk densities of the samples with the SDA additives are presumed to be as a result of the lower densities of the SDA. Similar observation was made by Chopra S, as referenced in the works of Arthur and Gikunoo [11], and Srisuwan et al [5], respectively. The clay-SDA-IOTW bricks at three levels of IOTW additions ranged from 1.98-1.89 mg-m^3, 2.16-2.04 mg-m^3, 2.32-2.27 mg-m^3. This showed that the clay-SDA-IOTW increased at the three levels of IOTW additions. We can therefore conclude that the IOTW contributed to the high densities recorded as a result of the high density of IOTW material. The differences in increase of the densities attained at 600-1200°C compared with the 400°C firing temperature were 8% to 28%.

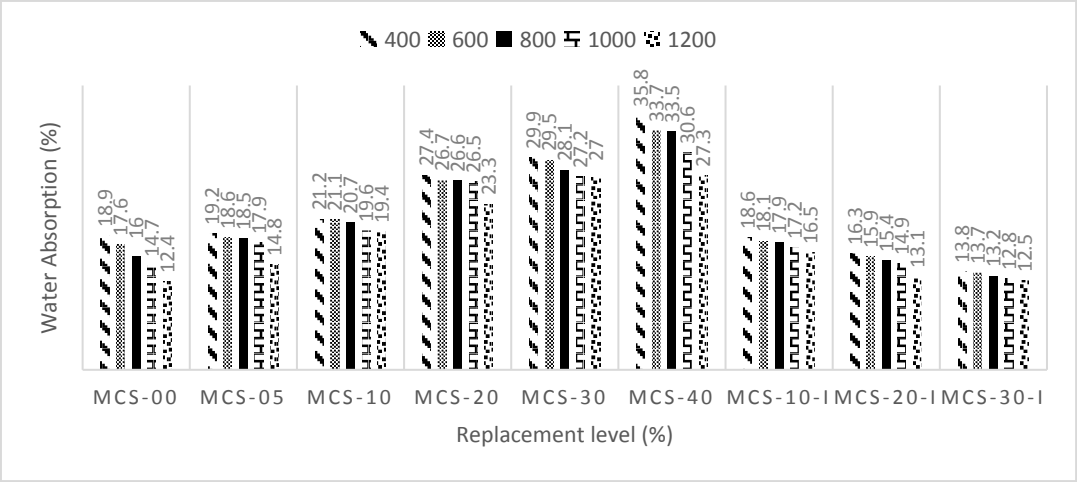

Figure 4. Water Absorption (%)

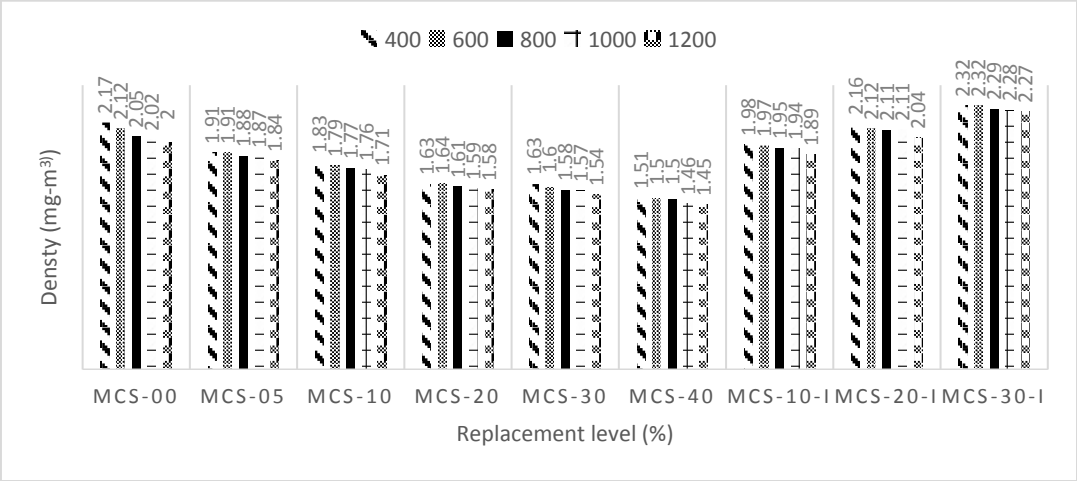

Figure 5. Density (mg-m^3)

 DOI: https://doi.org/10.30564/jbms.v3i2.3732

Compressive Strength

The compressive strength of clay-SDA and clay-SDA-IOTW, fired bricks are shown in Figure 6. Observations showed that at firing temperatures of 800°C and 1000°C, the 100% clay mixture (Control), gave the highest compressive strengths of 7.5 kN-m^2 and 8.2 kN-m^2, respectively. The mixture containing SDA, only the fired bricks with replacement of 5% SDA gave a strength of 7.1 kN-m^2 at 1000°C firing temperature. The same observation was made by Janbuala and Wasanapiarngong [2], using bagasse to produce lightweight clay bricks, and Srisuwan et al, [5], using wood ash. Other replacement levels and firing temperatures recorded low compressive strengths [3]. This has also been attributed to the low content of Al_2O_3 and mullites in SDA [6]. The three levels of additions of IOTW showed remarkable strength improvement over the clay-SDA fired bricks. The optimum compressive strength for each of the mix was at 1200°C and are given as 7.4 kN-m^2, 7.6 kN-m^2, and 8.5 kN-m^2, respectively.

Basic statistics and sensitivity on data on the fired bricks

The aim of this exercise was to evaluate and validate the credibility of the data collected on the experiments. For variations to be properly accounted for, sufficient number of tests were required. This was important because it will form the basis for determining from such results the potential quality and strength of the data, and for expressing results in the most useful form. Statistical procedures provide a sound basis for determining from such results the potential quality and strength of our experimental data, and for expressing results in the most useful form. The basic characteristics of the fired brick data will assist in understanding better the interactions of the various materials used for the production of the bricks. Table 5 showed in details the degrees of the performances and interactions of the fired bricks carried out using the Minitab 18 Software. Measurements were made on the mean, standard error of the mean (SE.Mean), standard deviation (St.Dev) and coefficient of variation (Coef. Var), on the linear shrinkage, water absorption, density and compressive strength of the fired bricks.

The mean value characterizes the central tendency or location of the data, while the coefficient of variation provides a general feeling about the performance of the method and its distribution around the mean. This expresses the variation as a percentage of the mean. Thus, the larger the coefficient of variation is, the greater the spread in the data. The standard error of the mean (SE Mean) estimates the variability between sample means, and the standard deviation and thus, establishes a benchmark for estimating the overall variation of a process. Whereas, the standard error of the mean estimates the variability between samples, the standard deviation measures the variability within a single sample. The variance (standard deviation squared) measures how spread-out the data are about their mean. A higher standard deviation value indicates greater spread in the data. The greater the variance is the greater the spread in the data. Figures 7 showed the diagrammatical presentation of these statistics. The values achieved showed good performance of the fired clay-SDA and Clay-SDA-IOTW bricks. Table 6 showed the strength of the relationships between the various parameters studied. (Linear shrinkage, water absorption, density, and compressive strength). They showed high correlation values (r^2: > 86 %), signifying strong relationship between the firing temperatures and clay composites. They are equally significant with p-value < 0.05. Therefore, it can be concluded that the additives used and firing temperatures on clay bricks were the major influence in the production of bricks, and they affected the final product. Cultrone et al [12] held the same view.

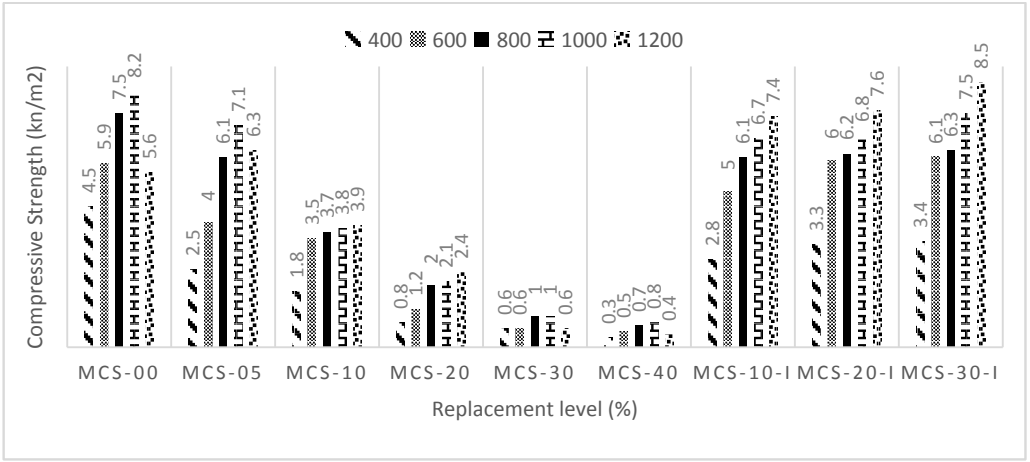

Figure 6. Compressive Strength (kN-m^2)

DOI: https://doi.org/10.30564/jbms.v3i2.3732

Table 5. Basic Statistics of SDA Ash-Lateritic Bricks

Property	Temp (oC)	Mean	SE Mean	StDev	Variance	CoefVar
Linear Shrinkage (%)	400	2.73	0.5	1.6	2.6	59.0
	600	3.1	0.5	1.6	2.6	51.7
	800	3.5	0.6	1.7	2.8	48.0
	1000	3.8	0.6	1.7	2.8	43.5
	1200	4.1	0.6	1.9	3.5	45.3
Water Absorption (%)	400	22.3	2.4	7.2	51.3	32.1
	600	21.7	2.3	6.8	45.9	31.3
	800	21.1	2.3	6.8	46.4	32.3
	1000	20.2	2.1	6.4	40.6	31.6
	1200	18.5	2.0	6.1	36.7	32.8
Density (mg-m^3}	400	1.9	0.1	0.3	0.1	14.69
	600	1.9	0.1	0.3	0.1	14.60
	800	1.9	0.1	0.3	0.1	14.36
	1000	1.8	0.1	0.3	0.1	14.80
	1200	1.8	0.1	0.3	0.1	14.76
Compressive Strength (kN-m^2)	400	2.2	0.5	1.4	2.1	65.0
	600	3.6	0.9	2.3	5.5	64.2
	800	4.4	0.9	2.6	6.7	58.9
	1000	4.9	1.0	3.0	8.8	60.7
	1200	4.7	1.0	3.0	9.3	64.4

Table 6. Correlation and P-Values of Sawdust Ash Lateritic Bricks

Property	**Temp (oC)**	**400**	**600**	**800**	**1000**
Linear Shrinkage (%)	600	0.990 (0.000)			
	800	0.987 (0.000)	0.995 (0.000)		
	1000	0.977 (0.000)	0.986 (0.000)	0.988 (0.000)	
	1200	0.977 (0.000)	0.979 (0.000)	0.988 (0.000)	0.992 (0.000)
Water Absorption (%)	600	0.997 (0.000)			
	800	0.994 (0.000)	0.997 (0.000)		
	1000	0.981 (0.000)	0.990 (0.000)	0.995 (0.000)	
	1200	0.951 (0.000)	0.970 (0.000)	0.969 (0.000)	0.978 (0.000)
Density (mg-m3)	600	0.997 (0.000)			
	800	0.994 (0.000)	0.998 (0.000)		
	1000	0.992 (0.000)	0.996 (0.000)	0.999 (0.000)	
	1200	0.990 (0.000)	0.997 (0.000)	0.998 (0.000)	0.997 (0.000)
Compressive Strength (kN-m2)	600	0.961 (0.000)			
	800	0.970 (0.000)	0.964 (0.000)		
	1000	0.961 (0.000)	0.960 (0.000)	0.997 (0.000)	
	1200	0.855 (0.000)	0.947 (0.000)	0.923 (0.000)	0.933 (0.000)

 DOI: https://doi.org/10.30564/jbms.v3i2.3732

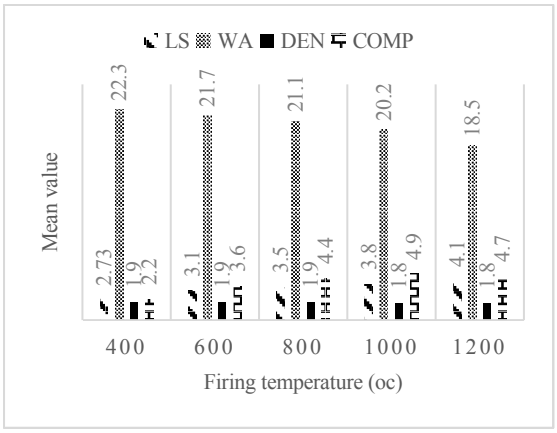

Mean

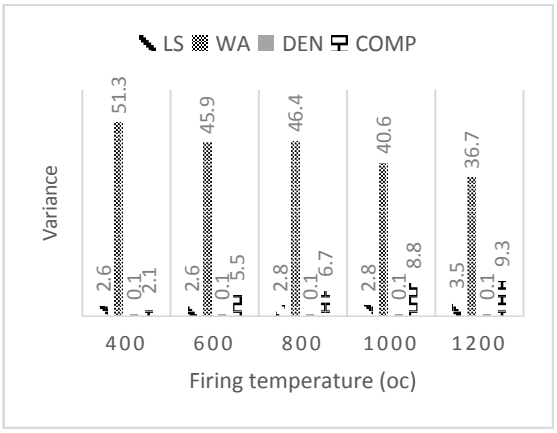

Variance

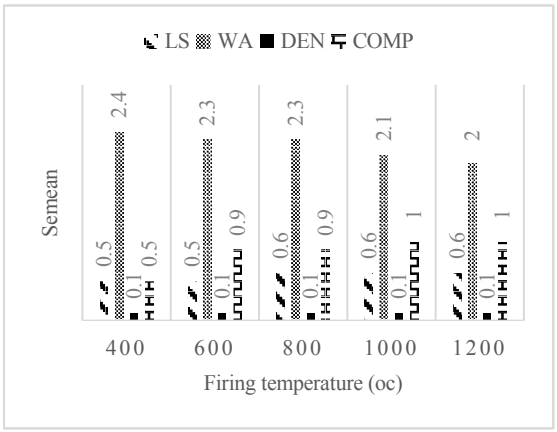

Standard Mean Error

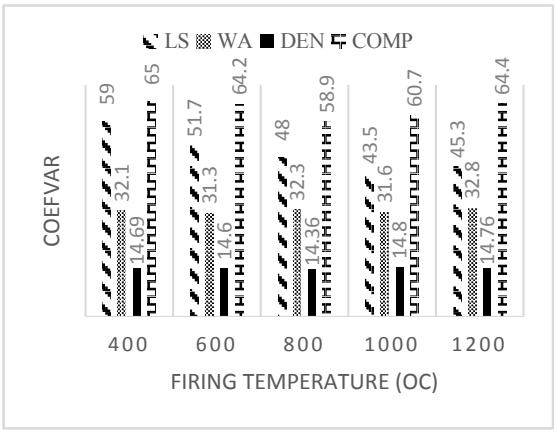

Coefficient of Variation

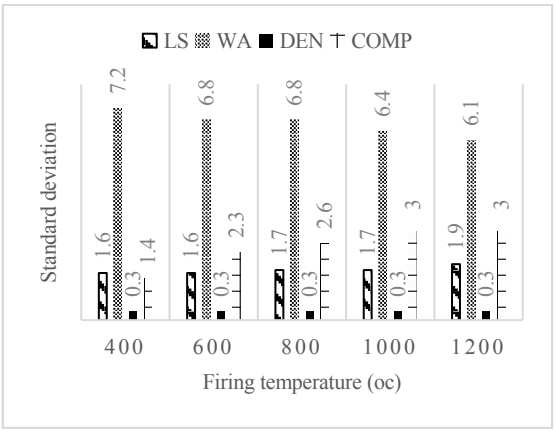

Standard Deviation

Figure 7. Basic Statistical Indicators of Fired Bricks

Linear Regression Model of the Clay-SDA Fired Bricks

Linear regression analysis was performed on the experimental data collected on the clay-SDA fired brick samples. The table of values is shown in Table 7. The normality and residual plots are shown in Figure 8. The regression models are significant with p-values < 0.005. The constant and mix are equally significant. However, the p-value for the Temp are greater than 0.005 for the water absorption and density, respectively. These values (water absorption and density) do not invalidate the significance of the regression models but may indicate that the evidence is not strong enough to suggest an effect exists.

DOI: https://doi.org/10.30564/jbms.v3i2.3732

Table 7. Regression Model Data

Property	Transformation	Equation			Characteristic		Static		
		Const	Mix	Temp	S	R^2	Var	*p*-value	Signif
WA	Box-Cox Rounded λ = 0.25 Estimated λ = 0.25 95 % CI for λ = (0.10, 0.40)	+9.96	+3.90	-0.07	2.0265	91.97	Const Mix Temp RegModel	0.000 0.000 0.838 0.000	Signif Signif NSignif Signif
Density	None	+2.13	-0.11	-0.001	0.0677	89.11	Const Mix Temp RegModel	0.000 0.000 0.894 0.000	Signif Signif NSignif Signif
(Comp)^2	None	+1.85	-0.16	-0.04	0.1306	82.70	Const Mix Temp RegModel	0.000 0.000 0.041 0.000	Signif Signif Signif Signif

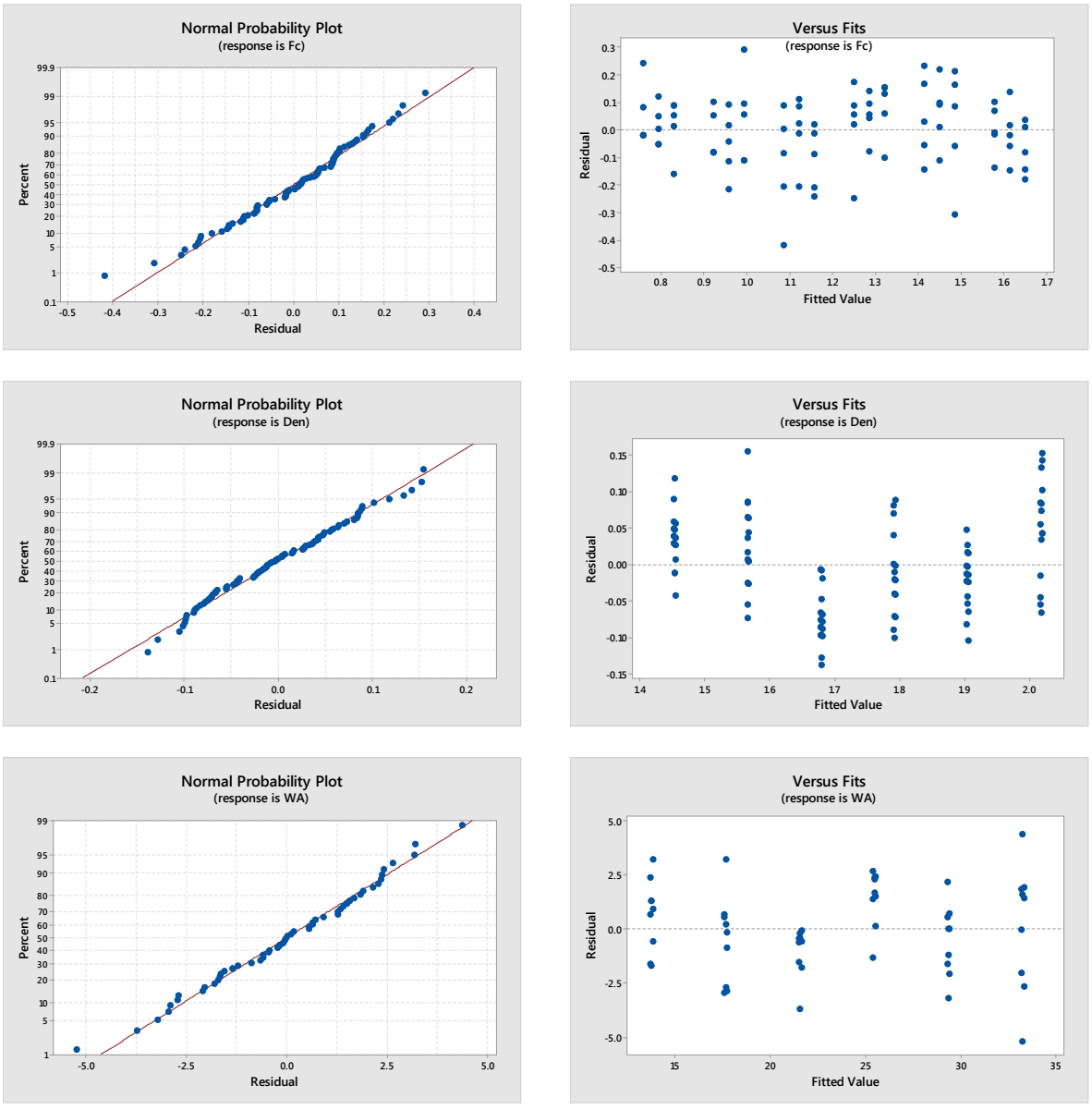

Figure 8. Normality and Residual Plots of the Regression Models

 DOI: https://doi.org/10.30564/jbms.v3i2.3732

5. Conclusions

This work addresses the changes in properties of clay-based bricks upon the addition of two waste materials, namely a sawdust ash (SDA) and iron ore tailing wastes (IOTW). It is advocated in this research that such practice would bring benefits to both the waste producers and the ceramic industries. An evaluation and effect, on the use of additives (SDA and IOTW), and the firing temperatures, have been carried out on clay samples, using experimental data, to ascertain the levels of their effectiveness in fired clay bricks. The followings are the conclusions derived from the work.

1) The linear shrinkage increased as the firing temperatures increased for all types of clay bricks considered. However, the additions of SDA and IOTW had different level of effects on the fired clay bricks. The linear shrinkage was reduced by their inclusion but better performance was recorded for the fire brick samples containing IOTW.

2) The water absorption, a property of durability was reduced for all types of clay bricks as the firing temperature was increased. The addition of SDA recorded higher values of water absorption than the control bricks, signifying not a suitable material when water absorption is considered. However, the values obtained when IOTW was added showed that the defects in using SDA can be remedied using IOTW.

3) The density of the clay bricks is affected by the firing temperatures across all types of clay bricks and more pronounced with the addition of SDA. From the data obtained, addition of SDA and firing to different temperature will produce lightweight bricks. These defects again are corrected using IOTW.

4) The compressive strength increased both with firing temperatures and percentage replacements for all the types of clay bricks considered. The optimum firing temperature for the control samples was 1000^{o}C. The same firing temperature was attained for 5 % wt. % SDA. A much reduced strengths was recorded for other replacements. Therefore, the use of SDA will not improve the compressive strength of fired clay bricks. However, the inclusion of IOTW markedly improved the compressive strength. The best firing temperature was 1200^{o}C at all the three additions. The sensitivity analysis and regression models showed that the use of SDA and IOTW for clay bricks will produce good fired bricks judging from the data collected on the experimental works.

References

[1] M Sutau, H Alptckin, E Erdogmus, Y Er, O Gencel (2015). "Characteristics of fired clay bricks with waste marble power addition as building materials," Construction and Building Materials, 82, 1-8.

[2] S Janbuala and T Wasanapiarnpong (2016). "Light-weight clay brick ceramic prepared with bagasse addition." ARPN Journal of Engineering and Applied Sciences, 11 (13), 8380-8384.

[3] Aouba, Laila and Bories, Cécile and Coutand, Marie and Perrin, Bernard and Lemercier, Hervé *Properties of fired clay bricks with incorporated biomasses: Cases of Olive Stone Flour and Wheat Straw residues.* (2016) Construction and Building Materials, 102 (Part. 1). 7-13. ISSN 0950-0618.

[4] AA Kadir, NA Sarani, MMAB Abdullahi, MC Perju, AV Sandu (2017). "Study on fired clay bricks by replacing clay with palm oil waste: Effects on physical and mechanical properties," International Conference on Innovative Research – ICIR EUROINVENT IOP Conf. Series: Materials Science and Engineering 209, 012037.
DOI: 10.1088/1757 – 899x/209/1/01 037.

[5] Srisuwan A, Sompech S, Saengthong C, Thaomola S, Chindraprasirt P, and Phonphuak N (2020). "Preparation and properties of fired clay bricks with added wood ash." Journal of Metals, Materials and Minerals, 30, (4), 84-89.

[6] Elinwa AU (2006). "Effect of addition of sawdust ash to clay bricks." Civil Engineering and Environment Systems, 23 (4), 263-270.

[7] ASTM C210-95 (2019). Standard Test Method for Reheat Change of Insulating Firebrick.

[8] ASTM C 373-88 (2006). Standard Test Method for Water Absorption, Bulk Density, Apparent Porosity, and Apparent Specific Gravity of Fired Whiteware Products.

[9] ASTM C216-19 (2019). Standard Specification for Building Brick (Solid Masonry Units Made from Clay or Shale).

[10] BS 1377-4:1990. Methods of Test for Soils for Civil Engineering Purposes. Compaction-Related Tests – BSI British Standards.

[11] E. K. Arthur & E. Gikunoo | (2020) Property analysis of thermal insulating materials made from Ghanaian anthill clay deposits. Cogent Engineering, 7:1, 1827493.
DOI: 10.1080/23311916.2020.1827493.

[12] G Cultrone, E Sebastian, MJ de la Torre (2005). "Mineralogy and physical behavior of solid bricks with additives." Construction and Building Materials, 19, 39-48.

DOI: https://doi.org/10.30564/jbms.v3i2.3732

BILINGUAL PUBLISHING CO.
Pioneer of Global Academics Since 1984

Journal of Building Material Science
https://ojs.bilpublishing.com/index.php/jbms

ARTICLE

Physio-Chemical Characteristics and Acid-Sulphate Reactions of Moringa Oleifera Seed Powder Cement Paste and Concrete

Augustine Uchechukwu Elinwa[1*] Isaac Bulus Ayuba[2] Sagir Samaila Danjauro[2]

1. Civil Engineering Department, Abubakar Tafawa University, Bauchi, Bauchi State, Nigeria
2. Civil Engineering Department, Abubakar Tafawa Balewa University, Bauchi State, Nigeria

ARTICLE INFO

Article history
Received: 19 September 2021
Accepted: 5 November 2021
Published Online: 10 December 2021

Keywords:
Moringa oleifera seed powder
X-ray diffraction analysis
Mechanical strengths
Acid-sulphate media
Microstructure

ABSTRACT

The evaluation of the effect of using moringa oleifera seed powder (MOSP) to partially replace cement by wt. % has been carried out. A mix parameter of 1: 1.7: 2.5, with designed strength of 20 kN-m^2, and a cement content of 420 kg-m^3, water-cementitious ratio of 0.5, to produce concrete specimens to which percentages of MOSP by wt. % of cement were added and cured for 90 days. Basic characteristics of the MOSP material were determined (Consistency and Setting times), and the concrete parameters workability, density, water absorption and compressive strength were also determined. The analysis of the experimental data collected on MOSP and MOSP-concrete confirmed that MOSP is substantially silicate (Quartz and Cristobalite). These have greatly to a large extent imparted on the quality of MOSP-concrete produced good quality concrete. The optimum replacement was at 0.2 % wt. % of cement.

1. Introduction

The construction industry is evolving, and the need to address demands for constructed facilities are increasing and becoming more complex with the dwindling conventional materials, and climate change. Cost and safety have been the underlying thrust in the construction industry, and therefore, the need for improved Research and Development (R & D) becomes very imperative. The importance of admixtures and additives in the concrete industry is gaining wide recognition because of proven advantages in ease of concreting, strength gains and durability issues. Water-reducing additives such as superplasticizers make it possible to achieve good workability of fresh concrete and correspondingly a dense concrete microstructure in the hardened state [1].

Recent advances in researches on new chemical additives have arisen because of the great advances in concrete technology. These new chemical additives, applied in small quantities can drastically improve crucial properties of concrete in its fresh and/hardened state [1]. Moringa oleifera seeds and leaves have been used extensively for water treatment, and in the health sector. They have not been researched upon for possible use as additives in the construction industry. To this extent, not much is said about the use of Moringa oleifera for concrete production in the literature. Therefore, it becomes imperative to carry such research works on Moringa oleifera for possible application in the construction industry. These research works will help determine the advantages and disadvantages in the use of the material. The introduction of Moringa oleifera seed powder as a

**Corresponding Author:*
Augustine Uchechukwu Elinwa,
Civil Engineering Department, Abubakar Tafawa University, Bauchi, Bauchi State, Nigeria;
Email: auelinwa@gmail.com/08065040376

 DOI: https://doi.org/10.30564/jbms.v3i2.3735

new component for concrete production makes available a number of new possibilities with respect to additive materials for concrete production. This will improve workability and the reheological properties of the fresh concrete.

A preliminary work on Moringa oleifera seed powder was undertaken by Susilorini et al [2]. They worked on the "compressive strength optimization of natural polymer modified mortar with Moringa oleifera in various curing media" using a mortar mix of 1: 1: 0.6, that is, cement, sand and water, with moringa oleifera seed powder dosage of 0, 0.1, 0.2, 0.5, 1, 2, and 5 % by wt. % of cement. Mortar cubes of 50 mm dimensions were made and cured for 7 days, 14 days, and 28 days, before testing to failure. The results of their study showed that the use of moringa oleifera seed powder improved the quality of the concrete, and the optimum dosage that gave the highest compressive strength was at 0.2 %.

A conference proceeding paper on the improved work on moringa oleifera seed powder and husk was carried out by Susilorini et al [3]. They made several concrete cylinder specimens of natural polymer modified concrete with dimensions 10 cm x 20 cm for a concrete design strength of 30 MPa and cured for 7, 14, and 28 days, using a moringa oleifera dosage of 0.2 wt. %. The results also showed that using the powder and husk improved the concrete strength.

The present work arose because of the very little knowledge of the spectrum of moringa oleifera seed powder applications as additives in concrete production. Equally of concern was the fact that Susilorini et al works were not in depth [2,3]. In the present study experiments are mounted to characterize the behavioral pattern of the moringa oleifera seed powder in cement paste and concrete. The basic characteristics of the material (water affinity and setting times) are established, and the effects of the hydration process on the physical, chemical, and morphological composition of MOSP on concrete characteristics such as workability, density, water absorption and compressive strength are evaluated. The work also assessed the behavior of this material in concrete, in acid and sulphate environments.

2. Materials

The materials used for this research are grade 43 'Ashaka' Portland cement, fine aggregate (river sand), coarse aggregate, Moringa oleifera seed powder (MOSP) and potable drinking water. The physical and chemical properties of the cement are shown in Table 1, while, the physical properties and sieve analysis of the fine and coarse aggregates are shown in Tables 2 and 3. Both the cement and aggregates conform to BS EN 196-1 [4] for testing cement, and BS EN 12620 [5] and BS 812-2 [6] for the testing of aggregates. The size of the coarse aggregate was 20 mm and both the fine and coarse aggregates were of zone 2 in the grading system.

Table 1. Physical and Chemical Properties of Cement

Physical Properties of Cement	
Specific Gravity	3.15
Lose Bulk Density (kg-m^3)	3150
Fineness Modulus	<10
Chemical Properties	
Oxide	Percentage by weight (%)
CaO	63.7
SiO_2	19.90
Al_2O_3	5.60
Fe_2O_3	2.90
MgO	1.50
Na_2O and K_2O	0.92
SO_3	2.30

Table 2. Physical Properties and Sieve Analysis of the Fine Aggregate

Physical Properties of the Fine Aggregate		
Test type		Results
Specific Gravity		2.32
Moisture Content (%)		1.18
Bulk Density (kg/m^3)		1611.32
Particle Size Distribution		
BS Sieve	Mass Retained (%)	% Passing
5 mm	-	
3.35 mm	0	100
2 mm	42.2	91.76
1.18 mm	60.9	79.58
600 µm	230	33.59
425 µm	87.7	16.06
300 µm	29.7	10.12
212	32.9	3.54
150	12.9	0.96
75	3.5	0.26
Pan	1.3	0.00
Total	500	

The Moringa Oleifera seed used for this work was sourced from the local markets in Bauchi State, Nigeria. Bauchi State is in the Sahel region of the Northern part of Nigeria, and characterized by extreme weathers. The seeds were grinded and sieved using sieve size 212 µm to obtain the desired fineness. The physical characteristics of the powder had a moisture content of 8.33%, bulk density, 8.42 g-cm^3, and a specific gravity of 0.28. The chemical compositions of the MOSP were determined by X-ray fluorescence (XRF) according to NF P15-467 [7], and the results are shown in Table 4. Figure 1 shows the x-ray diffraction of the MOSP.

DOI: https://doi.org/10.30564/jbms.v3i2.3735

Table 3. Physical Properties and Sieve Analysis of Coarse Aggregates

Physical Properties of the Coarse Aggregate		
Test type		Results
Specific Gravity		2.74
Moisture Content (%)		0.15
Bulk Density (kg/m^3)		1611.32
Aggregate Impact Value (AIV)		12.85
Aggregate Crushing Value (ACV)		26.85
Particle Size Distribution		
BS Sieve (mm)	Mass Retained (%)	% Passing
37.5	-	
28	0	100.00
20	364.3	87.86
14	2159.2	15.89
10	390.8	2.86
6.3	75.1	0.36
5	9.5	0.04
3.35	1.1	0.00
Pan	0.1	0.00
Total	3000	

Table 4. Oxide composition of Moringa seed

Oxide	Percentage by weight
SO_3	28.3
P_2O_5	8.2
CaO	7.8
K_2O	7.5
SiO_2	5.8
MgO	2.1
Nb_2O_5	0.03
ZnO	2.0
Na_2O	1.4
TiO_2	0.1
MnO	0.5
Al_2O_3	6.2
NiO	3.8
Cr_2O_3	3.1
Fe_2O_3	17.6
Ag_2O	0.03

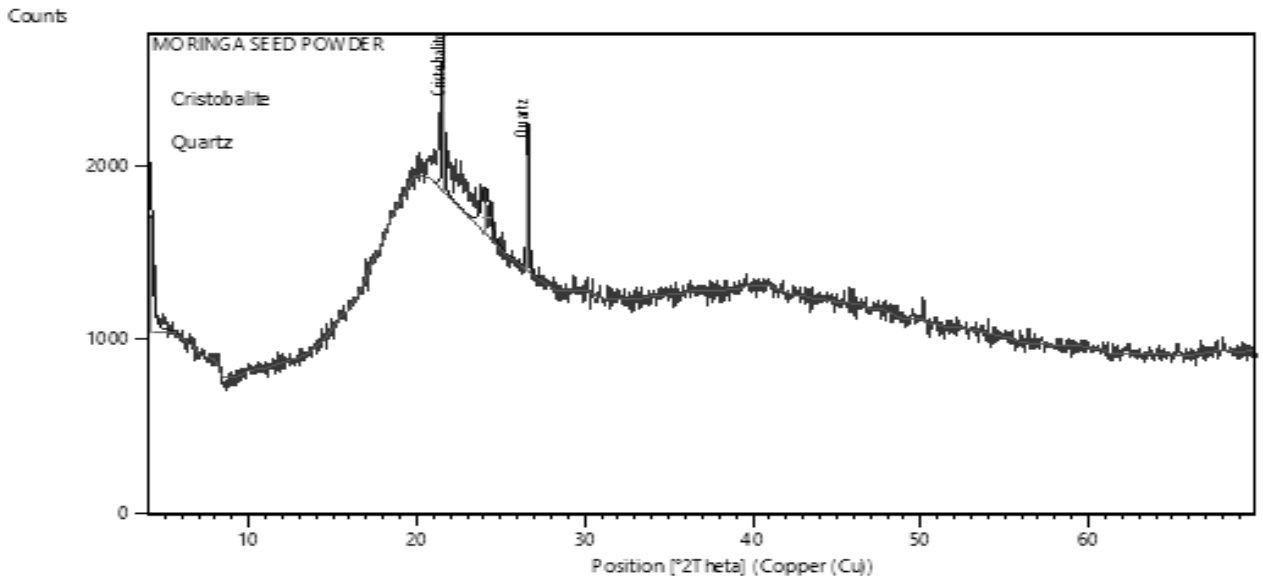

Pos.[°2Th.]	Height [cts]	FWHMLeft	[°2Th.] d-spacing [Å]	Rel. Int. [%]
4.1191	650.54	0.3070	21.45196	92.21
21.5700	705.51	0.1279	4.11992	100.00
24.1064	182.77	0.6140	3.69188	25.91
26.6326	673.4	0.1279	3.34714	95.45

Pattern List

Visible	Ref.Code	Score	Compound Name	Displ.[°2Th]	Scale Fac.	Chem. Formula
*	96-900-8233	35	Cristobalite	0.000	0.624	Si8.00 O16.00
*	96-900-9667	23	Quartz	0.000	0.819	Si3.00 O6.00

Figure 1. Details on the Moringa Oleifera Seed Powder

 DOI: https://doi.org/10.30564/jbms.v3i2.3735

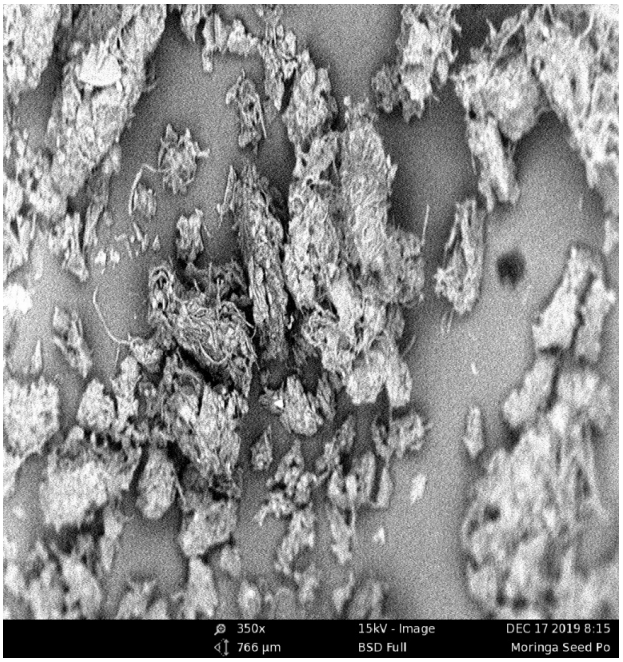

Figure 2. Microstructure of MOSP

3. Experiment

The experiments carried out were on the paste and concrete samples made using moringa oleifera seed powder in various proportions of 0.1% to 5.0% by wt. % to replace cement. The MOSP-paste tests were on the consistency and setting times of the paste. These were tested in accordance with BS EN 196-3 [8] using 300 g of cement with the MOSP in proportions of 0%, 0.2%, 0.5%, 2%, 3%, and 5% by wt. % of cement, and mixing kept within the stipulated 5 minutes. The results are shown in Table 5.

Table 5. Consistency and Setting Time of MOSP-Paste

Mix No	Consistency (%)	Initial setting time (Mins)	Final setting time (Mins)
M-0.0 MSP	34	105	253
M-0.2 MSP	34	118	274
M-0.5 MSP	34	121	293
M-1.0 MSP	34	142	368
M-2.0 MSP	35	179	457
M-3.0 MSP	37	203	552
M-5.0 MSP	38	365	703

While the MOSP-concrete was on the slump, density, water absorption, and compressive strength. The studies on the MOSP-concrete were done using a concrete mix of 1: 1.7: 2.5 with a cement content of 420 kg-m^3, fine and coarse aggregates of 708 kg-m^3 and 1062 kg-m^3, respectively, and a water-cementitious ratio of 0.5. The slump of the MOSP-concrete was in the fresh condition, and carried out in accordance with BS EN 12350-2 [9], using a truncated cone of 300 mm high with the bottom and top diameters as 200 mm and 100 mm, respectively. This was studied using replacement levels of MOSP by wt. % of cement from 0% to 5%. The results are shown in Table 6.

The density, water absorption and compressive strength were conducted in accordance with BS 1881 Part 122 [10], BS EN 12390-7 [11], and BS EN 12390-3 [12], respectively, The cube compressive strength was studied using a cube mold of 100 mm, and a total of seven (7) mixes were used and designated as 0.0% MOSPC, 0.2% MOSPC, 0.5% MOSPC, 1.0% MOSPC, 2.0% MOSPC, 3.0% MOSPC, and 5.0% MOSPC. The 0.0% MOSPC was the control, containing 0 % MOSP, while other mixes contained MOSP in proportions of the cement by wt. %. The total number of cube samples cast and cured from 3 days to 90 days was 105, three for each age, and at the end of each curing regime, three of the specimens were tested to failure and the average recorded. The compressive strength testing was done using the ELE Compression Machine with 2000 kN capacity and tested in accordance with 12390-3 [12]. The results on the slump, density, water absorption and compressive strength are shown in Tables 6 and 7.

Table 6. Slump of MOSP-Concrete

Mix No	Slump
M-0.0/ MOSPP	23
M-0.2 /MOSPP	26
M-0.5/ MOSPP	26
M-1.0 /MOSPP	29
M-2.0 /MOSPP	35
M-3.0/ MOSPP	45
M-5.0/ MOSPP	48

DOI: https://doi.org/10.30564/jbms.v3i2.3735

Table 7. Characteristics of MOSP-Concrete

Property	Mix No	Age (Days)				
		3	7	28	60	90
Water Absorption (%)	M-0.0/ MOSPC	0.7	1.0	1.5	1.8	2.3
	M-0.2/ MOSPC	0.8	1.1	1.6	1.9	3.0
	M-0.5 /MOSPC	0.8	1.1	1.7	2.2	3.7
	M-1.0/ MOSPC	0.9	1.2	1.8	2.6	4.3
	M-2,0/ MOSPC	1.0	1.8	2.0	2.7	4.7
	M-3.0/ MOSPC	1.2	1.6	2.1	2.8	5.1
	M-5.O/ MOSPC	1.4	2.0	2.2	3.2	6.0
Density(kg/m^3)	M-0.0 /MOSPC	2583	2613	2637	2607	2590
	M-0.2 /MOSPC	2650	2567	2587	2513	2527
	M-0.5 /MOSPC	2510	2667	2587	2617	2590
	M-1.0 /MOSPC	2590	2650	2610	2553	2547
	M-2,0 /MOSPC	2627	2597	2590.	2523.	2543.
	M-3.0 /MOSPC	2587	2583	2597	2530	2533
	M-5.O /MOSPC	2510	2503	2513	2513	2507
Compressive Strength (kN/m^2)	M-0.0 /MOSPC	14.0	18.0	20.7	22.0	24.0
	M-0.2 /MOSPC	17.0	19.9	25.3	27,0	27.1
	M-0.5 /MOSPC	14.4	16.3	24.0	25.3	23.9
	M-1.0 /MOSPC	12.5	15.0	18.4	19.5	17.6
	M-2,0 /MOSPC	12.2	14.7	17.9	18.9	17.5
	M-3.0 /MOSPC	11.7	14.5	16.1	17.6	14.8
	M-5.O /MOSPC	0.50	0.60	3.9	5.6	4.9

X-ray diffraction characterization of moringa oleifera seed powder and concrete

The second phase was the x-ray diffraction analysis on crushed cube compressive strength of the MOSP-concrete samples used for the investigation. This was taken at the replacement that gave the optimum strength, that was at 0.2% by wt. % of cement and cured from 3 to 90 days. These were matched with the control samples containing 0.0% MOSPC, and cured for the same period of days. The moringa oleifera seed was grinded into powder and sieved using sieve size 150μm. XRD is a nondestructive technique that provides detailed information about the crystallographic structure, chemical composition, and physical properties of materials. A Brunker-AXS D8 advanced equipment was used for the x-ray diffraction analysis. This was based on Bragg's law ($n\lambda = 2d\sin\lambda$), and recorded on an X-ray diffractometer operating at known voltages and current using a Cu Kα X-rays (α = 0.15406 nm) over the 2θ range from 10 to 100 degrees in the steps of 0.01 degree at room temperature in open quartz sample holders. The results are shown in Figures 3 and 4. The characteristics of x-ray diffraction peaks are shown in Figure 5.

 DOI: https://doi.org/10.30564/jbms.v3i2.3735

X-ray diffractogm of moringa oleifera seed powder Concrete

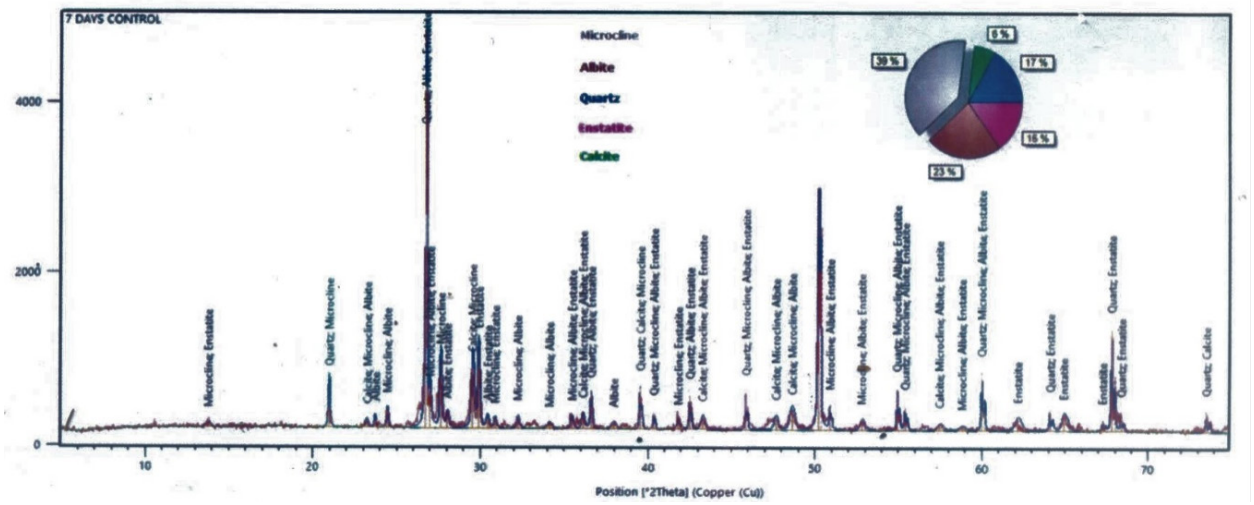

7 days

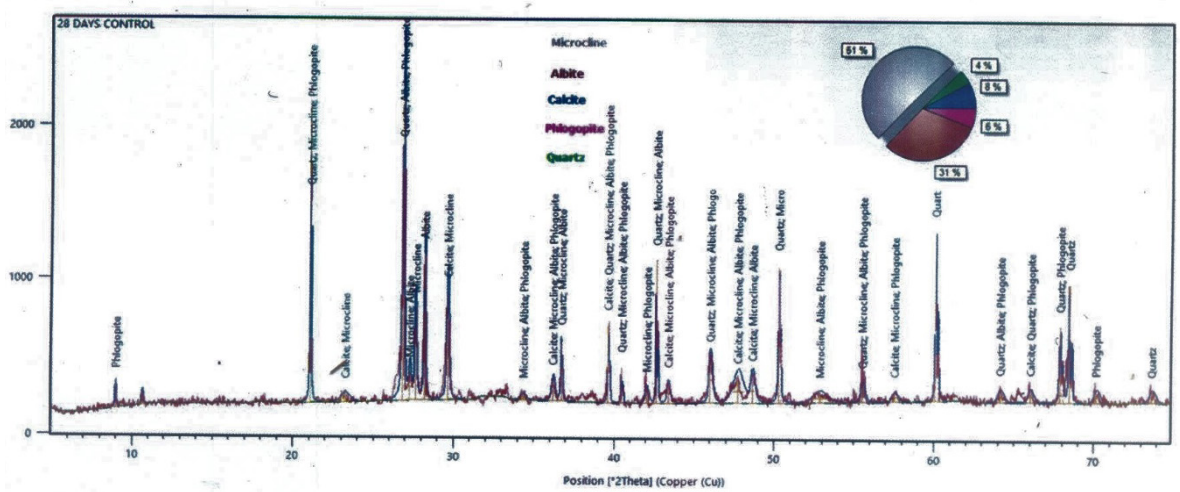

28 days

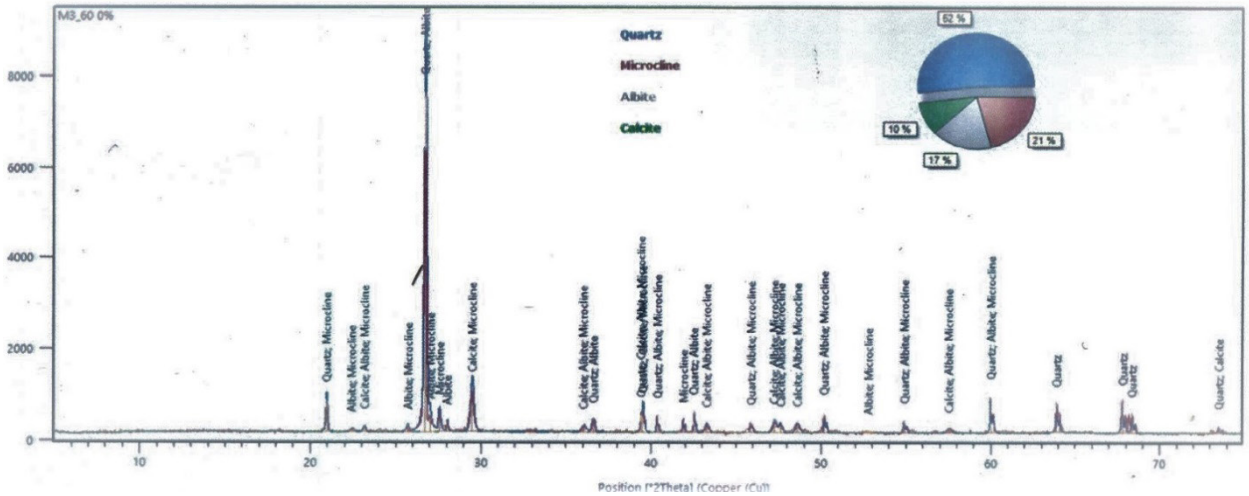

60 days

Figure 3. Control Samples of XRD MOSPC

DOI: https://doi.org/10.30564/jbms.v3i2.3735

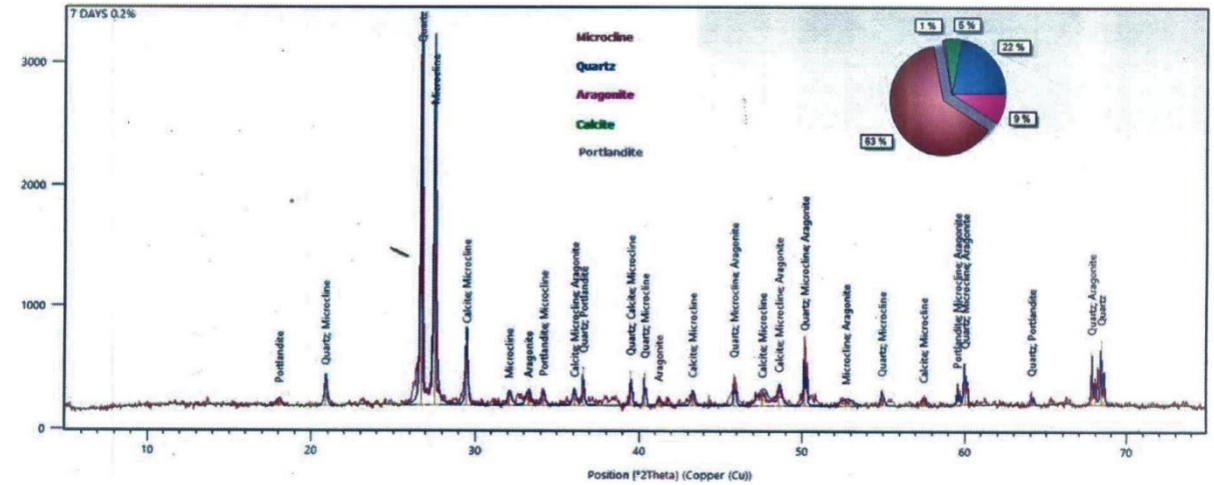

7 days

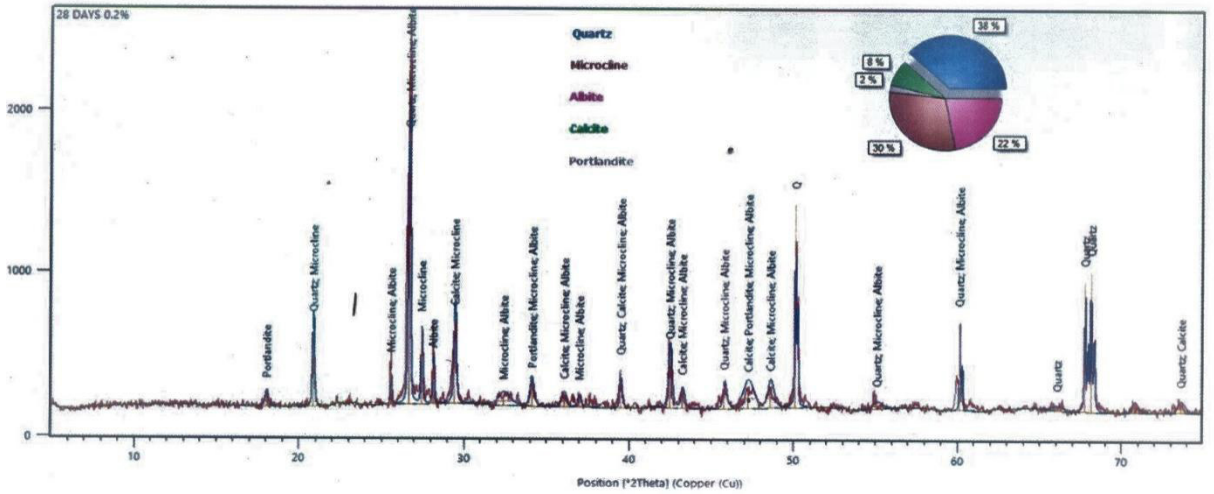

28 days

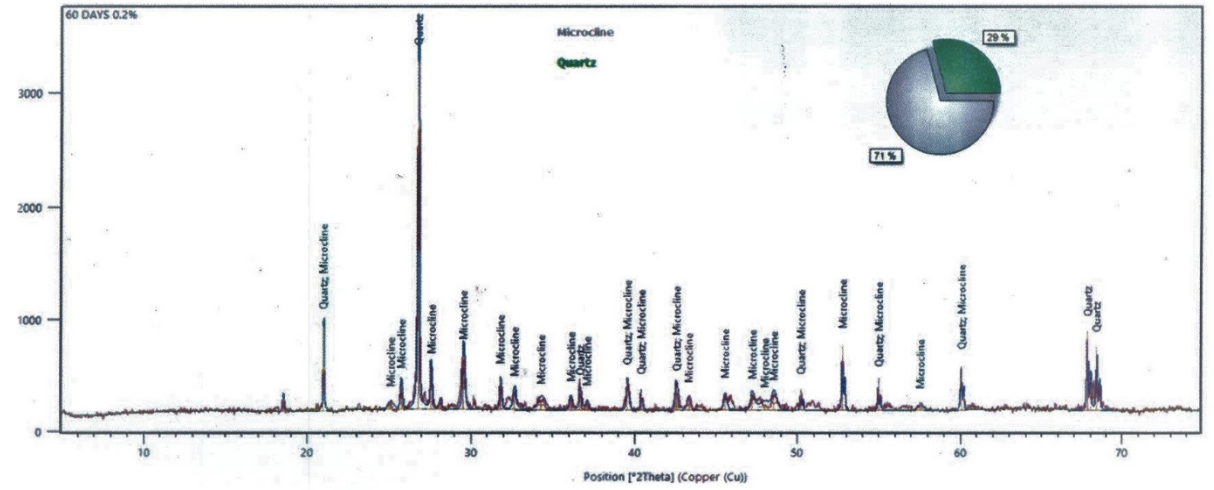

60 days

Figure 4. 0.2% Addition to Samples of XRD MOSPC

 DOI: https://doi.org/10.30564/jbms.v3i2.3735

Microstructure and Acid-Base Resistance of MOSP-Concrete

The third phase was experimental set-up for the study on the microstructure and acid and sulphate resistance of MOSP-concrete. The samples for this phase were taken from the crushed samples on the cube compressive strengths at the optimum replacement of cement by wt. % which was at 0.2% MOSP for ages of 3 to 90 days.

The study on the microstructure was carried out using scanning electron microscope (SEM-Hitachi S4100) equipped with energy dispersion spectroscopy, EDS-Rontec), at 5kV and 25 kV. Thin sections mounted on glass slides were prepared from the crushed samples, and observed using the SEM. The micrographs are shown in Figure 5. For the study on the acid- sulphate resistance, the acids and sulphates were 20% dilutions. The media used were H_2SO_4, and HNO_3 for the acids, and Na_2SO_4 and $MgSO_4$, for the sulphates. The procedure was weighing a selected crushed sample, weighed and recorded as initial weight (W_1), then immersed in the selected medium for periods of 56 days at 7 days interval, weighed and recorded as the final weight (W_2). At the end of each curing regime, it was removed, rinsed by sprinkling a little water, and allowed for some seconds to dry. The sample was weighed and the weight recorded. An average of two measurements was recorded and the percentage wt. loss was calculated as:

$$Wt.\ loss\ (\%) = \frac{W_1 - W_2}{W_1}\ x\ 100 \quad (1)$$

Where: W_1 and W_2 are the initial and final weights of the sample. The results are shown Tables 8 and 9.

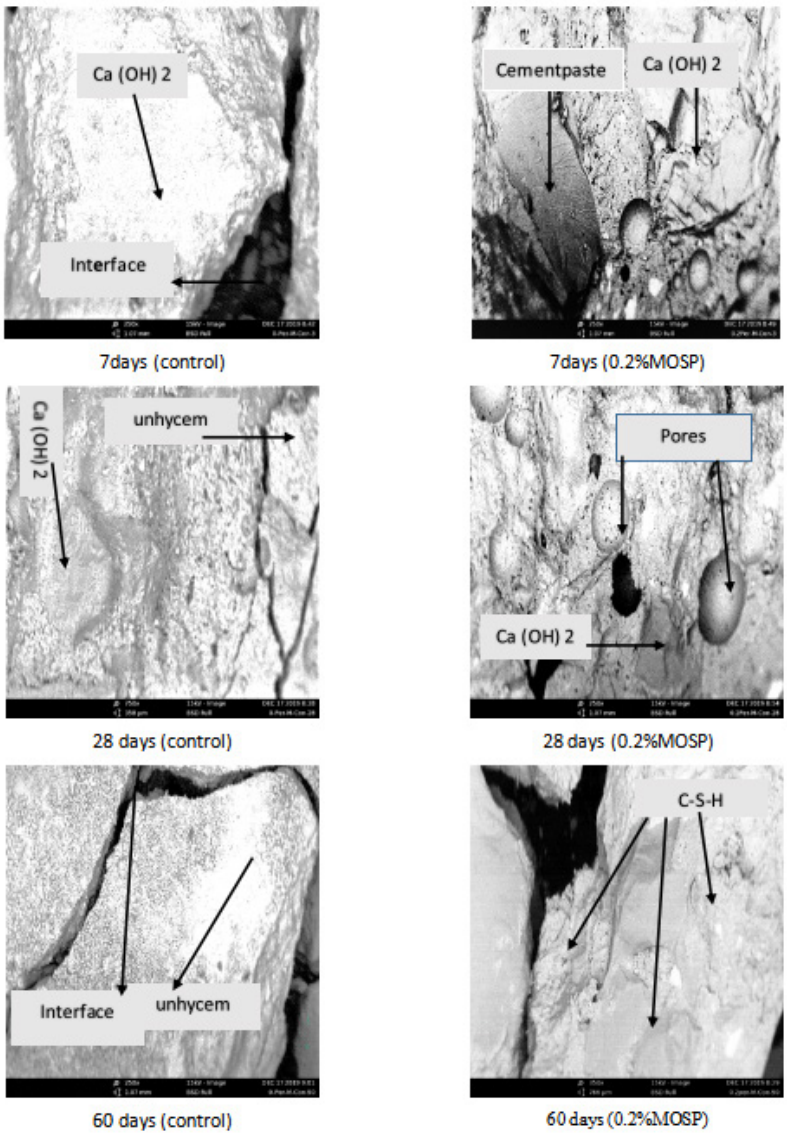

Figure 5. Micrograph of MOSP-Concrete

DOI: https://doi.org/10.30564/jbms.v3i2.3735

Table 8. Acid Resistance of MOSP-Concrete

Age (Days)	Mix	Medium	Percentage Decay (%)							
			7 d	14 d	21 d	28 d	35 d	42 d	49 d	56 d
3	0.0% MSOP	20 % HNO_3	-8.3	-7.5	-26.2	-9.7	-21.6	-9.9	-8.5	-18.5
7			-14.5	-6.0	-6.6	-10.6	-6.0	-8.2	-10.2	-13.6
28			-20.1	-9.0	-15.5	-29.8	-16.7	-10.2	-18.1	-10.6
60			-17.3	-15.7	-4.8	-5.5	-10.3	-18.6	-16.8	-18.4
90			-13.7	-10.9	-24.0	-3.0	-15.2	-16.8	-11.8	-18.4
3	0.2% MOSP		-29.8	-14.3	-9.5	-13.6	-24.6	-15.9	-7.2	-15.8
7			-10.2	-4.8	-11.5	-10.4	-4.2	-10.7	-6.9	-13.9
28			-27.5	-12.7	-8.0	-6.8	-12.1	-8.8	-20.6	-16.0
60			-12.4	-8.2	-10.4	-4.9	-3.7	-20.5	-16.1	-26.4
90			-13.0	-12.5	-3.4	-4.9	-1.6	-17.1	-13.2	-21.6
3	0.0 % MOSP	20 % H_2SO_4	-66.5	-34.0	-28.9	-36.6	-49.5	-57.6	-44.0	-41.7
7			-26.6	-48.0	-50.0	-46.1	-36.1	-38.8	-26.5	-37.4
28			-50.5	-64.0	-35.0	-37.6	-21.4	-52.0	-55.3	-1.3
60			-49.5	-56.2	-46.9	-62.1	-28.7	-49.6	-49.0	-42.2
90			-32.4	-12.2	-19.6	-52.7	-36.8	-41.6	-40.8	50.0
3	0.2% MOSP		-60.3	-59.9	-37.8	-29.5	-23.3	-30.6	-27.8	-34.0
7			-39.8	-55.5	-52.7	-34.5	-35.4	-23.3	-27.1	25.2
28			-52.3	-48.7	-61.7	-26.6	-46.6	-29.5	-27.7	22.6
60			-61.5	-53.3	-68.2	-24.0	-38.8	-31.7	-32.1	-26.3
90			-67.2	-58.8	-63.9	-9.6	-28.6	27.6	-40.7	-20.1

Table 9. Base Resistance of MOSP-Concrete

Age (days)	Mix	Medium	Percentage Growth ((%)							
			7d	14d	21d	28d	35d	42d	49d	56d
3	0.0 % MOSP	20 % $Na2SO_4$	3.6	11.0	5.9	6.9	16.9	5.1	2.7	4.7
7			5.0	8.6	6.3	8.1	5.1	6.1	21.8	39.6
28			9.0	3.8	18.1	13.9	12.2	7.4	14.7	10.6
60			0.6	6.3	10.5	4.3	9.9	7.9	2.4	8.8
90			3.2	7.6	4.1	18.4	7.8	6.8	14.6	1.7
3	0.2 % MOSP		7.0	3.8	7.2	3.3	6.4	7.5	9.4	5.2
7			7.8	3.5	8.4	3.0	6.1	9.2	8.9	5.8
28			5.9	4.3	5.4	3.8	3.5	12.0	8.89	9.3
60			5.4	8.2	4.3	2.6	7.0	9.1	7.6	5.2
90			5.7	8.0	9.0	2.0	4.3	6.9	9.1	17.1
3	0.0 % MOSP	20 % $MgSO_4$	4.2	4.6	12.6	8.3	7.5	22.0	2.7	7.7
7			5.3	6.9	2.4	5.6	6.47	6.9	6.5	14.6
28			9.5	4.7	9.2	6.5	10.0	18.7	7.5	7.7
60			7.2	8.1	7.7	5.7	8.5	5.0	8.2	10.3
90			4.8	6.0	17.7	9.6	10.1	7.7	7.5	3.7
3	0.2 % MOSP		9.4	5.2	6.7	4.9	6.0	9.1	8.5	3.3
7			5.2	3.8	8.9	6.3	8.5	8.5	10.3	3.5
28			6.7	4.9	8.0	4.5	9.5	6.8	12.2	7.5
60			9.6	6.3	3.6	4.9	10.7	30.9	12.3	7.4
90			7.2	3.3	7.5	5.8	6.7	12.7	5.8	6.4

 DOI: https://doi.org/10.30564/jbms.v3i2.3735

4. Discussion

Characteristics of MOSP

The major oxides in cement include CaO, SiO_2, Al_2O_3, and Fe_2O_3, while the minor oxides are SO_3, MgO, Na_2O and K_2O. Table 4 showed two outstanding and distinct chemical compounds in the chemical composition of MOSP. These are SO_3 (~28%) and Fe_2O_3 (~18%), respectively, which may primarily dictate the performance of MOSP as a composite material with concrete. The other relatively high elements are P_2O_5 (8%), CaO (8%), Al_2O_3 (6%), and SiO_2 (6%) respectively. SO_3 and TiO_2 with pH, approximately 7, are acidic oxides. They are therefore, corrosive to metals and also react with the alkalis [13]. The permissible level of SO_3 is in the range of 1-3% as against the 28% from Table 4. Horkoss et al studies were on the effects of SO_3 on the expansion of mortars, and showed that the cement produced with high sulphur clinker had lower expansion. He also observed that if the percentage surpassed the level of 3.5% it could increase the risk of DEF [14]. Therefore, the SO_3 content of 28.31% in MOSP, which exceeded the permitted range of (1-3)% must be of great interest as MOSP is proposed for use in concrete. Equally of concern are the percentage presence of K_2O (7.53% and Na_2O (1.40%), collectively called the alkalis, specified not to be greater than 0.4-1.3%. The alkalis react with active silica in aggregate to produce alkali-silica gel responsible for swelling under favorable conditions of moisture and temperature in voids and cracks [15]. With the works of Horkoss et al [16] SO_3 high content may not be a disadvantage but an advantage as it causes strength development to be slow (Retarder). Retarders are advised for hot weather concreting. High content of SO_3 from their works confirmed that it could form a resistance to sulphate attack. Again, the excess of phosphorous content of 2.0% will reduce C_3S content, and slow the hydration reaction, thereby, prolonging the induction [17].

Figures 1 and 2 show the diffractogramme and the microstructture of MOSP. Yhe XRD peaks and the pattern are shown below the diffractogramme. The peaks show that MOSP is not crystalline in nature but amorphous. The dominant minerals are cristobalite and quartz. Cristobalite (Si_8O_{16}) and quartz (Si_3O_6) are polymorphs of SiO_2. The solubility of silica minerals is a function of chemical composition, and the presence of a disrupted surface layer [18]. Quartz dictated in the sample is a hard, crystalline mineral composed as silica (silicon dioxide), whose atoms are linked in a continuous framework of SiO_4 silcon-oxygen tetrahedral, with each oxygen being shared between two tetrahedral. This gives an overall chemical formula of SiO_2. The four peaks are as shown.

Characteristics of MOSP-Paste and Slump (Fresh Concrete)

Figure 6 shows the plots of consistency of MOSP cement paste. Consistency is the water affinity of the material as it goes into reaction in the cement paste (the degree of wetness). The result showed that at replacement levels of 0% to 1.0%, the water requirement remained approximately constant at 34%. But beyond the replacement of 1.0% the water requirement continued to increase, and the increase recorded were 2.9%, 8.8%

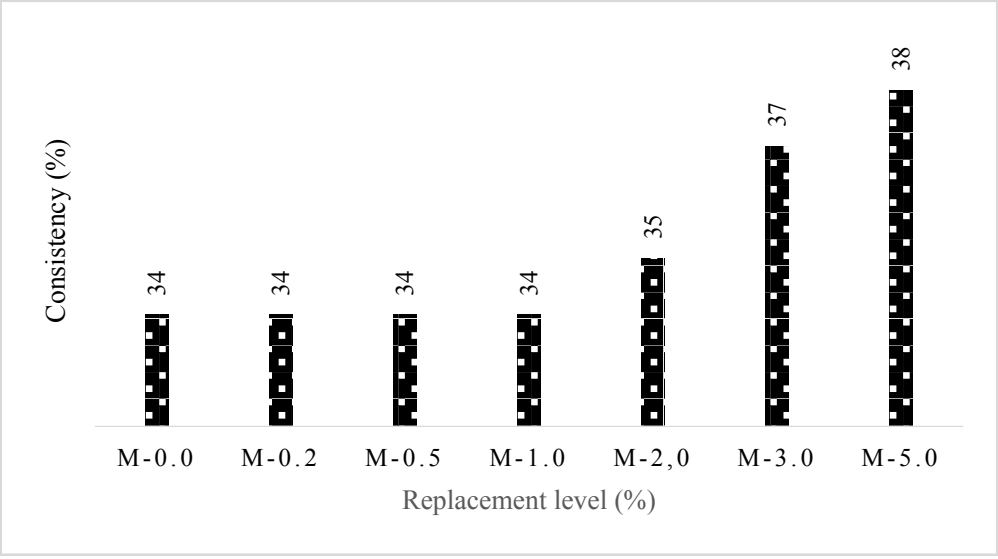

Figure 6. Consistency of MOSP-Paste

DOI: https://doi.org/10.30564/jbms.v3i2.3735

and 11.8% to the control. Above 1.0% replacement the possible explanation meanwhile could be attributed to the harshness of the paste, and therefore, for nonporous concrete the water requirement should not be greater than 34% and cement replacement with MOSP by wt. % should not be > 1.0%.

Figure 7 is the setting times of the MOSP cement paste. Setting properties of concrete is the most important in the field of concrete works because it helps in the various concrete operations. The physical properties of MOSP morphologically are hollowed granule and armophous. It has been reported that such physical properties caused the powder become pasta if added with certain amount of water [19], and also tends to form agglomerate morphologically [20]. The main cause of cement setting is the onset of the formation of C-S-H, and defined as the mechanism that governs the transition from plastic phase to hardened one, characterized by an increase in the system viscosity [14]. Figure 6 showed a steady increase both for the initial and final setting times. The final setting time for replacements up to 3.0% of cement by MOSP did not exceed the 10 hours stipulated by the code. Above 3.0% the stipulated time of 10hrs was exceeded. We can therefore conclude that it may be safe to use MOSP for concrete to a level of replacement not exceeding 3.0% wt. % of cement. Although, the 3.0% by wt. % replacement may seem to have satisfied the setting time of 10 hrs stipulated. It is however safer to limit the replacements to between 0.2% and 0.5% because of the SO_3 content pending further works with the material. This

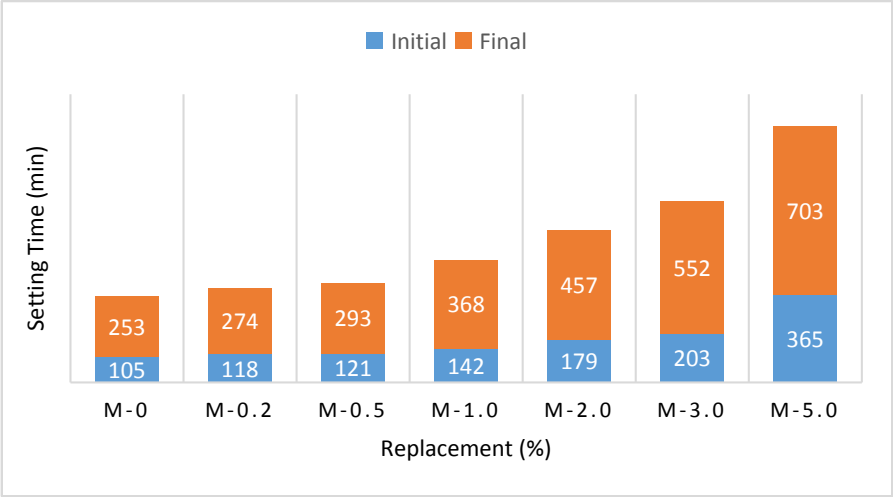

Figure 7. Setting Times of MOSP Cement Paste

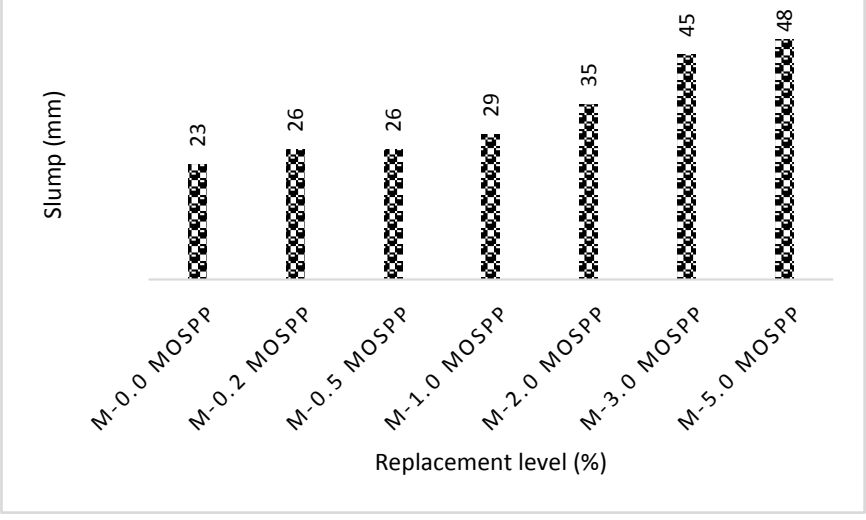

Figure 8. Slump of MOSP-Concrete

 DOI: https://doi.org/10.30564/jbms.v3i2.3735

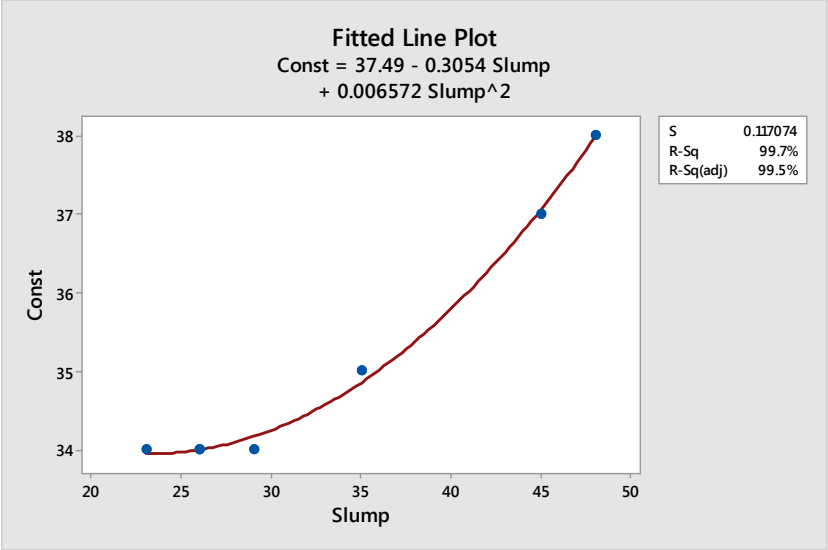

Figure 9. Consistency against the Slump

decision is based on suggestions of some researchers on the regulation of gypsum content in cementitious systems because of cement strength and its dimensional stability. They believed it may affect durability of cement concrete and thereby, cause serious damages [15]. High content of gypsum in cement was also considered as one of the main causes of DEF, and therefore limiting sulfate additions in cement is common to avoid DEF. This was also supported by the findings of Sayed Horkoss et al [16], who held a contrary view on cement produced with high sulfur clinker. They concluded that it gave a lower expansion to other types of gypsum. Therefore, in the applications of MOSP in cement concrete, we must be cautious because of the high SO_3 content. This work proposes to keep the replacement levels of MOSP at 0.2% and 0.5%, because of the SO_3 content, pending further works with this material. MOSP can also be used for hot weather concreting where enough time is needed to place the concrete due high temperature.

The slump of the MOSP concrete is shown in Figure 8 which is an expression of the workability of the concrete. The workability depends on the size and amount of the fine and coarse aggregates. The results showed that the use of MOSP in concrete will improve the workability of the concrete. An empirical relationship has been established between the consistency of MOSP-paste and the slump. This is given as Consistency = 37.49 +0.31slump + 0.001 slump2 with a standard deviation (s) of 0.1171, and a correlation factor of 99.7%. This is shown in Figure 9.

Mechanical strength of MOSP-concrete

The water absorption results showed increase as the replacement levels and age increased (Table 7). The replacement level of 0.2% gave the best behavior and thus could be said to be the optimum replacement level for best performance (Figure 10). This can also alley the fears raised on the setting times, limiting replacements from 0.2% to 0.3% by wt. % of cement. We can therefore conclude that the use of MOSP in concrete increased the water absorption. The differences in water absorption at 28 days and 90 days of curing were 2% to 41%, and 31% to 158%, respectively (Figure 11). The density of MOSP-concrete is a normal weight concrete as shown in Figure 12, and can achieve a value up to 2667 kg-m^3. The high value of the density could be attributed to the density of the MOSP which is approximately twice the density of cement.

From Figure 13, the compressive strength of MOSP-concrete increased as the replacements of cement by wt. % of MOSP were increased. The results showed that the compressive strength increased as MOSP by wt. % is increased for all ages of concrete specimen, up to 0.2% and 0.5%, with the best performance at 0.2%. This optimum was also achieved by Susilorini et al [2,3]. Although, it is observed that the compressive strength increased with age of curing above 0.5% replacement, however, increasing MOSP content decreased the compressive strength. The desired design strength of 20 kN-m^2 was satisfied by 0.2% and 0.5% replacements, respectively, that for 0.2% was achieved at the ages of 7 days (~20.0 kn-m^2), 28 days (25 kN-m^2), 60 days (27 kN-m^2), and 90 days (27 kN-m^2), while that for the 0.5 % was achieved at ages of 28 days (24 kN-m^2), 60 days (25 kN-m^2), and 90 days (~24 kN-m^2), respectively. These classes of concrete could be used for reinforced concrete members. For higher replacements of 1%, 2%, and 3%, they could not attain the desired strength of 20 kN-m^2,

DOI: https://doi.org/10.30564/jbms.v3i2.3735

but could equally be used for non-load bearing members such as lintels, foundation concrete, etc. The percentage strength differences are shown in Figure 14. The SO_3 levels at 0.2% and 0.5% MOSP can be said to favor better production of hydrate generators of bonding properties which led to the increase in compressive strength. The decrease of resistance beyond the levels of 0.2% and 0.5% confirmed that there is an optimum content above which the strength gradually decreased.

X-Ray Diffraction Analysis of MOSP-Concrete

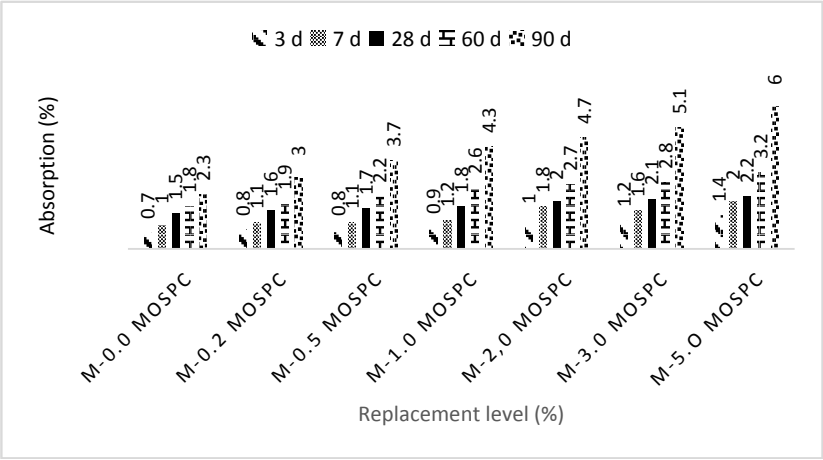

Figure 10. Water Absorption of MOSP-Concrete

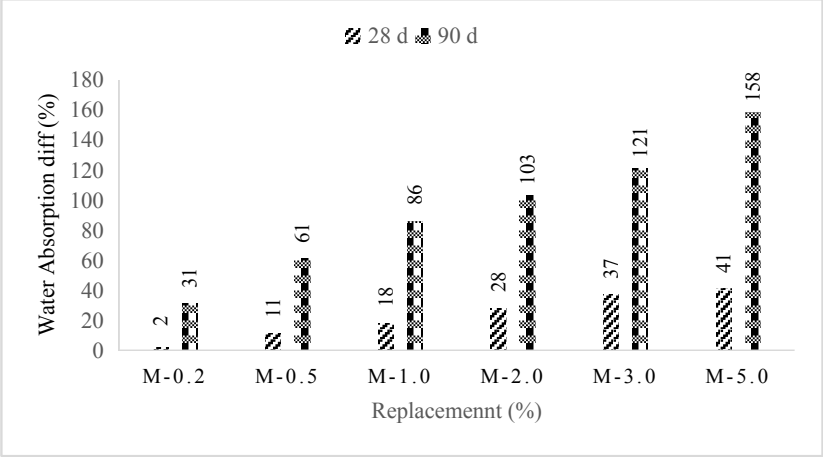

Figure 11. Water Absorption Difference (%)

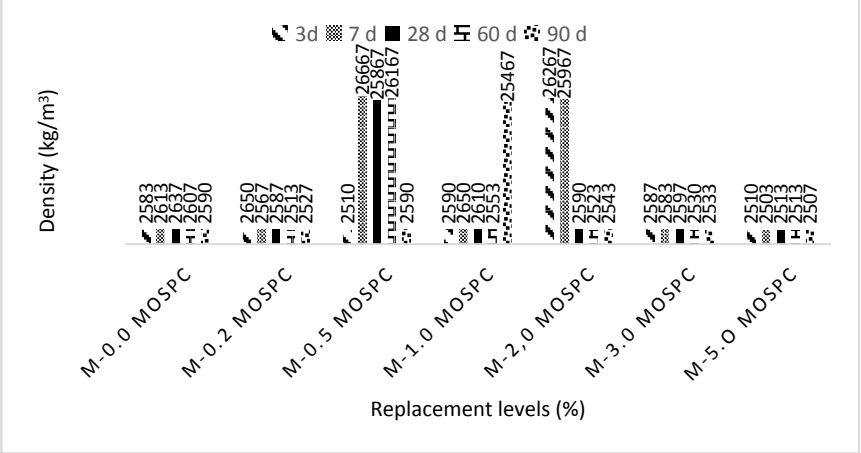

Figure 12. Density of MOSP-Concrete

Distributed under creative commons license 4.0 DOI: https://doi.org/10.30564/jbms.v3i2.3735

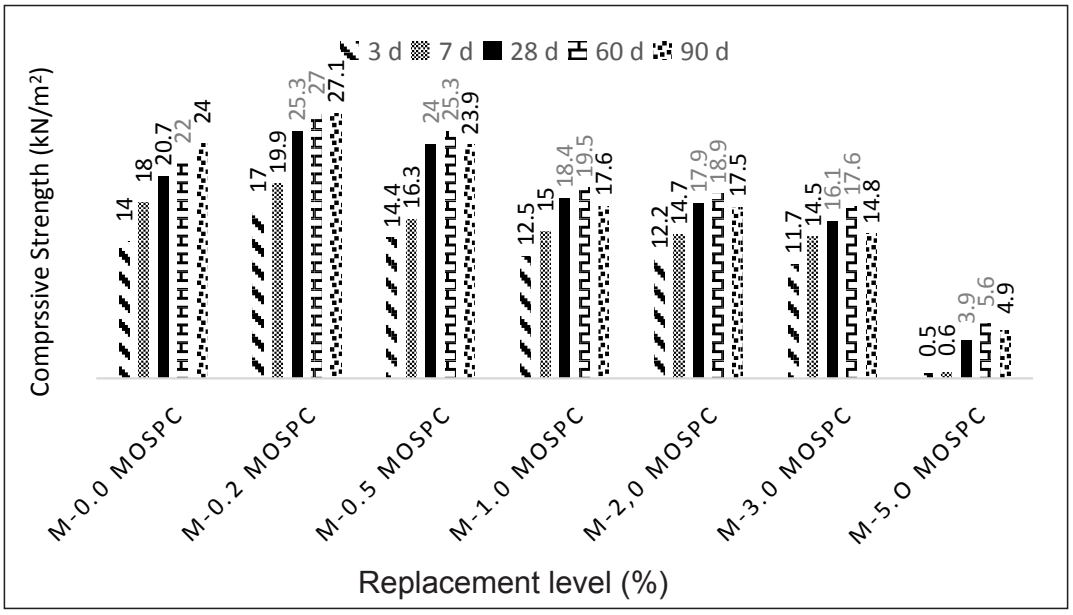

Figure 13. Compressive Strength of MOSP-Concrete

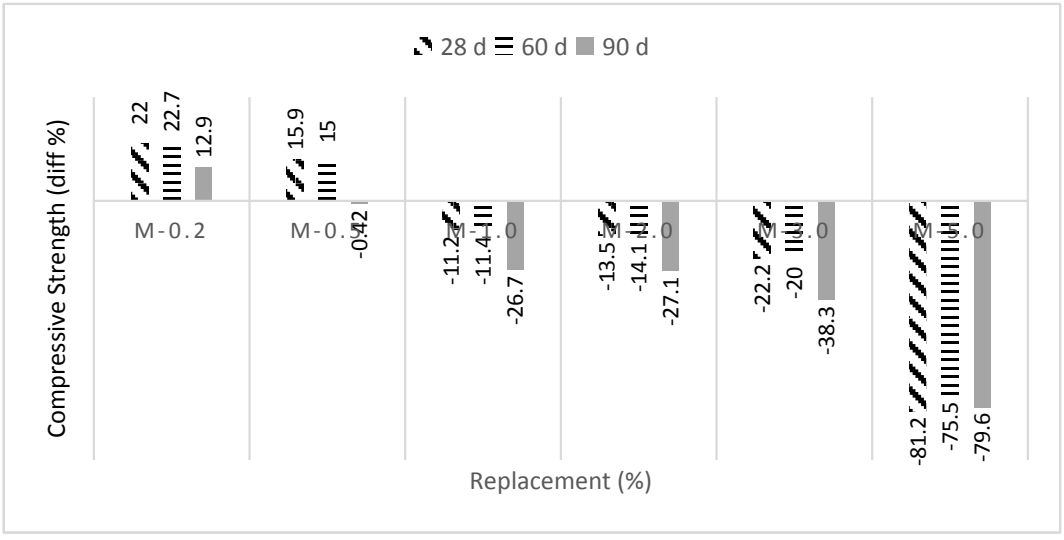

Figure 14. Compressive Strength Difference (%)

Figure 15 is information extracted from the x-ray diffractogrammes shown in Figures 3 and 4. It show that the quartz and microcline minerals are dictated at all ages of the samples (Control and 0.2% MOSP) but having various percentages. The two dominant minerals remaining at the end of the hydration process at the age of 60 days, for the 0.2% MOSP samples, were quartz and microcline. The percentage increase at 0.2% MOSP for quartz and microcline were approximately 37% and 43% respectively. While the percentage of quartz continued to increase, microcline remained constant above 28 days. Another dominant minerals are calcite and albite. Calcite is a polymorphy of calcium cabornate ($CaCO_3$). However, both disappeared at 28 days of curing. While albite was increasing, calcite decreased. The percentage increase and decrease with the control were 29% and 30% respectively. The presence of Portlandite at 7 and 28 days, and Araganite at 7 days, in the 0.2% MOSP has no explanation meanwhile. Enstaite and phlogophite dictated in the control samples were not found in the 0.2% MOSP samples.

DOI: https://doi.org/10.30564/jbms.v3i2.3735

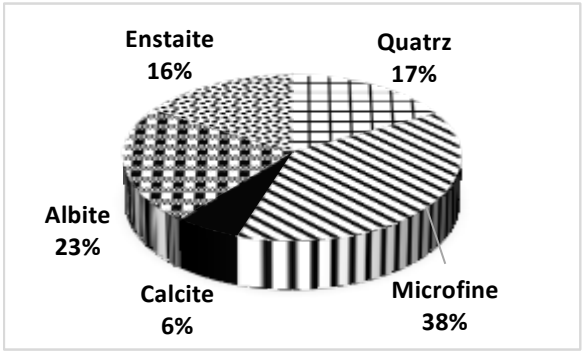

Seven Days-Control (0%MOSP)

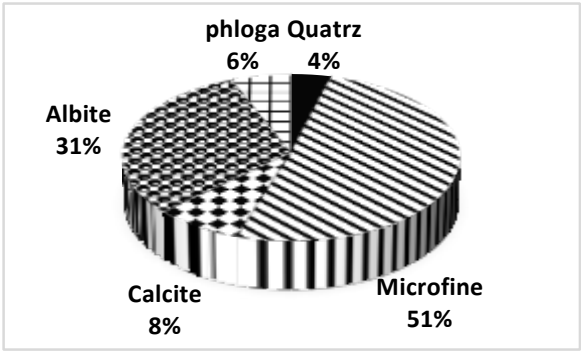

Twenty Eight-Day Control (0% MOSP)

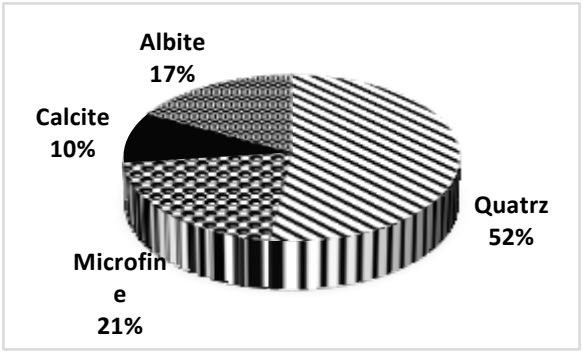

Sixty-Day Control (0% MOSP)

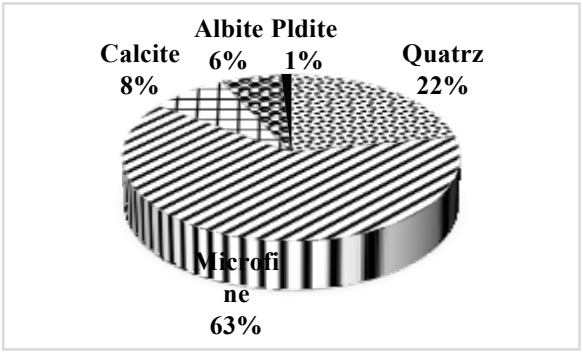

Seven-Day (0.2% MOSP)

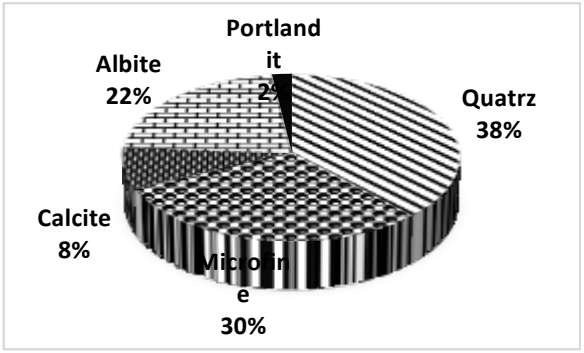

Twenty Eight-Day (0.2% MOSP)

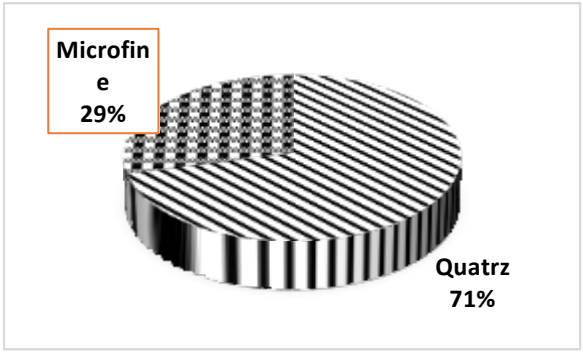

Sixty-Day (0.2 % MOSP)

Figure 15. Characteristics of x-ray diffraction peaks of MOSP-concrete

Microstructure Characteristics from the Micrograph of MOSP-Concrete

Figures 5 and 16 show the SEM of the MOSP-concrete and their mineral characteristics at the ages of 7, 28 and 60 days, respectively. Affecting factor for the effectivity of MOSP as an additive is the active compounds of the powder. When used as an additive or replacement material, the active compounds are dissolved in water and eventually go through hydration processes, modifying the end products (Figure 5). The size (212 µm) and physical properties of MOSP affect the amount of dissolved active compounds in water. Other studies about SEM result of MOSP indicated that the powder tends to form agglomerate morphologically [19].

At seven days of curing quartz, microfine, calcite and albite were dictated for both the control (0%) mix and the mix containing 0.2% MOSP but at various magnitude. However, enstaite and portlandite were peculiar as the case may be, to the control mix and the 0.2% mix, respectively. The view from Figure 5 showed agglomerate effects on the mix with 0.2%. The 28-day mineral characteristics showed that quartz, microfine, calcite, and

 DOI: https://doi.org/10.30564/jbms.v3i2.3735

albite were dictated. However, quartz and albite contents increased, while microfine decreased. These were opposite to the observed effects at 7-days. At 60 days only quartz and microfine were dictated, while calcite and albite had totally disappeared. The interpretation of this from Figure 5 showed that $Ca(OH)_2$ and the bubbles (porosity) noticed at 28 days have all disappeared and formed C-S-H responsible for strength. From understanding of hydration reactions of cement the predominant phases present in hardened concrete are monosulphate, Tobermorite (C-S-H) and portlandite, along with unreacted cement compounds and ettringite.

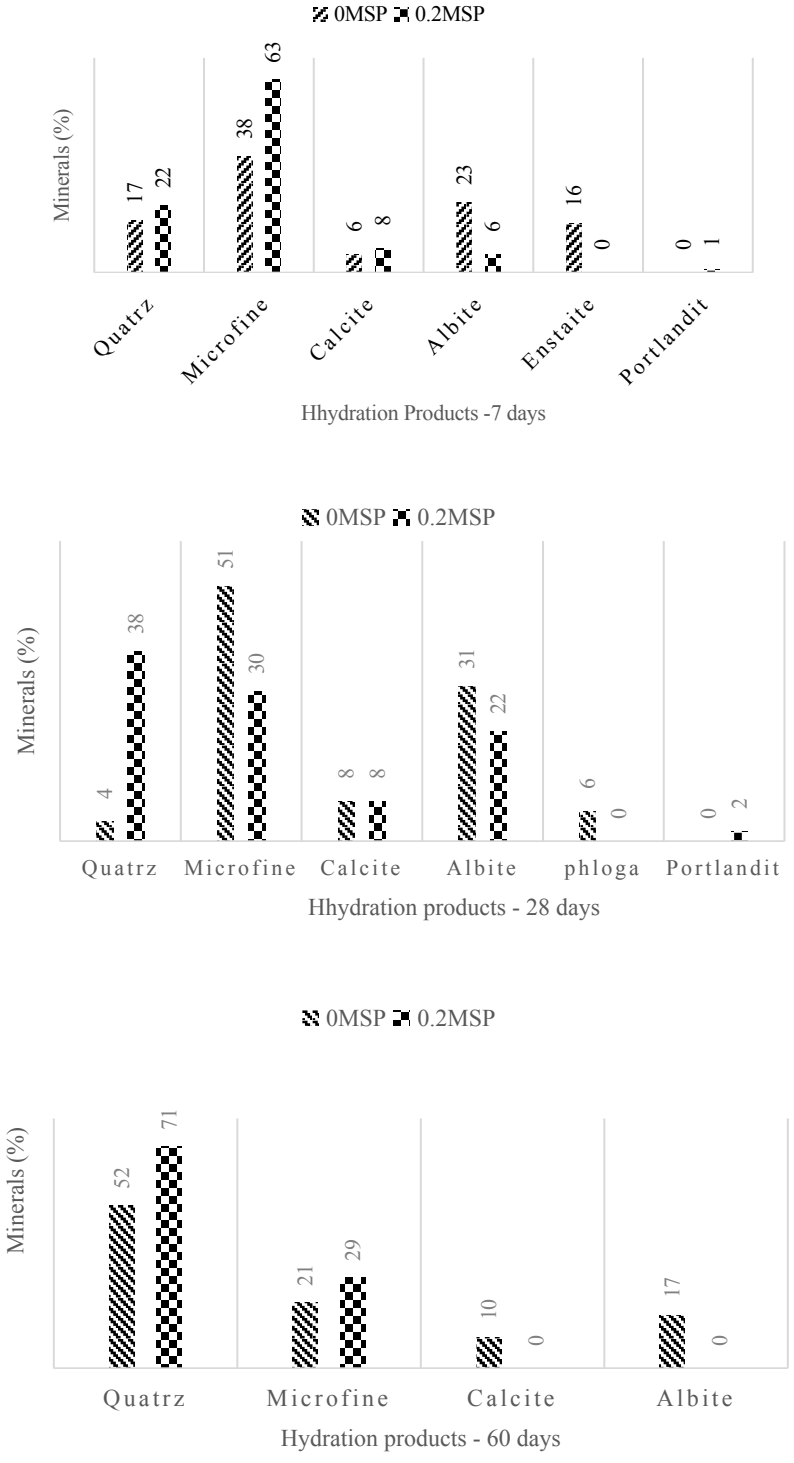

Figure 16. Hydration Products from the Micrograph

DOI: https://doi.org/10.30564/jbms.v3i2.3735

Acid-Sulphate Characteristics of MOSP-Concrete

The presentations shown in Tables 10 and 11 are analysis performed on the crushed samples in the acid and sulphate media (Tables 8 and 9). Table 10 is the statistical characteristics of the performances in the various medium, while Table 11 is the summary. The Means of HNO_3 (-11.5%) and H_2SO_4 (-41.4%) showed deterioration effects (decrease) while, that of Na_2SO_4 (9.0%) and $MgSO_4$ (8.1%) exhibited some swelling (increase). The decay was more drastic on H_2SO_4 medium than in HNO_3 medium. The difference was approximately 260%. The growth between the Na_2SO_4 and $MgSO_4$ was marginal, and approximately 10%.

Table 10. Statistical Characteristics of the MOSP-Concrete Samples in Acid and Base Medium

Medium 20% Dilution	Mix	Age (Days)	Mean	SEMean	StDev	Variance	CoefVar
HNO_3	0%MOSP	3	-13.8	2.6	7.2	52.4	-52.6
		7	-9.5	1.2	3.3	11.2	-35.3
		28	-16.3	2.4	6.8	46.2	-41.9
		60	-13.4	2.0	5.7	32.9	-42.7
		90	-14.2	2.2	6.1	37.7	-43.2
		Average	-11.5				
	0.2%MOSP	3	-16.3	2.7	7.5	56.4	-46.0
		7	-9.1	1.2	3.4	11.7	-37.6
		28	-14.1	2.5	7.1	50.0	-50.3
		60	-12.8	2.8	7.8	61.1	-60.9
		90	-10.9	2.5	7.0	49.1	-64.2
		Average	-12.6				
H_2SO_4	0% MOSP	3	-44.9	4.4	12.6	157.7	-28.0
		7	-38.7	3.2	9.0	81.8	-23.4
		28	-39.4	7.2	20.3	411.2	-51.5
		60	-48.0	3.5	9.9	97.0	-20.5
		90	-35.8	5.0	14.0	196.8	-39.2
		Average	-41.4				
	0.2 % MOSP	3	-37.9	5.1	14.3	205.7	-37.8
		7	-36.7	4.3	12.1	147.1	-33.1
		28	-39.5	5.2	14.6	211.9	-36.9
		60	-42.0	5.9	16.8	282.7	-40.1
		90	-39.6	7.6	21.6	466.8	-54.6
		Average	-39.1				
Na_2SO_4	0%MOSP	3	7.1	1.7	4.7	22.0	66.1
		7	12.6	4.3	12.2	149.4	97.2
		28	11.2	1.6	4.5	20.4	40.3
		60	6.3	1.3	3.6	13.0	56.9
		90	8.0	2.0	5.8	33.0	71.6
		Average	9.0				
	0.2%MOSP	3	6.2	0.7	2.0	4.1	32.6
		7	6.6	0.8	2.4	5.7	36.4
		28	6.6	1.1	3.1	9.5	46.4
		60	6.2	0.8	2.2	4.7	35.3
		90	7.8	1.6	4.5	20.1	57.8
		Average	6.7				
$MgSO_4$	0%MOSP	3	8.7	2.2	6.2	38.3	71.1
		7	6.8	1.2	3.5	12.0	50.7
		28	9.2	1.5	4.2	17.7	45.6
		60	7.6	0.6	1.7	2.8	21.9
		90	8.4	1.5	4.4	19.0	52.0
		Average	8.1				
	0.2%MOSP	3	6.6	0.8	2.2	4.8	33.1
		7	6.9	0.9	2.5	6.4	36.9
		28	7.5	0.9	2.5	6.2	33.1
		60	10.7	3.1	8.7	75.2	80.9
		90	6.9	0.9	2.7	7.1	38.5
		Average	7.7				

 DOI: https://doi.org/10.30564/jbms.v3i2.3735

Table 11. Summary of Mean in Acid and Base Medium

Mix	Medium			
	Acid (%)		Base (%)	
	HNO_3	H_2SO_4	N_2SO_4	$MgSO_4$
0 % MOSP	-11.5	-41.4	9.0	8.1
0.2 % MOSP	-12.6	-39.1	6.7	7.7

In acid environment, sulphuric and nitric acids are strong acids. When an acid comes into contact with concrete, the first line of attack arises from the reaction of the acid with portlandite (calcium hydroxide – CH) leading to the formation of calcium sulphate (ie, gypsum) and water. In the case of sulphuric acid, the reaction may be written as:

$$H_2SO_4 + Ca(OH)_2 \rightarrow C_3A.3CS.H_{32} \quad (2)$$

Acid attack on concrete is generally exhibited at pH < 6.5 [Fattuhi and Hughes, 1983].

In sulphate environment, the two sulphate media used are 20% Na_2SO_4 and $MgSO_4$. The sulphate ions penetrate into the concrete, then react with free and abundantly available portlandite, which in turn reacts with monosulphate to form ettringite. The reaction is given as:

$$C_3A.CS.H_{12}\,(\text{monosulphate}) + 2CSH_2\,(\text{gypsum}) + 16H \rightarrow C_3A.3CS.H_{32}\,(\text{ettringite}) \quad (3)$$

The expansive nature suggests the formation of ettringite which is characterized by mass increase (Table 11). The chemical properties in the formation of iron (ii) hydroxide as shown in Equation 4:

$$Ca(OH)_2 + FeSO_4 + 2H_2O \rightarrow CaSO_4.2H_2O + Fe(OH)_2 \quad (4)$$

5. Conclusions

An evaluation on the use of Moringa oleifera seed powder (MOSP) as an additive for concrete production and the possible effects and transformations was undertaken in this work. The followings are conclusions on the work.

(1) The x-ray diffraction showed that the dominant minerals (cristobalite and quartz) in MOSP are polymorphs of silica, and the chemical properties show that MOSP has a high content of SO_3. From past works the high content was considered to show the strength development and provides resistance to sulphate attacks. Therefore, MOSP can be classified as a retarder, and good as a sulphate-resistant material for cement and concrete.

(2) The work recommends the limit of replacement of cement by wt. % of MOSP in concrete to be limited to 0.2% to 0.3%.

(3) The basic characteristics of the material as a paste showed that it could be used for hot weather concreting where enough time is allowed for concreting, and for non porous concrete, the water requirement should not be greater than 34%, and replacements not greater than 1.0%.

(4) In the fresh condition the workability was improved with MOSP added to concrete mix. However, the water absorption increased with increase in the quantity of MOSP. Therefore, in using MOSP for concreting, the need to use water-reducing agents maybe helpful.

(5) Addition of MOSP is beneficial in increasing the density of concretes. The compressive strength was increased but within the limits of replacement levels of 0.2% and 0.3%. Therefore, for optimum performance, replacement should not exceed 0.2% by wt. % of cement.

(6) MOSP-concrete in acid environment showed that acid attack appeared to be the most likely damage mechanism responsible for observed deterioration.

(7) From the study, in situations where acid and sulphate co-exist, acid mechanism maybe the overriding attack process responsible for observed degration in concrete.

Highlights

- The dominant minerals in MOSP are cristobalite and quartz, which are polymorphs of SiO_2.
- The high content of SO_3 (28 %) is not a disadvantage rather an advantage. This property makes MOSP a retarder by slowing down the strength development, and equally provides resistance to sulphate attack.
- The optimum replacement of cement by wt. % is 0.2 %, and improves workability, density, and compressive strength, but increases water absorption.
- MOSP-concrete in acid environment showed that acid attack appeared to be the most likely damage mechanism responsible for observed deterioration.

References

[1] Application of Super Absorbent Polymer (SAP) in Concrete Construction: State-of-the-Art Report. Prepared by Technical Committee, 225-SAP. Edited by V.Mechtcherine and H.W. Reinhardt, 2012.

[2] R.M.I.R Susilorino, H. Hardjasaputra, S. Tudjono, Y. Kristianto, A. Patrama (2014). "Compressive strength of optimization of natural polymer modified mortar with moringa oleifera in various curing Medias." ICETIA, 107-110.

[3] Rr. M. I. R. Susilorini, H Hardjasaputra, S Tudjono, Y Kristianto, A Putrama (2014). "Compressive strength optimization of natural polymer modified mortar with moringa oleifera in various curing medi-

DOI: https://doi.org/10.30564/jbms.v3i2.3735

as." ICETIA, 43, 107-110.

[4] BS EN 196-1: 2016 – Methods of Testing Cement. Determination of Strength.

[5] BS EN 12620: 2013 – Aggregates for Concrete.

[6] BS 812-2: 1995. Testing Aggregates - Methods for Determining Density.

[7] NF P15-467-1985: Liants Hydrauliques – Méthode Pratique Instrumentale D'Analyse des Ciments par Spectrométrie de Fluorescence des Rayons X.

[8] BS EN 196-3: Methods of Testing Cement. Determination of Setting Times and Soundness.

[9] BS EN 12350-2: 2019: Testing Fresh Concrete. Slump Test.

[10] BS 1881-122: Testing Concrete Part 122: Methods for Determination of Water Absorption.

[11] BS EN 12390-7: 2019 – Testing Hardened Concrete. Density of Hardened Concrete.

[12] BS EN 12390-3: Testing Hardened Concrete. Compressive Strength of Test Specimens.

[13] F. Newkirk (1951). "Effect of SO_3 on the alkali compounds of Portland cement clinker." Journal of Research of the National Bureau of Standards, 47 (5), 349-356.

[14] S Horkossa, G Escadeillas, T Rizk , R Lteifc (2016) "The effect of the source of cement SO_3 on the expansion of mortar." Case Studies in Construction Materials, 4, 62-72.

[15] T.M. Borhan and R.S. Al-Rawi (2016). "Combined effect of MgO and SO_3 contents in cement on compressive strength of concrete." Al-Qadisiyah Journal For Engineering Sciences, 9 (4), 516-525.

[16] S Horkossa, G Escadeillas, T Rizk, R Lteif (2011). "The effect of the source of cement SO3 on the expansion of mortars." Case Studies in Construction Materials, 4, 62-72.

[17] Xie L, Deng M, Tang J, and Liu K (2021). "Development of cementitious materials prepared with phosphorous bearing clinkers. Material, 14, 508, htttps://doi.org/10.3390/mal14030508.

[18] L.R Drees, LP Wilding, NE Smeck, AL Senkayi (1989). "Silica in soils: Quartz and disordered silica polymorphs." http:doi.org/10.2136/sssabokser1.2ed.c.19.

[19] Hendrawati, Eti Rohaeti, Hefni Effendi, Latifah K Darusman (2015). "Characterization of physico-chemical properties of nano-sized moringa oleifera seed powder and its application as natural coagulant in water purification process." Journal of Environment and Earth Scienc, 5, (21), 18-26.

[20] Kumari, P., Sharma, P., Srivastava, S. & Srivastava, M.M. (2006). Bio sorption studies on shelled *Moringa oleifera* Lamarck seed powder: Removal and recovery of arsenic from aqueous system. Int. *J.Miner. Precess*. 132 (78): 131–139.

 DOI: https://doi.org/10.30564/jbms.v3i2.3735

BILINGUAL PUBLISHING CO.
Pioneer of Global Academics Since 1984

Journal of Building Material Science
https://ojs.bilpublishing.com/index.php/jbms

ARTICLE

Photon and Fast Neutron Transmission Parameters of Metakaolin Doped Concrete

O.I. Olarinoye[1] M.M. Idris[2*] M. Kure[1]

1. Department of Physics, Federeal University of Technology, Minna, Nigeria
2. Department of Physics, Nasarawa State University, Keffi, Nigeria

ARTICLE INFO

Article history
Received:9 October 2021
Accepted:30 November 2021
Published Online:6 December 2021

Keywords:
Metakaoline
Photons
Thermal neutrons
Concrete
EXABCal

ABSTRACT

Radiation-shielding properties of metakaolin doped concrete samples were investigated in this report. The gamma photon mass attenuation coefficients and exposure buildup factor of the samples were determined theoretically using WinXcom and EXABCal software respectively for the energy range of 15 keV - 15 MeV and fast neutron removal cross section for the concrete sample was evaluated. Results indicated that, oxides of silicon, aluminum, calcium and iron determined through the energy dispersive X-ray fluorescence spectrometric analysis constitute more than 85% of the chemical composition of the concrete samples. The oxides contribute 85.46, 86.47, 87.55, 88.75, and 86.15 % of the total chemical oxides in MK00, MK05, MK10, MK15, and MK20 respectively. Densities of the prepared MK doped concrete were in the range of 2.575-2.667 g/cm^3. Compressive stress of prepared MK doped concretes increased consistently with the curing period for each concrete sample. CS grew from 8.71 - 10.63, 8.84 - 10.83, 9.44 - 11.22, 10.89 - 11.53, and 10.76 - 11.43 MPa for MK00, MK05, MK10, MK15, and MK20 respectively as the period extends from 7 to 28 days. Mass attenuation coefficient decrease steadily with an increase in energy up to about 0.1 MeV and the decrease become smaller beyond this energy with increasing energy for all the mixtures. Fast neutron removal cross section results indicate that MK10 (0.07693 cm^{-1}) has the highest value of Σ_R followed by MK15 (0.07628 cm^{-1}) and MK20 (0.07537 cm^{-1}) while MK00 (0.07380 cm^{-1}) and MK05 (0.07404 cm^{-1}) have approximately the same value. It was found that MK10 concrete has the best gamma radiation and fast neutron shielding ability among the MK doped concrete under study.

1. Introduction

The continuous beneficial use of ionizing radiation (IR) and radioisotopes in the diagnosis and treatment of health trauma; electricity generation; food processing and preservation; material characterization and other peaceful purposes is hinged on adequate radiation protection of man and the biota against the harmful effect of IR [1,2]. A commonly adopted radiation protection technique is the use of barrier (shield) to confine the IR to a restricted volume of space or attenuate the radiation to as low as acceptable outside the barrier. When there is no space and cost restraint, the use of concrete as structural shield is widely accepted in different areas of IR and radioisotope appli-

**Corresponding Author:*
M.M. Idris,
Department of Physics, Nasarawa State University, Keffi, Nigeria;
Email: idrismustapham@nsuk.edu.ng

DOI:https://doi.org/10.30564/jbms.v3i2.3817

cations [3-6]. Concretes can generally be produced with locally available materials into a wide variety of structural configurations while requiring very minimal maintenance during use. Reports on the IR shielding capacity of different types of concrete have been published by different research groups [2,4,7]. The conclusion drawn from most of these reports is that the radiation attenuating capacity of concrete is a function of the radiation properties (energy and type) and the concrete's physical and chemical properties. However, the physical and chemical properties of concrete is to a large extent dependent on the properties of its composition [2,5,6].

Traditionally, concrete is a mixture of binder (cement), aggregates (fine and coarse) and water. Of all these, cement is the most expensive per unit mass. Furthermore, the exploration of raw materials used in the production of cement and the production process causes environmental degradation and emission of CO_2 (a green-house gas) respectively [3,4]. In fact, the cement industry is one of the biggest emitters of green-house gases and other environmental pollutants [8]. These have made research investigating alternative materials with pozzolanic properties that could serve as cement replacement (fully or partially) in the production of concrete very active [2,3,5,8]. In radiation protection, such replacement must however, not reduce the mechanical strength and shielding capacity of the concrete [3,9].

Metakaolin (baked kaolin clay) is derived from the calcination of kaolin clay at a temperature between 600 and 900 °C [3,10]. Metakaolin (MK) is a pozzolanic material rich in silica and alumina and it reacts with calcium hydroxide to give compounds with cement-like properties [11]. The partial replacement of cement with MK in concrete has produced concrete with decreased porosity, increased density, higher resistance to water pressure and chemically aggressive environment, reduced aggregate segregation and bleeding, reduced shrinkage and improve the physical and chemical properties of concretes [11-14]. The partial replacement of MK in concrete has also been shown to decrease the radon exhalation rate in concrete [3,12,13].

The effect of partial MK replacement of cement in concrete on the photon and neutron shielding capacity of concrete is scarce in the literature. This study thus investigates the effect of partial replacement of cement by MK on the photon and fast neutron shielding capacity of concrete. Kaolin clay is a mineral found in large commercial quantity (circa 50 million metric tons in reserve) and much more untapped in different parts of Nigeria [15] and coupled with the fact that Nigeria is seriously considering the use of nuclear technology for electrical power generation are further motivations for this study.

2. Materials and Methods

2.1 Metakaolin and Concrete Production

Kaolin rocks obtained locally from *Alkeleri* area of *Bauchi* state, Nigeria were grounded into fine power to increase their surface area and improve homogeneity. The fine powder was subsequently calcined at 800 °C for one hour in an electric furnace. After this heat treatment the clay powder was air dried, grounded again and sieved through a 150 µm mesh sieve. The homogenized clay powder was then analyzed chemically and used for concrete production.

Ordinary portland cement, fine (FA) and coarse (CA) aggregates obtained locally together with water and produced metakaolin (MK) were used for concrete production. The aggregates conformed with the ASTM standard. Measured metakaolin and aggregates were dry mixed for about 300 seconds after which cement was added in the right proportion and mixed for another 270 seconds for consistence. Tap water was then added and the mixture was mixed for 2 minutes after which a polycarboxylate based superplasticizers was added and mixed for another 210 seconds. The design mix for the concrete cubes was 1:2:3 representing the ratio OPC: FA: CA while a water to cement ratio of 0.5 was adopted for all mixtures. The fresh mixtures were cast into a 50 x 50 x 50 mm steel moulds. By the use of a vibratory table with vibration time of 10 minutes, each concrete mould was added to give shape and reduce voids within the concrete matrix. The cubes were de-molded after 24 hours and put in curing tank filled with water at 20 °C for curing. In all, five mortar mixtures coded as MK00, MK05, MK10, MK15 and MK20 representing the partial replacements using MK by weight of cement (bwoc) at 0, 5, 10, 15 and 20% respectively were prepared.

2.2 Compressive Strength Determination

The curing period for the MK-concretes ranged from 7 to 28 days. For each of the curing period, the compressive strength of the concrete cubes was tested in triplicate according to the ASTMC109/C109M standard procedure [16]. The masses of the concrete sample were measured in order to determine their respective densities.

2.3 Chemical Analysis of Concrete Samples

The concentrations of major chemical oxides in the prepared concrete samples were determined through the energy dispersive X-ray fluorescence (EDXRF) spectrometric analysis. The concrete blocks were pulverised, sundried and continuously weighed after an interval of 24 hours until a

 DOI:https://doi.org/10.30564/jbms.v3i2.3817

near constant weight was obtained. A portion (0.02 kg) of the pulverised and dried samples were mixed with a binder (PVC dissolved in toluene) carefully and pressed into circular pellets in a hydraulic press under a pressure of about 20 tons. The pellets each of diameter about 30 ± 3 mm were then put into the sample chamber of a PANanalytical Minipal4model PW4025/45B EDXRF spectrometer for chemical analysis of major oxides in the sampled concretes.

2.4 Calculation of Shielding Parameters

2.4.1 Photons

When a monochromatic beam of photons is incident on a thin absorbing medium of mass thickness *t*, the intensity upon emerging from the medium is evaluated using the equation:

$$I = I_o e^{-\mu_m t} \quad (1)$$

Where I, is the transmitted photon intensity while I_O and μ_m are respectively the incident photon intensity and the mass attenuation coefficient (MAC) of the material. The MAC is a measure of the mean number of photo-interactions which occurs between the incident photons and material medium of interest at a given mass thickness. It is a function of the energy of the incident photon.

$$\mu_m^c = \sum_i^n w_i(\mu_m)_i \quad (2)$$

In Equation 2, μ_m^c, is the mass attenuation coefficients of the composite material (concrete) while $(\mu_m)_i$ and w_i is the MAC of the i^{th} component (oxide) in the concrete and its weight fraction respectively. The MAC values of the concrete samples were evaluated via the WinXCOM software. Using the obtained chemical composition of the concretes through the EDXRF analysis as shown in Table 1 as the input parameter in WinXCOM.

Many of the photon interaction processes depend on the atomic number (Z) of the interacting medium. A convenient parameter used to represent atomic number of multi elemental material such as concrete is effective atomic number. Z_{eff} is a function of energy as it varies with varying energy which is also It is an important parameter used for radiation dose measurement and shielding calculations [18,19]. The effective atomic number of the concrete samples were estimated using the equation [18,19]:

$$Z_{eff} = \frac{\sum_i f_i A_i (\mu_m)_i}{\sum_j f_j \frac{A_j}{Z_j} (\mu_m)_j} \quad (3)$$

Where f_i, A_i and Z_i are the fractional abundance, atomic weight and atomic number of element i.

When scattered and secondary photons within the material is transmitted, the right hand side of Equation 1 is usually corrected using a multiplying factor called photon buildup factor (B). The buildup factor depends transmitting medium optical thickness, photon energy and detector response function among other factors. When the detector response function is the absorbed photon dose in air, the exposure buildup factor is prescribed. In this research, the exposure (EBF) buildup factors was considered and evaluated for the concrete samples using the EXABCal software [20] for different photon energies at selected depths.

2.5 Effective Removal Cross-Section of Fast Neutron

The attenuation of fast neutrons through a material medium can be estimated using its effective removal cross section. The fast neutron effective removal cross section Σ_R (FNRCS) is a measure of the likelihood that a neutron will undergo a given interaction per unit length of the material it transmits through. Σ_R has been developed to accommodate neutron scattering and buildup. For composite material, the Σ_R is often estimated via the equation [21-23]:

$$\Sigma_R = \bar{\rho} \sum \bar{w_i} (\frac{\Sigma_R}{\rho})_i \quad (4)$$

Where, ρ, w_i, and $\left(\frac{\Sigma_R}{\rho}\right)_i$ is the mass density of the glass, weight fraction, and fast neutron mass removal cross section of the i^{th} element in the absorbing/interacting material. $\frac{\Sigma_R}{\rho}$ is usually a smooth function of atomic number according to [21]:

$$\frac{\Sigma_R}{\rho} = 0.19 Z^{-0.743} \quad \text{for } Z \leq 8; \quad (5)$$

and,

$$\frac{\Sigma_R}{\rho} = 0.125 Z^{-0.565} \quad \text{for } Z > 8 \quad (6)$$

Σ_R of the concrete samples were estimated via Equations 4 - 6.

3. Results and Discussion

3.1 Compressive Stress

The obtained values of the compressive strength (CS) of the concrete samples as a function of curing period (in days) is depicted in Figure 1.

The figure shows a consistent increase in CS with the curing period for each concrete sample. CS grew from 8.71 - 10.63, 8.84 - 10.83, 9.44 - 11.22, 10.89 - 11.53, and 10.76 - 11.43 MPa for MK00, MK05, MK10, MK15, and MK20 respectively as the period extends from 7 to 28 days. For curing period above 7 days the CS of MK15 is the maximum compared to other concrete samples; and indicating that the optimum cement replacement level by MK which gives maximum CS is 15%. The increase in CS with metakaolin content increased could be attributed

DOI:https://doi.org/10.30564/jbms.v3i2.3817

to the increase in the oxides of silicon, aluminum, iron and calcium in the concrete samples. It is the reaction between these oxides that gives concrete the high stiffness and strength. Also, the stiffening and setting characteristics of cement paste primarily depend on hydration of aluminates [24]. The metakaolin content of the concrete though delay the concrete hardening process but increase the CS as MK content grows to an optimum level of 15%.

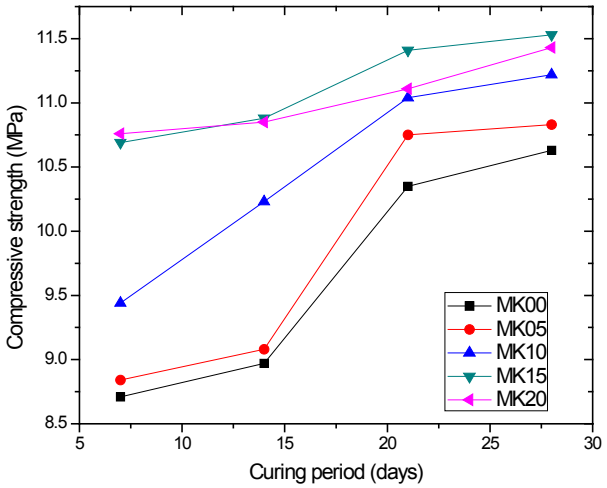

Figure 1. Compressive strength of the concrete samples as function of curing period.

3.2 Chemical Analysis of the Concretes

The result of the chemical (major oxides) analysis of the prepared concretes is given in Table1. The result shows that the oxides of silicon, aluminum, calcium and iron constitute more than 85% of the chemical composition of the concretes. These oxides to large extent dictate the chemical and mechanical features of the concrete. The oxides contribute 85.46, 86.47, 87.55, 88.75, and 86.15 % of the total chemical oxides in MK00, MK05, MK10, MK15, and MK20 respectively.

Also shown in Table 1 is the mass density (±0.001) calculated from the measured masses and volume of the concrete cubes. The density varied from 2.219 - 2.301 g/cm^3. The trend of the CS at 7-day curing period is similar to that of the density. Replacement of cement in concrete by MK up to 15% also increase the density of the concrete.

3.3 Photon Shielding Parameters

3.3.1 Mass Attenuation Coefficient

Calculated mass attenuation coefficient (MAC) (cm^2/g) of the MK-doped concretes for photon energies between 15 keV and 15 MeV and its variation with photon energy and MK replacement level is depicted in Figure 2.

Table 1. Chemical composition and mass density of concretes.

Oxides	Weighted fractions of samples				
	MK00	MK05	MK10	MK15	MK20
SiO_2	41.700	41.200	43.100	42.200	40.200
Al_2O_3	6.200	6.370	6.480	6.490	6.400
Na_2O	0.640	0.870	0.810	0.620	0.820
K_2O	0.460	0.840	0.442	0.442	0.042
CaO	36.060	37.400	36.900	38.430	38.280
MgO	2.030	2.000	1.880	1.900	2.040
TiO_2	0.220	0.310	0.250	0.300	0.290
Co_3O_4	0.010	0.010	0.019	0.004	0.010
Fe_2O_3	1.500	1.500	1.070	1.630	1.290
CuO	0.030	0.031	0.017	0.018	0.014
As_2O_3	0.006	0.010	0.008	0.007	0.006
SrO	0.450	0.510	0.037	0.440	0.440
ZrO_2	0.032	0.045	0.037	0.036	0.030
HfO_2	0.012	0.011	0.013	0.010	0.006
PbO	0.045	0.052	0.047	0.044	0.040
Density (g/cm^3)	2.219	2.248	2.301	2.274	2.261

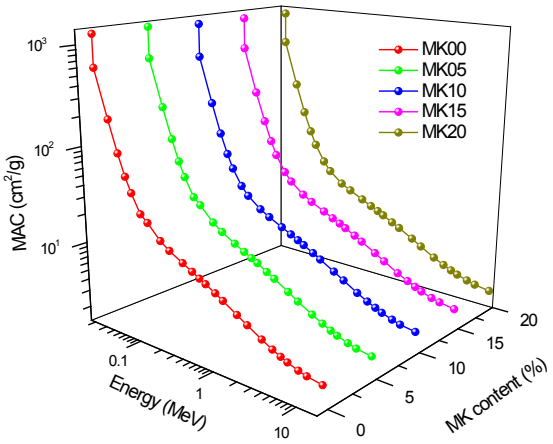

Figure 2. Mass attenuation coefficient (μ_m) of the MK doped concretes (MK0-MK20)

From Figure 2, the MAC value decrease steadily with increase in energy throughout the energy spectrum. However, the decline in MAC value was rapid for energies less than 150 keV compared to the remaining part of the energy spectrum. This rapid decline is due to the relatively high photoelectric interaction cross section (Σ_{PE}) at energies in the range 15 ≤ E ≤ 15 keV since Σ_{PE} is proportional to E^{-4}. Beyond this energy range, the Compton scattering interaction dominates the photon interaction processes. The fact that cross section for Compton scattering (Σ_{CS}) is proportional to E^{-1} explains why the reduction in MAC values is less rapid for E >150 keV. Furthermore, a comparison between the MAC

DOI:https://doi.org/10.30564/jbms.v3i2.3817

values of the concretes reveals that MAC values range from 2.28 - 1256.89, 2.28 - 1265.36, 2.23 - 1164.72, 2.23 - 1169.72, and 2.11 - 1159.66 as energy varied from 15 keV - 15 MeV for MK00, MK05, MK10, MK15, and MK20 respectively. Obviously, the trend ($(MAC)_{MK20}$ < $(MAC)_{MK10}$ < $(MAC)_{MK15}$ < $(MAC)_{MK00}$ < $(MAC)_{MK05}$) is dictated by the chemical composition of the concretes. In the photoelectric interaction dominated energy region, the differences in the MAC values is higher than the Compton scattering dominated energies. This can be attributed to the dependence of Σ_{PE} and Σ_{CS} on the atomic number (Z) of the concrete. Typically, Σ_{PE} α Z^3 while Σ_{CS} Z, hence the trend in the relative value of MAC could be the same with that of the effective atomic number of the concretes. Throughout the considered energy spectrum, MK05 had the highest MAC values an indication of the best photon absorber among the prepared concretes.

3.3.2 Effective atomic number

The Effective atomic number(Z_{eff}) of the MK doped concretes for 15 keV to 15 MeV photons as it varies with energy is shown in Figure 3. The Z_{eff} values were also noticed to lie between the minimum and maximum atomic numbers of the constituents elements. The largest values are seen in low - energy regions where the photoelectric absorption is the main interaction process. From 0.3 to 3 MeV the Z_{eff} values are reduced, this is the region where the Compton scattering is dominant. The lowest Z_{eff} can be noticed for photons of energy 1 MeV. Above 4 MeV, the Z_{eff} increases again after a period of being almost constant.

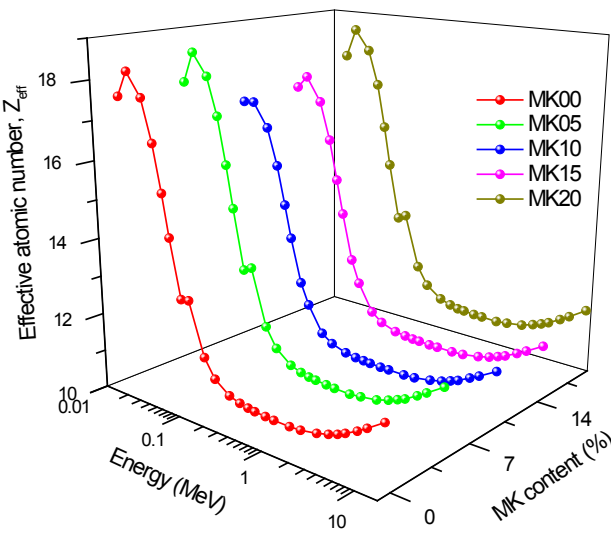

Figure 3. Effective atomic number (Z_{eff}) of the MK doped concrete (MK0-MK20).

3.4 The Exposure Buildup Factor

The Exposure Buildup Factor for mfp of 5, 10, 15, 20, 25 and 30 were calculated using the EXABCal software based on the GP fitting parameters. The energy variation of the incident photons for different mfp are presented in Figure 4(a-e).

Figure 4(a-e) presents the buildup factor changes with respect to energy and penetration depth. Irrespective of the material composition, EBF changes are similar with respect to energy. Thus, low values of EBF are observed at low energy and increases with increase in energy to certain maximum value. There is variation in peak of the plots as the material composition, energy of photon and depth of penetration varies. According to Olarinoye [9], these peaks range from 0.1 and 0.3 MeV for most materials. Beyond these peaks, a decrease in EBF is seen for all considered mfp with further increase in energy. Figure 5(a-e) the energy spectrum are categorized into low, intermediate and high energy region. This categorization is in accord with the three dominant photon interaction processes at the regions.

The photoelectric effect is the dominant mode of interaction at the lower end of the energy spectrum (15 keV - 0.1 MeV). For photoelectric effect, there is direct proportionality to the fifth power of the material's Z_{eq} and inverse proportionality to the third power of the energy under study. There is simply a removal of photons from the incoming beam thereby preventing buildup in this study. The EBF direct proportionality with Z_{eq} implies the higher Z_{eq} material will have a higher probability of removing photons than low Z_{eq} material. This is why the EBF of MK00 and MK05 are lower at these energies. The further increase in energy in the second region, the EBF is seen to increase with increasing energy. This dominated region by the compton interaction process is called the Compton region. The Compton interaction is directly proportional to the Z_{eq} at any given energy. The high EBF obtained at this region is because of the almost zero absorption taking place within this region. There is a mere degradation of photons in the process [9].

As the energy is increased further, a third interaction process kicks in. This interaction process begins at energies just beyond 1.022 MeV. Consequently, there is a decrease in EBF gradually with further increase in energy owing to the fact that the incident photons are utilized in pair production. Thus there is photons degradation in the process. Across Figure 4(a-e), is also worthy of note that higher mfp have higher EBF across the energy spectrum. This is because the EBF is a function of depth and thickness. The more the thickness, the more the chances

DOI:https://doi.org/10.30564/jbms.v3i2.3817

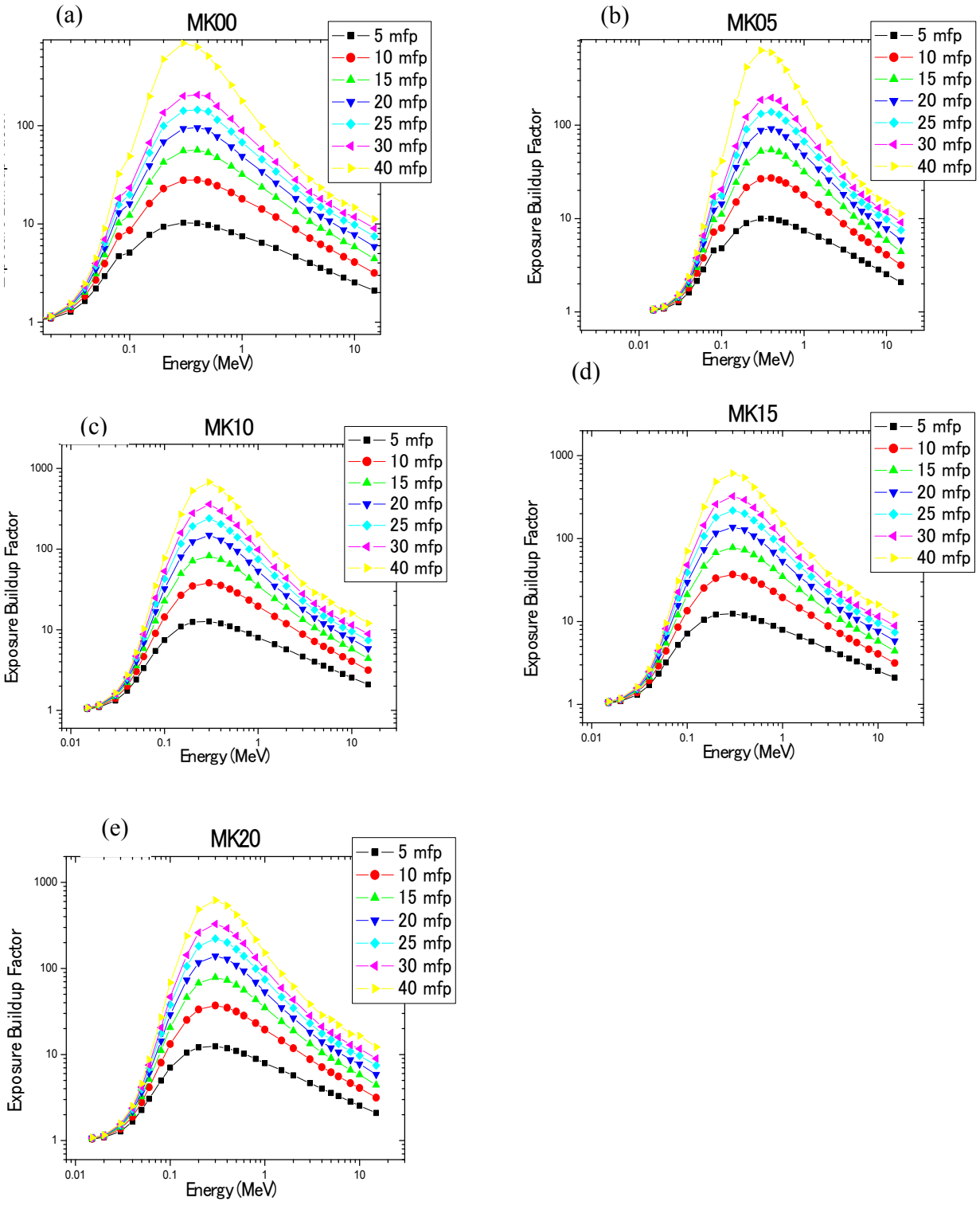

Figure 4. Energy Dependence and exposure buildup factors at various energy for MK doped concretes (MK0-MK15).

 DOI:https://doi.org/10.30564/jbms.v3i2.3817

of having photons interaction which eventually escape the system. From Figure 4(a-e), 5 mfp has the least EBF while 30 mfp has the highest EBF as expected.

Exposure Buildup Factor Variation with Penetration Depth (mfp)

The variation of Exposure Buildup Factor with depths of the concretes are shown in Figure 5 (a - d) for the selected energies (0.015, 0.15, 1.5 and 15 MeV).

The EBF increases as the penetration depth increases. There is a rapid increase in EBF at lower depths for photon energy 0.015 MeV, and increases slightly as the mfp is increased for the materials under study. However, at 0.15 MeV photon energy, the increase is rather steady with increase in energy. The lowest value of EBF was seen in MK05 followed closely by MK00. The MK10 has the highest value of EBF while MK10 and MK15 strongly overlapped between the highest and lowest EBF materials. At 1.5 and 15 MeV, the materials have similar variation in the value of EBF across all thicknesses. This account for the fact that at these energies, the Compton interaction process is dominant and hence across the thickness, they show a fairly constant value.

3.5 Fast Neutron Removal Cross Section

The Σ_R of the concretes was obtained through use of Equation 4. The variation of FNRCS with material is shown in Figure 6.

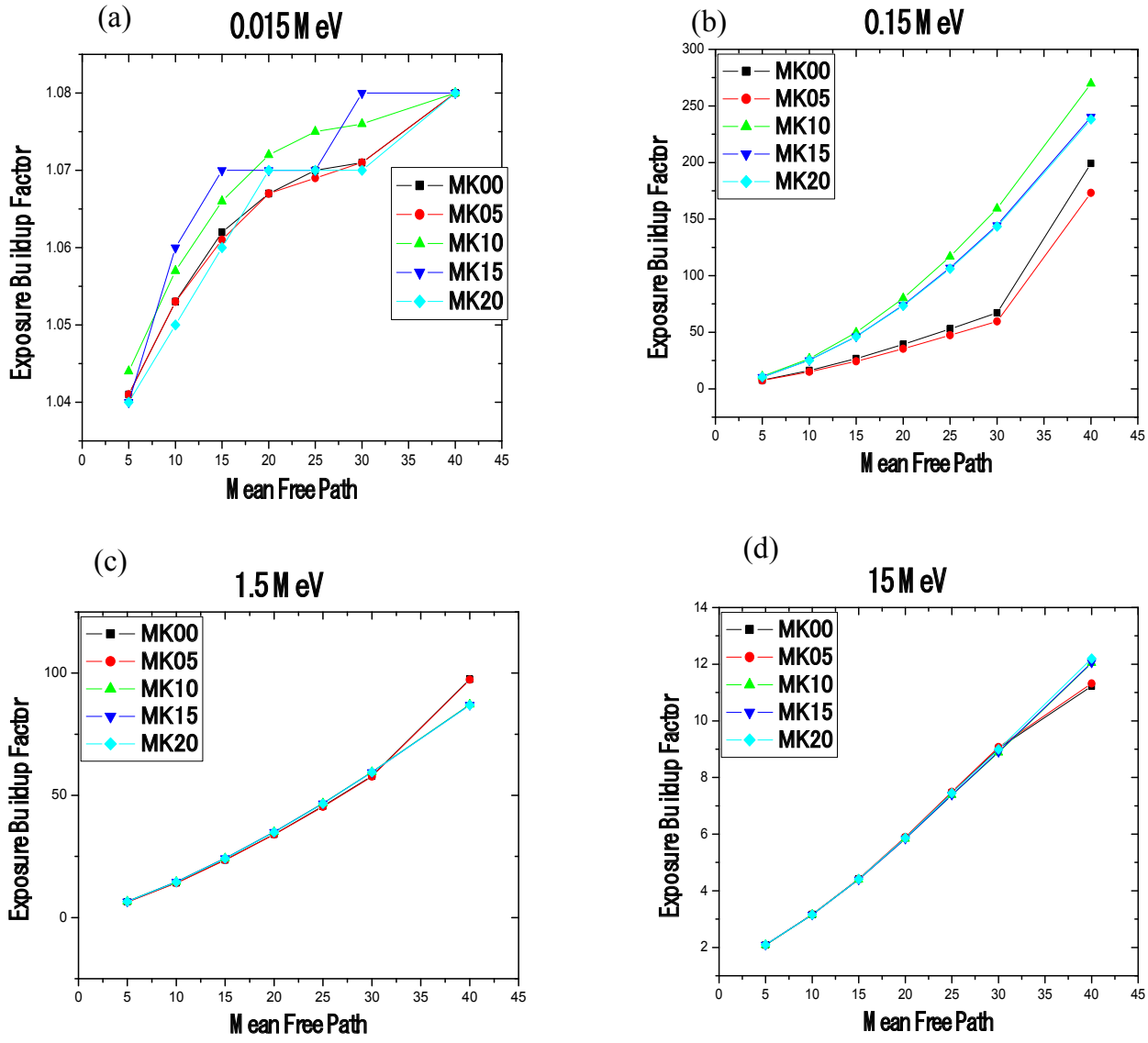

Figure 5. Variation of energy absorption buildup factor with the penetration depth for MK doped concretes (MK0-MK15).

DOI:https://doi.org/10.30564/jbms.v3i2.3817

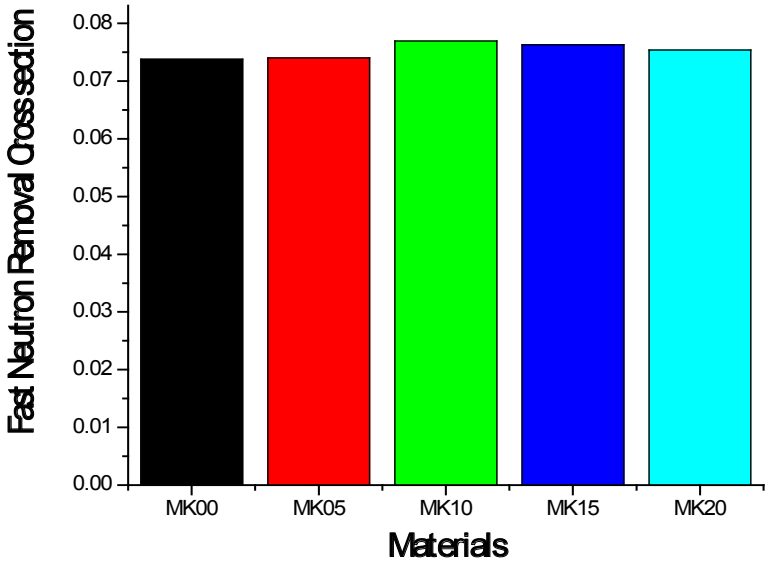

Figure 6. Fast Neutron Removal Cross Section for MK doped concrete (MK0-MK15).

The result showed that the Σ_R of MK00, MK05, MK10, MK15, MK20 were 0.07380, 0.07404, 0.07693, 0.07628, 0.07537 cm^{-1} respectively. MK10 have the highest value of Σ_R followed by MK15 and MK20 while MK00 and MK05 have approximately the same value. The closeness in their values can be attributed to their similar elemental composition. The higher values of Σ_R as seen in MK10, MK15 and MK20 can be attributed to the higher percentage of Carbon within their matrix compared to the other. The partial removal cross section of carbon is higher than every other element contained in the concretes considered. The two new BMG are thus good absorber for fast neutrons and are potentially better neutron shield material compare to heavy concretes.

4. Conclusions

In the current investigation, the mixture of metakaolin (MK), ordinary porland cement (OPC), coarse (CA), and fine aggregate (FA) were theoretically investigated. The densities of MK doped concrete were in the range of 2.575-2.667 g/cm^3. The mass attenuation coefficient of the MK concrete mixtures was investigated by the use of WinXCOM computer program at the orthovoltage and radiotherapy energies (15keV- 15MeV). Moreover, the neutron shielding features are calculated for the prepared MK doped concretes (MK00- MK20). The addition of metakaoline content has a significant effect to evolve the gamma shielding properties of the studied concretes. It was found that MK10 concrete has the best gamma radiation and fast neutron shielding ability among the MK doped concrete under study.

References

[1] Olarinoye I.O, El-Agawany FI, El-Adawy A., Rammah YS. Mechanical features, alpha particles, photon, proton, and neutron interaction parameters of TeO2-V2O3-MoO3 semiconductor glasses. DOI: https://doi.org/10.1016/j.ceramint.2020.06.093.

[2] Hossaini M.S, Islma MAS., Quasem MA, Zaman MA, 2010. Study of shielding behavior of some multilayer shields containing PB and PX; *Indian journal of Pure and applied Physics*. 48, 860-868.

[3] Buket CÖ, Cavit ÇK, Banu O, Erkan G, Serdar A, 2020. Gamma and neutron attenuation properties of alkali-activated cement mortars, Radiation Physics and Chemistry. 166. 108478. DOI: https://doi.org/10.1016/j.radphyschem.2019.108478

[4] Aycan G, Birol A, Tahir C, 2017. Photon Attenuation Properties Of Concretes Containing Magnetite And Limonite Ores; Physicochem. Probl. Miner. Process. 53(1), 184-191.

[5] Sabir BB, Wild S, Bai, J, 2001. Metakaolin and calcined clays as pozzolans for concrete: a review, *Cement and Concrete Composites*. 23(6): 441-454.

[6] Mohammad PI., Noor AM, Suhairy S, Abdul BM, Mohd KSS, Rahmad AR, 2001. Concrete mix design for X-and gamma shielding NDT group, Nuclear Malaysia.

 DOI:https://doi.org/10.30564/jbms.v3i2.3817

[7] Ripan B, Hossaini S, Mollah AS, 2015. Calculation of gamma ray attenuation parameters for locally developed shielding materials: Polyboron; JRRAS, 9, 26-34

[8] Dunuweera SP, rajapakse RM, 2018. Cement types, composition, uses and advantages of nanocement, environmental impact on cement production and possible solutions.Advances in materials Science and Engineering.
DOI: https://doi.org/10.1155/2018/4158682.

[9] Olarinoye IO, 2017. Photon buildup factors for some tissues and phantom materials for penetration depths up to 100 MFP. J. Nucl. Res. Dev. 13, 57-67.

[10] Ženíšek Michal1, VLACH Tomáš, LAIBLOVÁ Lenka, 2016. Dosage of Metakaolin in High Performance Concrete; Key Engineering Materials.
DOI: https://doi.org/10.4028/www.scientific.net/KEM.722.311.

[11] Justice M. J, 2005. Evaluation of Metakaolins for use as supplementary cementitious materials; A thesis presented to school of civil and environmental engineering, Georgia Institute of technology.

[12] Lau B. M. F., R. V. Balendran and Yu K. N., 2003. Metakaolin As A Radon Retardant From Concrete; Radiation Protection Dosimetry TECHNICAL NOTE, Nuclear Technology Publishing. Vol. 103, No. 3, pp. 273-276.

[13] Sergio A., M. Avacir Casanova Andrello3, Marcos Antonio Scapin1, Sordi, Gian-Maria A. A., 2013. High density concrete to application in radiological protection. Asessement of the additions-microsilica-metakaolin-limestone filler. *International Nuclear Atlantic Conference - INAC 2013 Recife, PE, Brazil, November 24-29.*

[14] EL-Dakroury A.M., I.S. Ibrahium and I.E. Iyob, 2014. Development and performance properties of ternary mixed concrete; Arab Journal of Nuclear Science and Applications, 47(4), (27-39).

[15] Samuel A. O., 2012. Documentation, Application and utilization of clay minerals in Kaduna state (Nigeria); intechopen.com/books.
DOI: http://dx.doi.org/10.5772/48093.

[16] ASTMC109/C109M-16a, 2016. ASTMC109/C109M-16a: Standard Test Method for Compressive Strength of Hydraulic Cement Mortars (Using 2-in. or [50-mm] Cube Specimens).

[17] Gerward, L., Guilbert, N., Jensen, K.B. and Levring, H., 2004. WinXCom—a program for calculating X-ray attenuation coefficients. *Radiation physics and chemistry*, *71*(3-4), pp.653-654.

[18] Olarinoye, I., 2011. Variation of effective atomic numbers of some thermoluminescence and phantom materials with photon energies. *Res J Chem Sci*, *1*(2), pp.64-69.

[19] El-Mallawny, R., Sayyed, M.I., Dong, M.D., 2017. Comparative Shielding Properties of Some Tellurite Glasses. Journal of Non-Crystalline Solids.

[20] I.O. Olarinoye, R.I. Odiaga, S. Paul, 2019. EXABCal: A program for calculating photon exposure and energy absorption buildup factors, Heliyon 5(7), e02017.

[21] Y.S. Rammah, I.O. Olarinoye, F.I. El-Agawany, El Sayed Yousef, S. Ibrahim, A.A. Ali, 2021. SrO-reinforced potassium sodium borophosphate bioactive glasses: Compositional, physical, spectral, structural properties and photon attenuation competence, Journal of Non- crystalline solids 559, 120667.
DOI: https://doi.org/10.1016/j.jnoncrysol.2021.120667.

[22] A. El-Khayatt, 2010. Calculation of fast neutron removal cross-sections for some compounds and materials, Annals of Nuclear Energy 37(2), 218-22.

[23] Schmidt, F. A., 1970. *Attenuation properties of concrete for shielding of neutrons of energy less than 15 MeV* (No. ORNL-RSIC-26). Oak Ridge National Lab., Tenn.

[24] Tanvir M., Nur Y., and. Abul B. E. Md, 2016. Potential of Carbon Nanotube Reinforced Cement Composites as Concrete Repair Material; Volume 2016, Article ID 1421959, 10 page.
DOI: http://dx.doi.org/10.1155/2016/1421959.

DOI:https://doi.org/10.30564/jbms.v3i2.3817

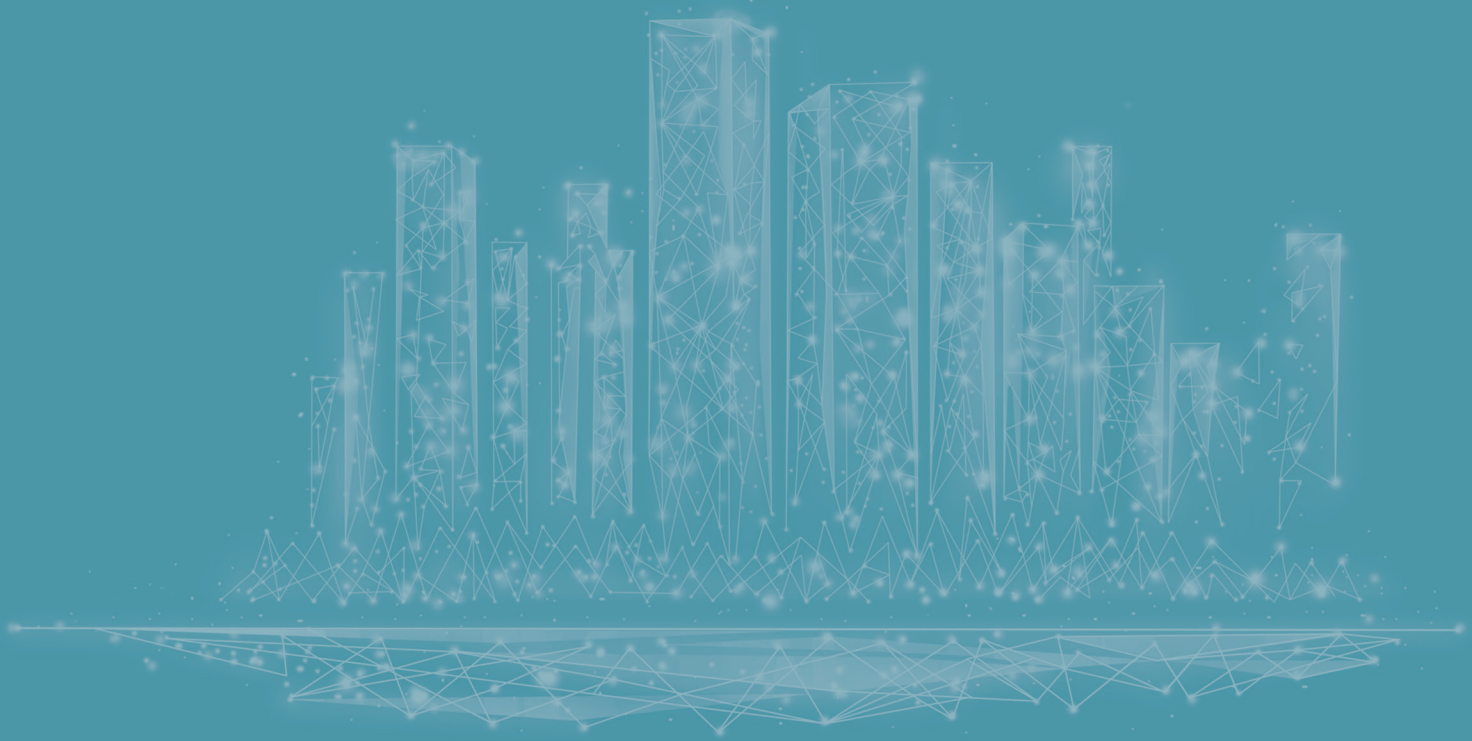

BILINGUAL
PUBLISHING CO.
Pioneer of Global Academics Since 1984

Tel:+65 65881289
E-mail: contact@bilpublishing.com
Website:ojs.bilpublishing.com

ISSN 2630-5216
02